



Draft version 2



ATLAS NOTE

October 17, 2018

¹ Measurement of flow harmonics with multi-particle cumulants in Pb+Pb ² collisions at $\sqrt{s_{\text{NN}}} = 5.02 \text{ TeV}$ with the ATLAS detector

³ Mingliang Zhou^a and Jiangyong Jia^{a,b}

⁴ *^aDepartment of Chemistry, Stony Brook University, Stony Brook, NY 11794, USA*

⁵ *^bBrookhaven National Laboratory, Physics Department, Bldg. 510A, Upton, NY 11973, United States of America*

6

Abstract

7 This internal note presents details of measurements of the multi-particle azimuthal anisotropy
8 in lead-lead collisions at 5.02 TeV at the LHC in 2015. The measurements are performed for
9 charged particles with various transverse momenta, from $0.5 < p_T < 5.0 \text{ GeV}$ to $2.0 < p_T <$
10 5.0 GeV , and in the pseudorapidity range $|\eta| < 2.5$. The anisotropy is characterized by the
11 cumulant form of Fourier coefficients, $c_n\{4\}$, of the charged-particle azimuthal angle distri-
12 bution. The Fourier coefficients are evaluated using multi-particle cumulant calculated with
13 the direct cumulant (Q-cumulant) method. For the first time, cumulant of the dipolar flow,
14 $c_1\{4\}$, was measured as a function of centrality, with different p_T ranges. Measurement of
15 higher harmonic $c_4\{4\}$ is found to fall into the picture of linear and non-linear hydrodynam-
16 ical response. In 2015 Pb+Pb run, ultra-central collision (UCC) triggers collected ample
17 central events to perform detailed studies of cumulants in ultra-central collisions. To study
18 the correlation between flow harmonics, the symmetric cumulant, as well as the recently
19 proposed asymmetric cumulant, are also investigated. Furthermore, in order to evaluate the
20 contributions from non-flow sources, the newly proposed subevent cumulant technique was
21 also applied and compared with the standard cumulant method.

22 Contents

23 1	Introduction	4
24 2	Survey of published results on cumulant in Pb+Pb collisions	6
25 3	Detector, trigger and offline event selection	10
26 3.1	Triggers	10
27 3.2	Event selection	11
28 3.3	Centrality	14
29 4	Track selection, efficiency and fakes	15
30 4.1	Track selection	15
31 4.2	Tracking in Monte-Carlo	15
32 4.3	Efficiency	17
33 4.4	Fakes	17
34 5	Methodology	19
35 5.1	Outline	19
36 5.2	Calculation of 2-, 4- and 6-particle correlation $\text{corr}_n\{2k\}$	19
37 5.2.1	Standard Q -cumulant method	20
38 5.2.2	3-subevent Q -cumulant method	21
39 5.3	Calculation of 2-, 4- and 6-particle cumulant $c_n\{2k\}$	22
40 5.3.1	Standard cumulant	22
41 5.3.2	3-subevent cumulant	23
42 5.4	Calculation of 2-, 4- and 6-particle flow signal $v_n\{2k\}$	24
43 5.5	Calculation of normalized cumulant $nc_n\{2k\}$	24
44 5.6	Universality check of flow fluctuation models	25
45 5.7	Calculation of symmetric cumulant $sc_{n,m}\{4\}$ and $nsc_{n,m}\{4\}$	26
46 5.7.1	Standard symmetric cumulant	26
47 5.7.2	3-subevent symmetric cumulant	26
48 5.8	Calculation of asymmetric cumulant $ac_{n,n+m}\{3\}$ and $nac_{n,n+m}\{3\}$	27
49 5.8.1	Standard asymmetric cumulant	27
50 5.8.2	3-subevent asymmetric cumulant	28
51 6	Analysis	30
52 6.1	Particle phase space	30
53 6.2	Trigger weighting	31
54 6.3	Flattening procedure	33
55 6.4	Event class	35
56 6.5	Mixed events	38
57 6.6	Statistical uncertainty	39
58 7	Systematics and cross-checks	41
59 7.1	Outline	41
60 7.2	Ultra-central collision trigger efficiency	42
61 7.3	Monte-Carlo closure	43
62 7.4	Loose and tight track selection	45
63 7.5	Lower and higher tracking efficiency	46
64 7.6	Pileup rejection	47

65	7.7	Detector effects from flattening procedure	49
66	7.8	Centrality definition	51
67	7.9	Event class bin width	52
68	7.10	η gap for subevent	52
69	7.11	Summary of systematics	54
70	7.11.1	2-particle cumulant $c_n\{2\}$	55
71	7.11.2	4-particle cumulant $c_n\{4\}$ and $\hat{c}_n\{4\}$	56
72	7.11.3	6-particle cumulant $c_n\{6\}$ and $\hat{c}_n\{6\}$	58
73	7.11.4	Universality check of flow fluctuation	60
74	7.11.5	Symmetric and normalized symmetric cumulant $sc_{n,m}\{4\}$ and $nsc_{n,m}\{4\}$	61
75	7.11.6	Asymmetric and normalized asymmetric cumulant $ac_{n,n+m}\{3\}$ and $nac_{n,n+m}\{3\}$	63
76	8	Results	64
77	8.1	Outline	64
78	8.2	Comparison between standard and 3-subevent cumulant	64
79	8.3	2-particle cumulant $c_n\{2\}$	67
80	8.4	4-particle cumulant $c_n\{4\}$ and $nc_n\{4\}$	70
81	8.5	4-particle cumulant in ultra-central collisions	76
82	8.6	4-particle cumulant in 2.76 and 5.02 TeV	81
83	8.7	6-particle cumulant $c_n\{6\}$ and $nc_n\{6\}$	81
84	8.8	Universality check of flow fluctuation models	87
85	8.9	Symmetric cumulant $sc_{n,m}\{4\}$ and $nsc_{n,m}\{4\}$	90
86	8.10	Asymmetric cumulant $ac_{n,n+m}\{3\}$ and $nac_{n,n+m}\{3\}$	95
87	9	Selected plots for the paper	97
88	9.1	2-particle cumulant $v_n\{2\}$ with $n = 2, 3, 4$	97
89	9.2	4-particle cumulant $nc_n\{4\}$ with $n = 2, 3, 4$	97
90	9.3	6-particle cumulant $nc_n\{6\}$ with $n = 2, 3, 4$	98
91	9.4	Cumulant ratio $v_n\{4\}/v_n\{2\}$ with $n = 2, 3, 4$	98
92	9.5	Cumulant ratio $v_n\{6\}/v_n\{4\}$ with $n = 2$ and comparison with CMS	98
93	9.6	Symmetric and asymmetric cumulant	99
94	9.7	Volume fluctuation	100
95	10	Summary	102
96	11	Appendix	103
97	11.1	Systematics from 3-subevent method	103
98	11.2	Results for 2.76 TeV Pb+Pb	108
99	11.3	Results for 2.76 TeV Pb+Pb HIJING	110

100 List of contributions

101 • Mingliang Zhou

- 102 – Writing analysis code for the standard and sub-event cumulant calculation;
- 103 – Evaluating the systematic uncertainties in 5.02 TeV Pb+Pb;
- 104 – Writing the internal note;
- 105 – Writing the paper draft;

106 • Jiangyong Jia

- 107 – Exploring flow fluctuation in the ultra-central collision;
- 108 – Producing final physics plots;
- 109 – Writing the paper draft;

110 1 Introduction

111 Heavy-ion collisions at RHIC and the LHC create hot, dense matter whose space-time evolution is well
 112 described by relativistic viscous hydrodynamics [1, 2]. Owing to strong event-by-event density fluctua-
 113 tions in the initial state, the distributions of the final-state particles also fluctuate event-by-event. These
 114 fluctuations lead to harmonic modulation of the particle densities in the azimuthal angle ϕ , characterized
 115 by a Fourier expansion $dN/d\phi \propto 1 + 2 \sum v_n \cos n(\phi - \Phi_n)$, where v_n and Φ_n represent the magnitude and
 116 event-plane angle of the n^{th} -order harmonic flow. These quantities can also be conveniently represented
 117 by the per-particle "flow vector" $\mathbf{v}_n = v_n e^{-in\Phi_n}$ in each event. The measurements of harmonic flow coef-
 118 ficients v_n , and their event-by-event fluctuations, have placed important constraints on the properties of
 119 the medium and on the density fluctuations in the initial state.

120 One important observable for studying event-by-event fluctuations of the initial condition as well as
 121 the final state dynamics of the medium is $p(v_n)$, the probability density distribution of the v_n , for event
 122 selected with similar centrality. The $p(v_n)$ are directly related to event-by-event fluctuations of the eccen-
 123 tricity ϵ_n associated with the n^{th} -order shape component in the initial state, $p(\epsilon_n)$ [3, 4]. Measurement of
 124 $p(v_n)$ has been performed at the LHC for $n = 2, 3$ and 4 using an unfolding technique. While the $p(v_n)$
 125 shape is approximately described by a Gaussian fluctuation of the underlying flow vector, significant
 126 deviations from Gaussian are observed at large v_2 in mid-central and peripheral collisions, and at large
 127 v_3 in mid-central collisions. Further detailed study of this non-Gaussian behavior, however, is limited by
 128 large uncertainties in the tail of the $p(v_n)$ distribution arising from the unfolding procedure.

129 An alternative way to study the $p(v_n)$ is through multi-particle azimuthal correlations within the
 130 cumulant framework [5, 6]. This method calculates the quantities $c_n\{2k\}$, known as the $2k$ -particle
 131 cumulants for the n^{th} -order flow harmonics. In the absence of non-flow correlations, such as resonance
 132 decay, jets etc, the $c_n\{2k\}$ are related to the moments of the $p(v_n)$, and therefore are sensitive to the
 133 shape of the $p(v_n)$ distribution. Most models of the initial state of A+A collisions predict a $p(v_n)$ whose
 134 shape is close to Gaussian, and that the four-particle cumulants $c_n\{4\}$ are zero or negative. The $c_n\{4\}$ for
 135 $n = 2, 3$ and 4 have been measured at RHIC and the LHC. The values of $c_2\{4\}$ and $c_3\{4\}$ are found to be
 136 negative, except for $c_2\{4\}$ in very central Au+Au collisions at RHIC where it is positive. The origin of
 137 this positive $c_2\{4\}$ is not understood. Furthermore, ATLAS has shown that $c_4\{4\}$ is negative in central
 138 collisions but becomes positive in mid-central and peripheral collisions. This sign change has been
 139 interpreted as nonlinear model-mixing effects between v_4 and v_2 , i.e. v_4 contains nonlinear contributions
 140 that are proportional to v_2^2 .

141 In the cumulant framework, the $p(v_n, v_m)$ is studied using the so-called four-particle "symmetric
 142 cumulants", $sc_{n,m}\{4\} = \langle v_n^2 v_m^2 \rangle - \langle v_n^2 \rangle \langle v_m^2 \rangle$ [7] or the three-particle "asymmetric cumulants" such as
 143 $ac_{n,2n}\{3\} = \langle v_n^2 v_{2n} \cos(2n(\Phi_n - \Phi_{2n})) \rangle$ [8], which is sensitive to $p(v_n, v_m)$. The symmetric cumulants
 144 involve only the magnitude of the flow vector, while the asymmetric cumulants involve both the mag-
 145 nitude and phase of the flow vector. For this reason, asymmetric cumulants are often referred to as the
 146 "event-plane correlators". The $sc_{2,3}\{4\}$, $sc_{2,4}\{4\}$ and $ac_{2,4}\{3\}$ have been measured previously in A+A
 147 collisions [9]. The values of $sc_{2,3}\{4\}$ are found to be negative, reflecting an anti-correlation between v_2
 148 and v_3 , while the positive values of $sc_{2,4}\{4\}$ and $ac_{2,4}\{3\}$ suggest a positive correlation between v_2 and
 149 v_4 , consistent with the nonlinear mode-mixing effects mentioned before.

150 In heavy-ion collisions, v_n coefficients are often calculated for events with similar activity, defined
 151 as the particle multiplicity in a fixed pseudorapidity range. Due to fluctuations in the particle production
 152 process, the centrality for events selected to have the same particle multiplicity fluctuates from event to
 153 event. Since the v_n coefficients change with centrality, any fluctuation of centrality may lead to additional
 154 fluctuations of v_n , which broaden the underlying $p(v_n)$ and $p(v_n, v_m)$ distributions [10]. Therefore the
 155 cumulants $c_n\{2k\}$, symmetric cumulants $sc_{n,m}\{4\}$ and asymmetric cumulants $ac_n\{3\}$ could be affected
 156 by the centrality resolution effects associated with a given event class definition. This centrality fluctua-

tions, more commonly known as volume fluctuations, have been shown to contribute significantly to the event-by-event fluctuation of conserved quantities, especially in ultra-central collisions due to the steeply falling centrality distribution [11]. Recently, the volume fluctuations are found to also influence flow fluctuations, and is responsible for the sign-change of the $c_2\{4\}$ in ultra-central collisions [12]. Therefore, a detailed study $c_n\{2k\}$, $sc_{n,m}\{4\}$ and $ac_{n,2n}\{3\}$ for different choices of reference event classes helps to clarify the meaning of centrality and provide insights on the sources for particle production in heavy-ion collisions. In this paper, two reference event classes are used in the calculation of cumulants to study the influence of volume fluctuations: the total transverse energy in the forward pseudorapidity $3.2 < |\eta| < 4.9$ and the number of reconstructed charged particles in mid-rapidity $|\eta| < 2.5$.

One weakness of the standard multi-particle cumulant method is that it may not suppress adequately the non-flow correlation, which, although expected to be very small in A+A collisions, could in principle be responsible for the positive $c_n\{4\}$ values discussed above. These non-flow correlations can be further suppressed using a three-subevent cumulant method, which is based on correlation of particles from three different subevents separated in pseudorapidity η . This three-subevent method has successfully used in pp and $p+Pb$ collisions to suppress non-flow correlations [13], which are much stronger than in A+A collisions, to obtain a $c_n\{4\}$ associated with long-range collective flow. Therefore, the influence of non-flow on $c_n\{4\}$ in the standard method can be quantified by comparing with the three-subevent method.

This internal note presents a measurement of cumulant $c_n\{2k\}$, symmetric cumulant $sc_{n,m}\{4\}$ and asymmetric cumulant $ac_{n,2n}\{3\}$ in Pb+Pb collisions at $\sqrt{s_{NN}} = 5.02$ TeV with the ATLAS detector. The results are obtained with the standard cumulant method, as well as with the three-subevent cumulant method to quantify the influence of non-flow correlations. The highlights of this measurement include: 1) first study of $c_1\{4\}$ associated with ϵ_1 , the dipole fluctuations in the initial state, 2) investigation of the centrality and p_T dependence of $c_2\{4\}$ and $c_3\{4\}$, especially the sign of these quantities in ultra-central collisions, 3) precision study of $c_4\{4\}$ to understand the role of mode-mixing effects, 4) quantify the flow fluctuation using model-independent observable and 5) study of the correlation among different flow harmonics through symmetric cumulant and asymmetric cumulant. This internal note is organized as follows.

- Section. 2 summarizes the previous published results that are related with this analysis;
- Section. 3 describes the ATLAS detector, trigger, and offline event selections;
- Section. 4 contains a description of selection criteria for charged-particle tracks, as well as details of the Monte Carlo simulation samples used to derive the tracking efficiency and fake-track rates;
- Section. 5 outlined the detailed cumulant method;
- Section. 6 outlined the detailed analysis procedure;
- Section. 7 contains detailed discussions of the systematic errors;
- Section. 8 presented all the results of this analysis;
- Section. 9 summarizes the plots to be included in the paper;
- Section. 10 is devoted to summary and conclusions;
- Section. 11 contains comprehensive summary of systematics and results;

196 2 Survey of published results on cumulant in Pb+Pb collisions

197 Whenever the heavy ion collision reaches a new high energy, the first thing to check is the energy de-
 198 pendence of the flow harmonics. ALICE has published the measurement of v_2 at 5.02 TeV Pb+Pb and
 199 compared with previous energies [14], as shown in Fig. 1. Except for the lowest energies, where v_2 could
 200 go negative, for $\sqrt{s_{\text{NN}}} > 5 \text{ GeV}$, as the collision energy increases, the v_2 also increases. At the TeV level,
 201 the magnitude of v_2 almost saturates.

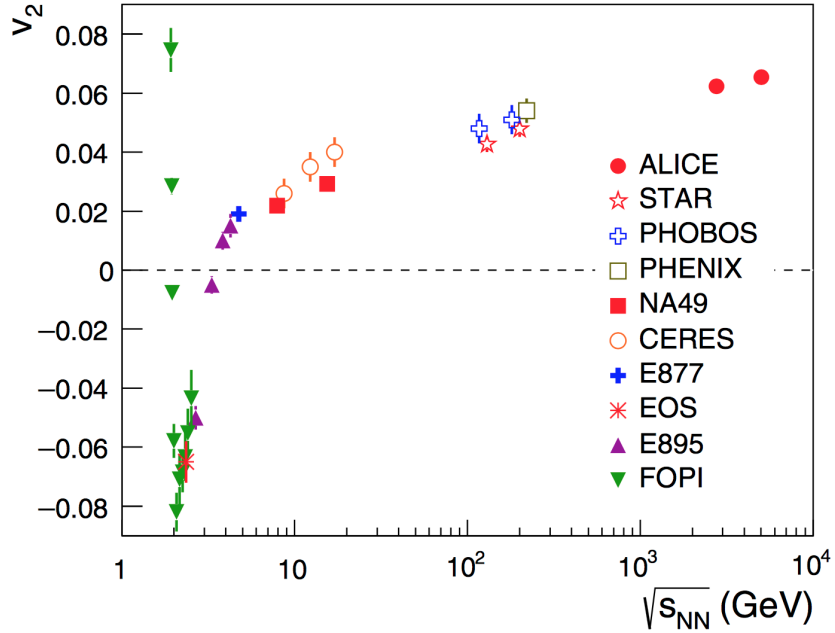


Figure 1: v_2 measured as a function of different collision energies $\sqrt{s_{\text{NN}}}$, published by ALICE.

202 ATLAS has measured the p_{T} dependence of $c_2\{4\}$ and $c_3\{4\}$ with 2.76 TeV Pb+Pb data [?], as
 203 shown in Fig. 2. For $v_2\{2\}$ and higher order cumulants, the magnitude of v_2 first increases with p_{T} ,
 204 reaches maximum around 2 – 3 GeV, then decreases as p_{T} goes even higher.

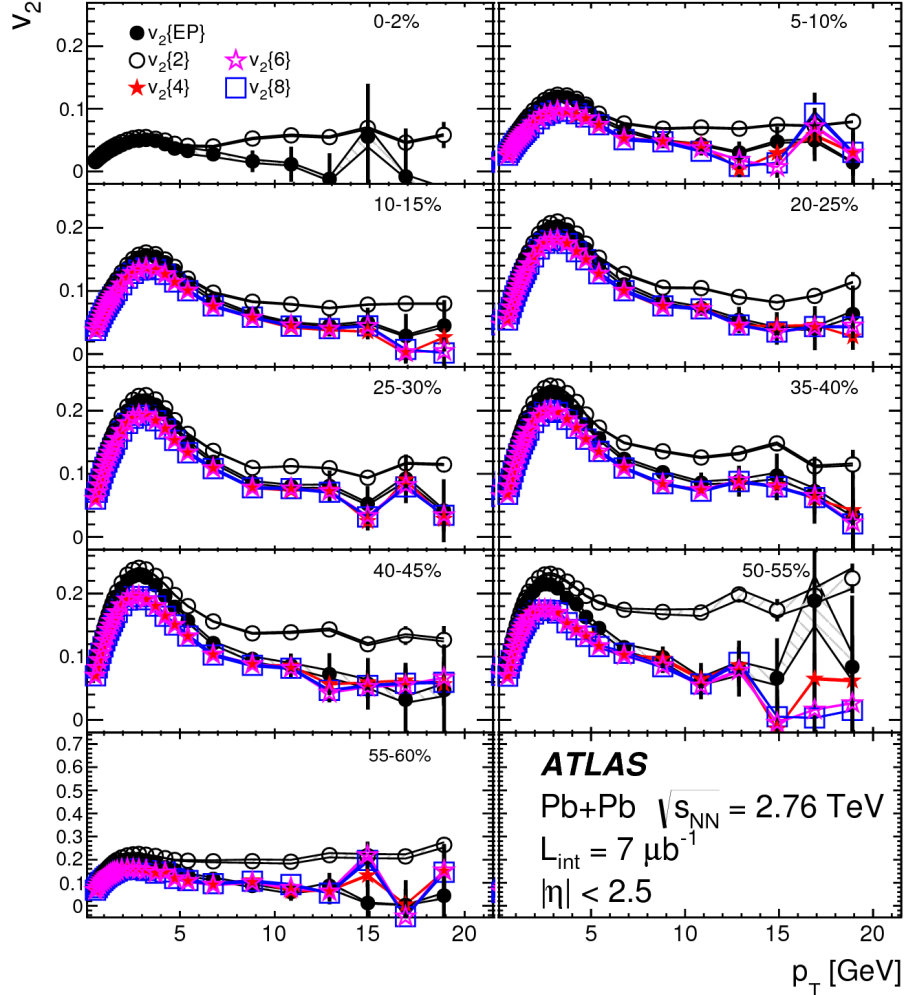


Figure 2: $v_2\{2k\}$ measured as a function of p_T , published by ATLAS

205 Note that in previous differential multi-particle cumulant measurements [15], p_T dependence are
 206 measured with respect to only one reference particles. While in this analysis, the p_T dependence are
 207 measured with all the particles. For example, to measure cumulant $c_2\{4\}$ in range $2.0 < p_T < 5.0$ GeV:

- 208 • Previous differential cumulant: in $\langle e^{in(\phi_i+\phi_j-\phi_k-\phi_l)} \rangle$, only one particle is from $2.0 < p_T < 5.0$ GeV
 209 and the rest three particles are from $0.5 < p_T < 5.0$ GeV;
 210 • This analysis: in $\langle e^{in(\phi_i+\phi_j-\phi_k-\phi_l)} \rangle$, all the four particles are from $2.0 < p_T < 5.0$ GeV;

211 The previous differential cumulant measurement assumes that the flow in different p_T ranges share the
 212 same event plane, which might not be the case as shown by the flow decorrelation measurement in
 213 p_T [16]. Note that there also exists decorrelation in η [17], but in this analysis we are only measuring
 214 cumulants as a function of p_T . With Run 2 Pb+Pb data, the statistics are higher, we are correlating all
 215 the particles in the selected p_T range, instead of correlating particles from the low p_T with high p_T . This
 216 will also benefit us in the way that the cumulant formulas are simpler than differential cumulant, without
 217 special treatment of reference particles.

218 For the measurement of v_1 , a primary background is global momentum conservation (GMC), which
 219 induces a significant dipole component. ATLAS has published the 2-particle correlation measurement
 220 of $v_1\{2\}$ at 2.76 TeV Pb+Pb [18], with momentum conservation effects properly removed, as shown

in Fig. 3. $v_1\{2\}$ as a function of p_T starts from negative values, and crosses 0 at $p_T \approx 1$ GeV. It reaches maximum positive at $p_T \approx 4$ GeV and then decreases towards very high p_T . Different centralities are shown in different panels, and the trends are very similar, meaning a weak centrality dependence of $v_1\{2\}$. Unlike 2-particle correlation, global momentum conservation does not play a role in 4-particle correlation. This is because the 4-particle cumulant is defined as:

$$c_1\{4\} = \langle v_1^4 \rangle - 2 \langle v_1^2 \rangle^2 \quad (1)$$

where GMC contributes to both $\langle v_1^4 \rangle$ and $\langle v_1^2 \rangle^2$, then most of the effects are canceled.

But in order to obtain a non-zero $c_1\{4\}$ signal, the lowest p_T cut at least needs to be above 1 GeV. Due to this reason, we have different lowest p_T cuts from 1.0 GeV to 2.0 GeV.

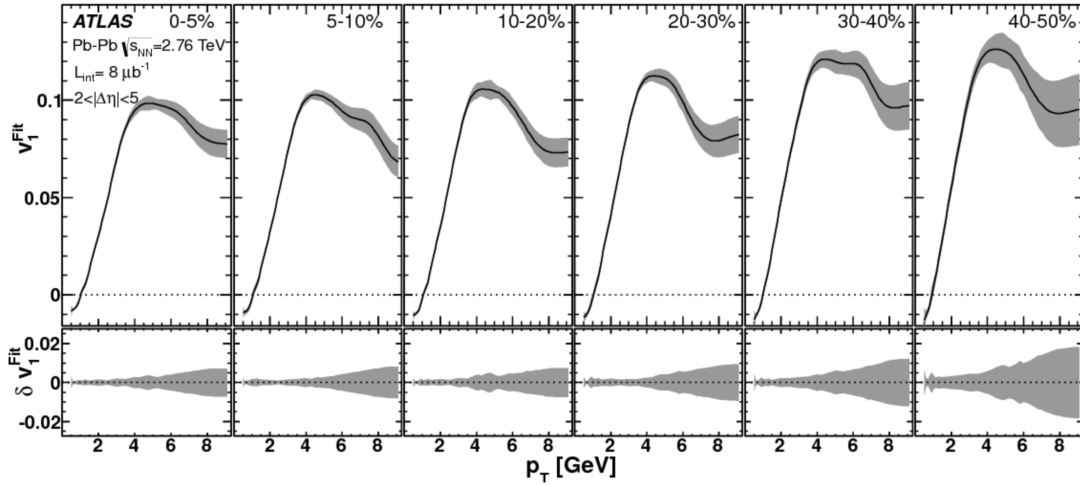


Figure 3: $v_1\{2\}$ measured as a function of p_T , in different centralities, published by ATLAS.

Symmetric cumulants, $sc_{n,m}\{4\}$, was first proposed and measured by ALICE [9], as shown in Fig. 4. Symmetric cumulants in HIJING are found to be consistent with 0, meaning that these observables are not sensitive to the non-flow contributions. In this analysis, we have extended the measurements to 5.02 TeV Pb+Pb, with multiple p_T cuts. Both the energy of p_T dependence of symmetric cumulants will provide more insights into the flow correlations.

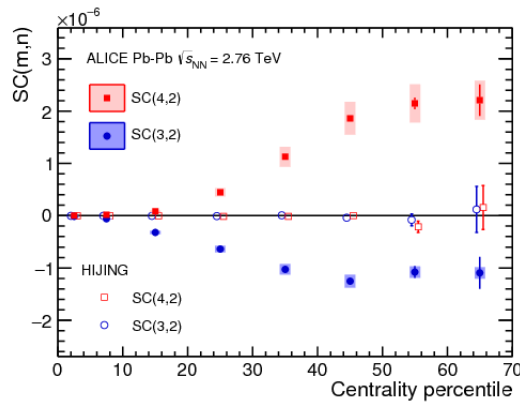


Figure 4: Symmetric cumulants $sc_{2,3}\{4\}$ and $sc_{2,4}\{4\}$ as a function of centrality, measured by ALICE.

Cumulant ratios have long been used to probe the fluctuation of eccentricity ϵ_n in the initial stage. Recently, CMS collaboration has published the non-Gaussian elliptic-flow fluctuation in 5.02 TeV Pb+Pb [19]. In the paper, they measured the cumulant ratio $v_2\{6\}/v_2\{4\}$, as shown in Fig. 5, and the method they used the unfolding technique. In this analysis, we calculated the same observable using multi-particle cumulant. One advantage of cumulant method is that the systematics partially cancels in the ratio, which results in a much better precision. Furthermore, we have tested the non-Gaussian fluctuation in different p_T ranges, which reflects the additional dynamical fluctuation after the initial stage.

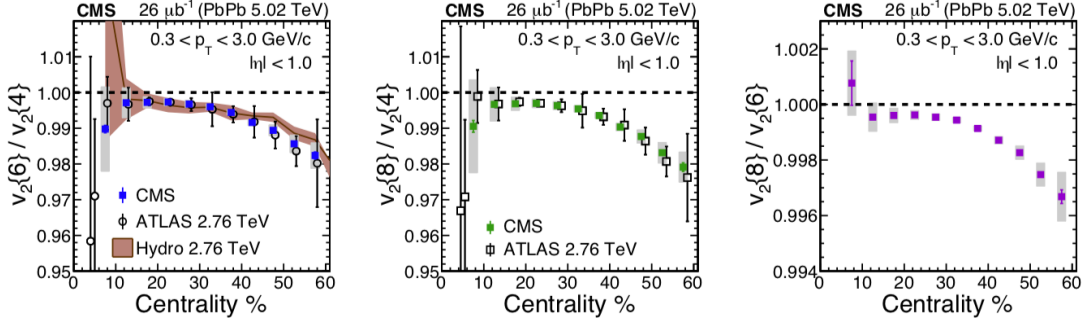


Figure 5: Cumulant ratio $v_2\{6\}/v_2\{4\}$ as a function of centrality, with unfolding method, published by CMS.

241 3 Detector, trigger and offline event selection

242 The results presented in this analysis were obtained from a sample of minimum-bias and ultra-central
 243 lead-lead collisions at $\sqrt{s_{\text{NN}}} = 5.02$ TeV recorded by ATLAS in 2015 (Run 2). The corresponding
 244 integrated luminosity are approximated $22 - 470 \mu\text{b}^{-1}$. The measurements were performed using the
 245 ATLAS inner detector and forward calorimeters. The inner detectors covers the complete azimuthal
 246 range and extends over the pseudorapidity region $|\eta| < 2.5$. The inner detector silicon tracker, used in this
 247 analysis for track reconstruction, consists of layers of pixel and microstrip detectors (SCT) immersed in
 248 a 2 T axial magnetic field. An additional pixel layer, the "Insertable B Layyer" (IBL) installed between
 249 Run 1 and Run 2 (2013-2015), is used in the 5.02 TeV Pb+Pb measurements. The MBTS system detects
 250 charged particles over $2.1 < |\eta| < 3.9$ using two hodoscopes of counters positioned at $z = \pm 3.6$ m.
 251 The forward calorimeters (FCal) use liquid argon with copper tungsten absorbers to perform both the
 252 electromagnetic and hadronic energy measurements with copper-tungsten/liquid argon technology, and
 253 also provide complete coverage in azimuthal for $3.2 < |\eta| < 4.9$. The trigger system was used to select
 254 minimum-bias lead-lead collisions. It required a coincidence of signals recorded in both zero-degree
 255 calorimeters (ZDC), located symmetrically at $z = \pm 140$ m, and in the minimum-bias trigger scintillator
 256 (MBTS, only used in Run 1) counters at $z = \pm 3.6$ m.

257 3.1 Triggers

258 The minimum-bias triggers for 5.02 TeV Pb+Pb collisions are:

- 259 • HLT_mb_sptrk_ion_L1ZDC_A_C_VTE50
- 260 • HLT_noalg_mb_L1TE50

261 where the major difference is Level-1 total energy TE: VTE50 requires total energy less than 50 GeV while
 262 TE50 larger than 50 GeV; sptrk requires at least 1 reconstructed track at the HLT level, and L1ZDC_A_C
 263 requires one hit in both sides of ZDC. These two requirements will clean up most diffractive events.
 264 In any case, this measurement stops at 80% centrality, which means the contributions from diffractive
 265 events are minimal.

266 To enhance the statistics in ultra-central events, ultra-central collision (UCC) triggers are used:

- 267 • HLT_hi_th1_ucc_L1TE10000
- 268 • HLT_hi_th2_ucc_L1TE10000
- 269 • HLT_hi_th3_ucc_L1TE10000
- 270 • HLT_hi_th1_ucc_L1TE12000
- 271 • HLT_hi_th2_ucc_L1TE12000
- 272 • HLT_hi_th3_ucc_L1TE12000
- 273 • HLT_hi_th1_ucc_L1TE14000
- 274 • HLT_hi_th2_ucc_L1TE14000
- 275 • HLT_hi_th3_ucc_L1TE14000

276 where L1TEX denotes the minimum L1 total energy cut and thX corresponds to the various minimum
 277 FCal Calorimeter E_T cut at the HLT level:

- 278 • th1: online FCal $E_T > 4.172$ TeV;
 279 • th2: online FCal $E_T > 4.326$ TeV;
 280 • th3: online FCal $E_T > 4.500$ TeV;

281 Fig. 6 shows the FCal E_T distributions seeded by two major UCC triggers, compared with those
 282 seeded by MinBias triggers. UCC triggers collected more than 20 times statistics compared with MinBias
 283 triggers in the ultra-central collisions. Meanwhile, as seen in these plots, the turn-on curves of UCC
 284 trigger efficiency are very sharp, which means small selection bias. The impact from trigger efficiency
 285 will be discussed in details in Sec. 7.

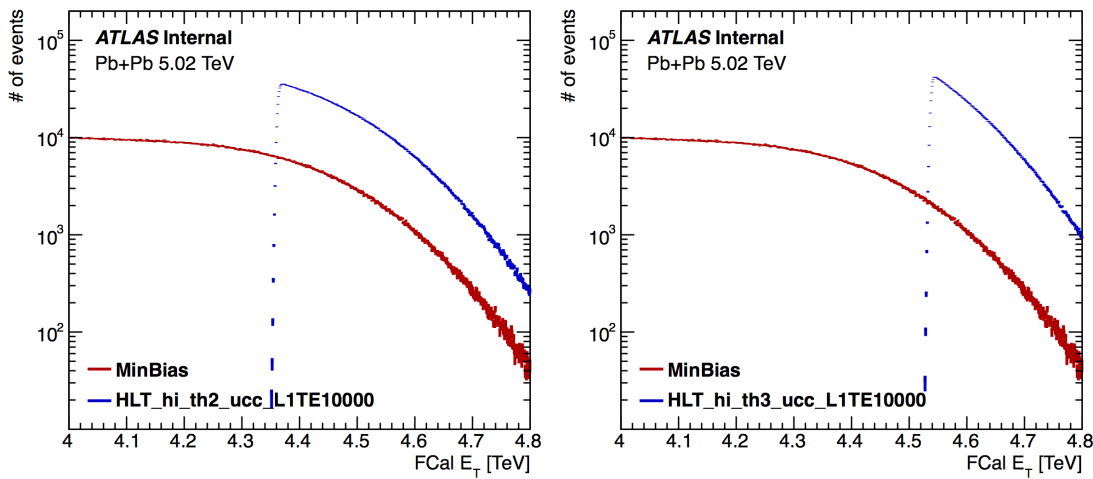


Figure 6: FCal E_T distribution for two major UCC triggers (red points), compared with MinBias trigger (blue points).

286 3.2 Event selection

287 The reconstruction version of the data set is `data15_hi.XXX.physics.MinBias.recon.AOD.r7874`.
 288 The event selections for 5.02 TeV Pb+Pb events are:

- 289 • Pass good run list (GRL): <https://twiki.cern.ch/twiki/bin/viewauth/Atlas/HeavyIonRunList>;
 290 • Have a primary reconstructed vertex;
 291 • Events with detector error tags removed:
 292 – LAr error;
 293 – Tile error;
 294 – SCT error;
 295 – Incomplete events;
 296 • Vertex position cut: $|z_{vtx}| < 100$ mm;
 297 • $0\% \leq$ centrality $< 80\%$;
 298 • Pileup rejection: https://twiki.cern.ch/twiki/bin/view/Main/HIAnalysisTools#HI_Pileup_Tool_Working;

where the definition of centrality will be discussed shortly. In this analysis we are cutting the vertex position at 100 mm instead of 150 mm (in previous Pb+Pb analysis). This is because multiplicity distribution along η changes with the z_{vtx} position, and in previous measurements it is not an issue since all the particles in $|\eta| < 2.5$ are used to calculate the cumulant. However, with the 3-subevent cumulant method, two subevents are defined with the range $2.5/3 < |\eta| < 2.5$, which is closer to the edges of the Inner Detector. In order to avoid introducing large multiplicity fluctuations in these two subevents, we further constrain the vertex position to 100 mm, and we will not lose much statistics with this tighter cut.

In the 2015 Pb+Pb run, the luminosity conditions provided by the LHC result in an average probability of 0.1% that an event contains two or more Pb+Pb collisions (pileup). The pileup events are suppressed by only using the tracks from primary vertex (in fact, in Pb+Pb, only one primary vertex is reconstructed). The remaining pileup events are further suppressed based on the correlation between the ZDC and FCal. This signal in the ZDC is calibrated to the number of detected neutrons N_n based on the location of the peak corresponding to a single neutron.

Fig. 7 shows the procedure of pileup rejection and its performance. The left plot shows the correlation between number of neutrons in the ZDC and total transverse energy E_T in the FCal. The "banana"-shaped main band (green) mainly contains events with a single vertex. While in a pileup event, both the number of neutrons and FCal $\sum E_T$ are larger than a single event, and this is indicated by the events in the "grass" (purple) region above the main band. To clean up the pileup, one way is by applying a linear cut on the correlation map, indicated by the black straight line, and another way is cutting off 0.1% of the events in the tails of N_{neutrons} distribution in each FCal E_T slice, indicated by the red curve. In this analysis, we will use the red curve as the default cut. The right plot shows the performance of the two pileup rejection methods just mentioned. The Y-axis shows the fraction of rejected pileup events out of all the pileup events. The rejection rate is low at low FCal E_T , this is because the band for pileup events most overlaps with the main band for single events. However, since the fraction of pileup events is very low in peripheral collisions, the low rejection rate has no impact on the results. On the other hand, the rejection rate reaches 100% in ultra-central collision, where the fraction of pileup event is high, meaning that almost all the pileup events are rejected using the HI pileup rejection tool.

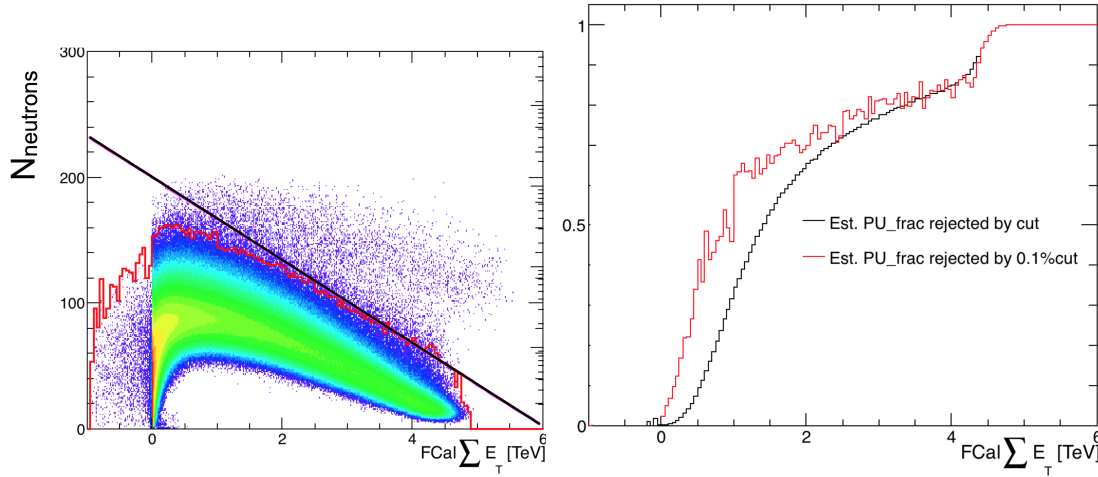


Figure 7: Left plot shows the correlation between calibrated number of neutrons in the ZDC and FCal $\sum E_T$. Right plot shows the fraction of rejected pileup events in all pileup events. Two rejection criteria are shown: a linear cut and 0.1% cut.

Fig. 8 illustrates the FCal sum E_T distribution before and after this pileup cut, as well as the fraction of events that are rejected as a function of FCal sum E_T . As expected, the rejection rate is < 0.2% for FCal $E_T < 4.5$ TeV, and increases toward 1 quickly as FCal E_T increases.

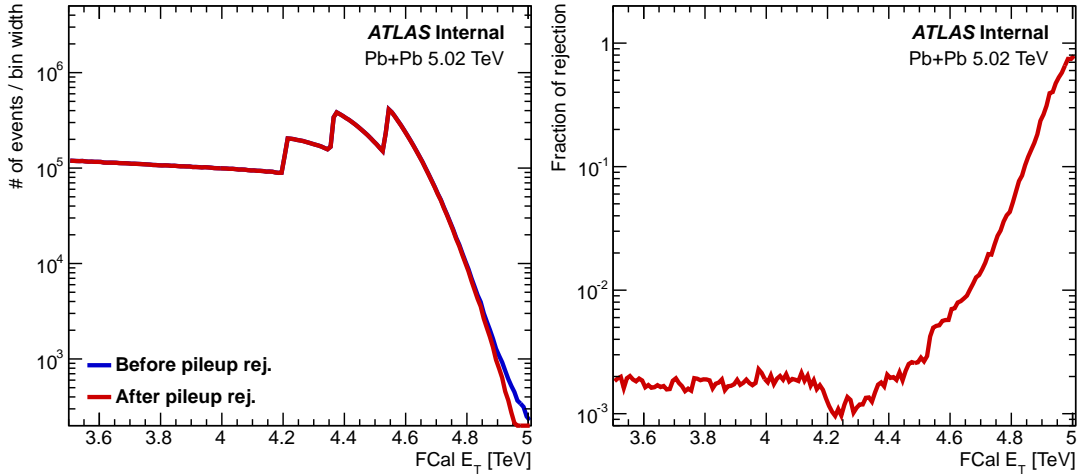


Figure 8: Left plot shows the FCal sum E_T distribution before and after applying the HI pileup tool. Right plot shows the fraction of events that are rejected by this tool, as a function of FCal sum E_T .

Furthermore, in order to further suppress the residual pileup events, an additional cut has been applied on the correlation map between FCal E_T and efficiency corrected reconstructed number of tracks N_{ch} . Fig. 9 shows the correlation froms MinBias events (left), and UCC events collected with one of the UCC triggers (right) as a demonstration. Since pileup events have relatively larger FCal E_T than normal events, the pileup events should fall under the main correlation band. From the correlation map, some "grass" is indeed observed. To determine the cut, a Gaussian fitting is applied to the N_{ch} distribution for each FCal E_T slice, and the events beyond 5σ are rejected (indicated by the red dots). To reach the high FCal E_T region, where the performance of Gaussian fit is poor (because of the additional structure from pileup events), a linear cut is determined by fitting the red dots in the region FCal $E_T < 4, 7$ TeV. Events below this linear cut are rejected.

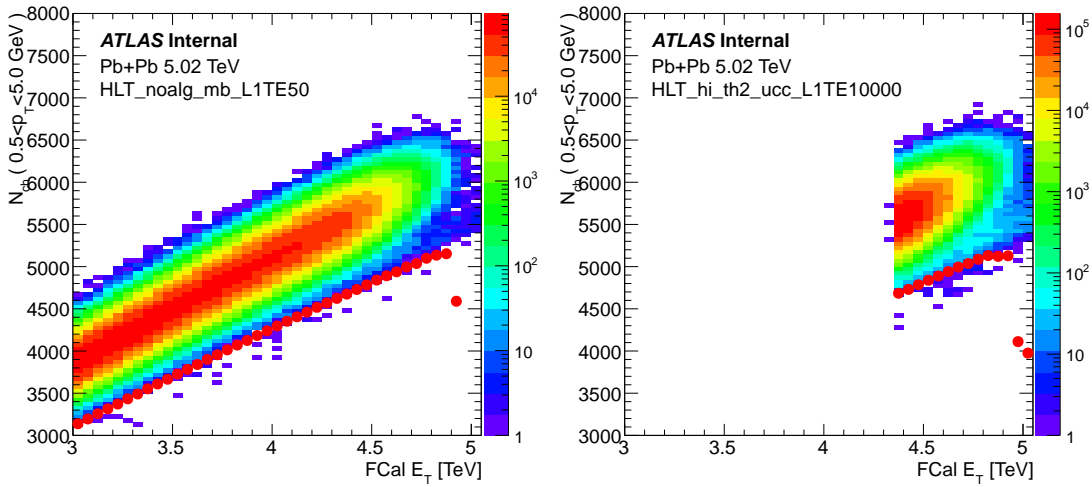


Figure 9: Correlation between FCal E_T and N_{ch} in the ultra-central collisions. The red dots indicate the 5σ position of the Gaussian fit in each N_{ch} slice at fixed FCal E_T . The actual cut is a linear fit of the red points in order to reach the largest FCal $\sum E_T$ region.

³⁴⁰ 3.3 Centrality

³⁴¹ The details of centrality cuts are documented here: https://twiki.cern.ch/twiki/bin/view/AtlasProtected/HeavyIonAnalysis2015#NEW_Centrality_Recommendations_f. The Pb+Pb
³⁴² event centrality is characterized using the total transverse energy ($\sum E_T$) deposited in the FCal detector
³⁴³ at the electromagnetic energy scale. An analysis of this distribution after all triggers and event selections
³⁴⁴ gives an estimation of the fraction of the sampled non-Coulomb inelastic cross-section to be $85\% \pm 1\%$.
³⁴⁵ This estimate is obtained from a shape analysis of the measured FCal $\sum E_T$ distributions compared with
³⁴⁶ a convolution of proton-proton data with a Monte Carlo Glauber calculation. The FCal $\sum E_T$ distribution
³⁴⁷ is then divided into a set of 1% percentile bins, together with a bin defined for the 0.1% most central
³⁴⁸ events. The uncertainty associated with the centrality definition is evaluated by varying the effect of trig-
³⁴⁹ ger and event selection inefficiencies as well as background rejection requirements in the most peripheral
³⁵⁰ FCal $\sum E_T$ interval.
³⁵¹

³⁵² The centrality interval and corresponding number of participants N_{part} estimated from Glauber model
 are listed in Table. 1

Centrality	0-5%	5-10%	10-15%	15-20%	20-25%	25-30%	30-35%	35-40%
N_{part}	384.5	333.1	285.2	242.9	205.6	172.8	144.1	118.8
Centrality	40-45%	45-50%	50-55%	55-60%	60-65%	65-70%	70-75%	75-80%
N_{part}	96.6	77.4	60.9	47.0	35.2	25.8	18.3	12.5

Table 1: Centrality intervals and corresponding number of participants N_{part} estimated from Glauber model in Run 2.

354 4 Track selection, efficiency and fakes

355 4.1 Track selection

356 The track selection for 5.02 TeV Pb+Pb follows the standard cut implemented in the xAOD ToolInDet:
 357 Loose quality cut is denoted as `HILoose` and is defined as:

- 358 • $p_T > 500$ MeV;
- 359 • number of Pixel hits > 0 ;
- 360 • number of SCT hits + dead sensors ≥ 6 ;
- 361 • if IBL hit is expected: at least 1 IBL hit required;
- 362 • if no IBL hit is expected: a Layer-0 hit if expected;
- 363 • $|d_0| \leq 1.5$ mm;
- 364 • $|z_0 - z_{\text{vtx}}| * \sin\theta \leq 1.5$ mm;

365 where "ndf" denotes number of degree of freedom of the track.

366 Tight quality cut is denoted as `HITight` and is defined as:

- 367 • $p_T > 500$ MeV;
- 368 • *** number of Pixel hits > 1 ;
- 369 • *** number of SCT hits + dead sensors ≥ 8 ;
- 370 • if IBL hit is expected: at least 1 IBL hit required;
- 371 • if no IBL hit is expected: a Layer-0 hit if expected;
- 372 • *** $|d_0| \leq 1.0$ mm;
- 373 • *** $|z_0 - z_{\text{vtx}}| * \sin\theta \leq 1.0$ mm;
- 374 • *** $\chi^2/\text{ndf} \leq 6$;

375 where the differences compared with loose cut are highlighted with "***". In this analysis, the default
 376 track selection is the loose quality cut, and tight quality cut is used as a systematic check and is discussed
 377 in Section 7. We prefer `HILoose` over `HITight` mainly because there are more particles remaining with
 378 the loose cut, which results in smaller statistical uncertainties. The loose and tight cuts are determined by
 379 evaluating the tracking efficiency and fake rates in the Monte-Carlo samples with same detector condi-
 380 tions as during the data taking and these two cuts results in relatively lower fake rates with high tracking
 381 efficiency.

382 4.2 Tracking in Monte-Carlo

383 To estimate the tracking efficiency and fake rate in 5.02 TeV Pb+Pb, HIJING Monte-Carlo samples with
 384 similar detector conditions and flow after-burner [20] are used:

- 385 • `mc15_5TeV.420000.Hijing_PbPb_5p02TeV_MinBias_Flow_JJFV6.recon.AOD.`
- 386 `e4962_a868_s2921_r9447`

387 Within the reconstructed tracks, the primary tracks $N_{ch}^{primary}$ are defined as:

- 388 • pass the loose track quality selection;
- 389 • truth match probability > 0.5 ;
- 390 • associated truth particle is a primary particle;

391 where primary particle is defined on the truth level:

- 392 • status = 1, charge != 0;
- 393 • $p_T > 200$ MeV;
- 394 • $|\eta| \leq 2.5$;
- 395 • $0 < \text{Barcode} < 2E5$;
- 396 • strange baryons are excluded;

397 The tracking efficiency ϵ is then defined as:

$$\epsilon(p_T, \eta, \text{centrality}) \equiv \frac{N_{ch}^{primary}}{N_{ch}^{truth}} \quad (2)$$

398 where $N_{ch}^{primary}$ denotes the number of primary tracks on reconstructed level and N_{ch}^{truth} denotes the num-
399 ber of primary particles on the truth level, all of which passed the loose quality selection.

400 The fake track is defined as:

- 401 • pass the loose track quality selection;
- 402 • fulfill one of the following:
 - 403 – truth match probability < 0.5 ;
 - 404 – not associated with truth particles;
 - 405 – Barcode = 0 of associated truth particle;

406 The fraction of fake tracks f is defined as:

$$f(p_T, \eta, \text{centrality}) \equiv \frac{N_{ch}^{fake}}{N_{ch}^{primary} + N_{ch}^{fake}} \quad (3)$$

407 where N_{ch}^{fake} denotes the number of fake tracks.

408 To compensate the contribution from fake tracks, the efficiency ϵ can be corrected by defining ϵ' :

$$\epsilon' (p_T, \eta, \text{centrality}) \equiv \frac{N_{ch}^{primary} + N_{ch}^{fake}}{N_{ch}^{truth}} = \frac{\epsilon}{1 - f} \quad (4)$$

409 where an additional correction of fake rates $1 - f$ is added to the tracking efficiency ϵ .

410 4.3 Efficiency

411 The tracking efficiency map used in this analysis is borrowed from Run 2 v_n analysis [21], which is
 412 evaluated as a function of p_T, η and centrality. To estimate the tracking efficiency, the track selection
 413 follows the loose quality cut. The tracking efficiency $\epsilon(\eta)$ are shown in Fig. 10, for different p_T ranges
 414 and centrality. $\epsilon(\eta)$ is highest in mid-rapidity $-1 < \eta < 1$, and decreases by 20% in forward-rapidity. As
 415 collision moves to peripheral, the efficiency increases. The tracking efficiency slightly increases towards
 416 higher p_T . Efficiency from HILOOSE is higher than HITIGHT as expected.

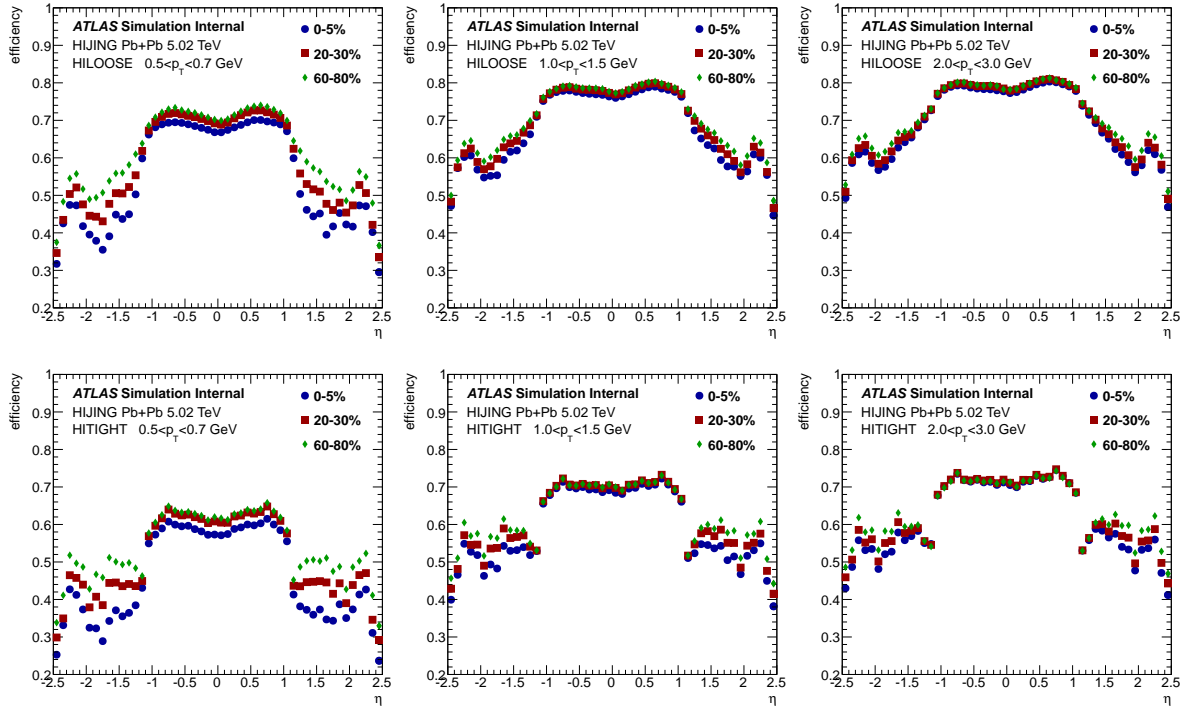


Figure 10: 5.02 TeV Pb+Pb tracking efficiency $\epsilon(\eta)$, for different p_T ranges and centralities. Top row is for loose track quality cut (default) and bottom row is for tight cut.

417 4.4 Fakes

418 Since one of the focuses in this analysis is on ultra-central collisions, fake rate correction $1 - f$ were
 419 applied to the efficiency ϵ and each track is weighted by $(1 - f)/\epsilon$. The fake rates map is also borrowed
 420 from Run 2 v_n analysis [21], which is evaluated as a function of p_T, η and centrality. To estimate the
 421 fraction of fake tracks, the track selection follows the loose quality cut. The fake rate $f(\eta)$ are shown in
 422 Fig. 11, for different p_T ranges and centrality. $f(\eta)$ is lowest in mid-rapidity $-1 < \eta < 1$, and increases
 423 by more than 2 times in forward-rapidity. As collision moves to peripheral, the fake rate significantly
 424 decreases. The fake rate decreases significantly towards higher p_T . Fake rate from HILOOSE is higher
 425 than HITIGHT as expected.

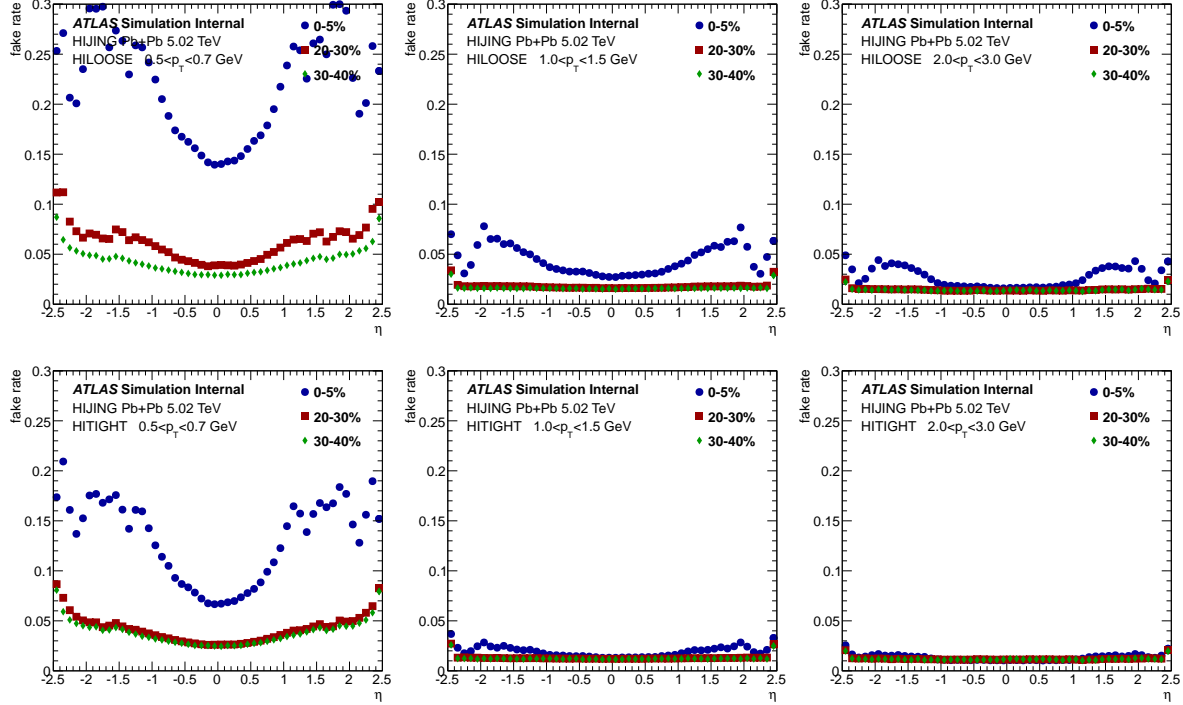


Figure 11: 5.02 TeV Pb+Pb tracking fake rates $f(\eta)$, for different p_T ranges and centralities. Top row is for loose track quality cut (default) and bottom row is for tight cut.

426 5 Methodology

427 5.1 Outline

428 The details of cumulant analysis are carried out in the following procedures:

- 429 • Calculation of 2-, 4- and 6-particle correlation $\text{corr}_n\{2k\}$:

- 430 – Standard cumulant method;
- 431 – 3-subevent cumulant method;

- 432 • Calculation of 2-, 4- and 6-particle cumulant $c_n\{2k\}$:

- 433 – Standard cumulant method;
- 434 – 3-subevent cumulant method;

- 435 • Calculation of 2-, 4- and 6-particle flow signal $v_n\{2k\}$;

- 436 • Calculation of normalized cumulant $nc_n\{2k\}$;

- 437 • Universality check of flow fluctuation models;

- 438 • Calculation of symmetric cumulant $sc_{n,m}\{4\}$ and $nsc_{n,m}\{4\}$:

- 439 – Standard symmetric cumulant method;
- 440 – 3-subevent symmetric cumulant method;

- 441 • Calculation of asymmetric cumulant $ac_{n,n+m}\{3\}$ and $nac_{n,n+m}\{3\}$:

- 442 – Standard asymmetric cumulant method;
- 443 – 3-subevent asymmetric cumulant method;

444 5.2 Calculation of 2-, 4- and 6-particle correlation $\text{corr}_n\{2k\}$

445 2-, 4- and 6-particle correlations are defined as:

$$\begin{aligned} \text{corr}_n\{2\} &\equiv \left\langle e^{in(\phi_i - \phi_j)} \right\rangle \\ \text{corr}_n\{4\} &\equiv \left\langle e^{in(\phi_i + \phi_j - \phi_k - \phi_l)} \right\rangle \\ \text{corr}_n\{6\} &\equiv \left\langle e^{in(\phi_i + \phi_j + \phi_k - \phi_l - \phi_m - \phi_n)} \right\rangle \end{aligned} \quad (5)$$

446 where notation $\text{corr}_n\{2k\}$ is used for the $2k$ -particle correlations and n denotes harmonic n in the Fourier
447 coefficients v_n . i, j, k, l, m, n denotes unique particles in certain phase space (p_T, η) , which will be quan-
448 tified in the analysis section. $\langle \dots \rangle$ is the weighted average calculated for each event

$$\begin{aligned} \left\langle e^{in(\phi_i - \phi_j)} \right\rangle &\equiv \frac{\sum' w_i w_j e^{in(\phi_i - \phi_j)}}{\sum' w_i w_j} \\ \left\langle e^{in(\phi_i + \phi_j - \phi_k - \phi_l)} \right\rangle &\equiv \frac{\sum' w_i w_j w_k w_l e^{in(\phi_i + \phi_j - \phi_k - \phi_l)}}{\sum' w_i w_j w_k w_l} \\ \left\langle e^{in(\phi_i + \phi_j + \phi_k - \phi_l - \phi_m - \phi_n)} \right\rangle &\equiv \frac{\sum' w_i w_j w_k w_l w_m w_n e^{in(\phi_i + \phi_j + \phi_k - \phi_l - \phi_m - \phi_n)}}{\sum' w_i w_j w_k w_l w_m w_n} \end{aligned} \quad (6)$$

449 where \sum' means the summation of unique particles: i.e. $i \neq j$, $i \neq j \neq k \neq l$ and $i \neq j \neq k \neq l \neq m \neq n$
 450 respectively. w is the weight applied to each particle, which is a combination of tracking efficiency ϵ ,
 451 fraction of fake tracks f and trigger re-weighting w_{trig} :

$$w \equiv \frac{w_\phi(1-f)}{\epsilon} \quad (7)$$

452 where all these weights will be discussed in details in the cumulant analysis section 6.

453 The most straightforward way to calculate $2k$ -particle correlation $corr_n\{2k\}$ is called nested loop
 454 method: counting all the possible unique combinations within $2k$ nested loops of tracks. Since nested
 455 loop method has a complexity of $\mathcal{O}(M^{2k})$, where M is the multiplicity in each event, it requires a lot
 456 of CPU hours to compute the 6-particle correlation, especially in Pb+Pb collision. An equivalent way
 457 is named as Q -cumulant (or direct-cumulant) method, which calculates $corr_n\{2k\}$ in a single loop, thus
 458 greatly reduces the complexity to $\mathcal{O}(M)$. The Q -cumulant method carefully removes all the correlations
 459 between same particles ("duplicates") by using simple diagrams. In this note, we will only list all the
 460 formula using Q -cumulant, without going into details about the derivation, and we have confirmed that
 461 both nested loop and Q -cumulant methods give identical results, which validates all the formulas we
 462 have used for the Q -cumulant method.

463 5.2.1 Standard Q -cumulant method

464 The event-by-event $\mathbf{Q}_{n,k}$ vector in standard cumulant method is defined as:

$$\mathbf{Q}_{n,k} \equiv \sum w_i^k e^{in\phi_i} \quad (8)$$

465 where w_i is the particle weight introduced earlier and the power k is for the purpose of removing dupli-
 466 cates. n denotes the harmonic n from the Fourier coefficients v_n .

467 In order to simply the expression, $S_{p,k}$ is introduced as:

$$S_{p,k} \equiv (\sum w_i^k)^p \quad (9)$$

468 where k in $S_{p,k}$ is the same one with k in $\mathbf{Q}_{n,k}$. Note that unlike $\mathbf{Q}_{n,k}$, $S_{p,k}$ is not related to the azimuthal
 469 angle ϕ of each particle.

470 The $\mathbf{Q}_{n,k}$ and $S_{p,k}$ are defined in this way so that $2k$ -particle correlation $corr_n\{2k\}$ can be expressed
 471 as a function of $\mathbf{Q}_{n,k}$ and $S_{p,k}$:

$$corr_n\{2k\} = f(\mathbf{Q}_{n,k}, S_{p,k}) \quad (10)$$

472 The event-by-event 2-, 4- and 6-particle correlations in the standard Q -cumulant method can then be
 473 written as [6]:

$$\begin{aligned} corr_n\{2\} &= \frac{|\mathbf{Q}_{n,1}|^2 - S_{1,2}}{S_{2,1} - S_{1,2}} \\ corr_n\{4\} &= \frac{|\mathbf{Q}_{n,1}|^4 + |\mathbf{Q}_{2n,2}|^2 - 2\mathcal{R}e(\mathbf{Q}_{2n,2}\mathbf{Q}_{n,1}^*\mathbf{Q}_{n,1}) + 8\mathcal{R}e(\mathbf{Q}_{n,3}\mathbf{Q}_{n,1}^*) - 4S_{1,2}|\mathbf{Q}_{n,1}|^2 + 2S_{2,2} - 6S_{1,4}}{S_{4,1} + 8S_{1,3}S_{1,1} - 6S_{1,2}S_{2,1} + 3S_{2,2} - 6S_{1,4}} \\ corr_n\{6\} &= (|\mathbf{Q}_{n,1}|^6 - 6|\mathbf{Q}_{n,1}|^2\mathcal{R}e(\mathbf{Q}_{2n,2}\mathbf{Q}_{n,1}^*\mathbf{Q}_{n,1}) + 9|\mathbf{Q}_{2n,2}|^2|\mathbf{Q}_{n,1}|^2 + 4\mathcal{R}e(\mathbf{Q}_{3n,3}\mathbf{Q}_{n,1}^*\mathbf{Q}_{n,1}\mathbf{Q}_{n,1}^*)) \\ &\quad + 18S_{1,2}\mathcal{R}e(\mathbf{Q}_{2n,2}\mathbf{Q}_{n,1}^*\mathbf{Q}_{n,1}^*) - 36\mathcal{R}e(\mathbf{Q}_{2n,4}\mathbf{Q}_{n,1}^*\mathbf{Q}_{n,1}^*) - 36\mathcal{R}e(\mathbf{Q}_{n,3}\mathbf{Q}_{n,1}\mathbf{Q}_{2n,2}^*) + 18S_{2,2}|\mathbf{Q}_{n,1}|^4 \\ &\quad - 54S_{1,4}|\mathbf{Q}_{n,1}|^2 - 72S_{1,2}\mathcal{R}e(\mathbf{Q}_{n,3}\mathbf{Q}_{n,1}^*) + 36|\mathbf{Q}_{n,3}|^2 + 144\mathcal{R}e(\mathbf{Q}_{n,5}\mathbf{Q}_{n,1}^*) - 9S_{1,2}|\mathbf{Q}_{n,1}|^4 \\ &\quad + 36|\mathbf{Q}_{n,1}|^2\mathcal{R}e(\mathbf{Q}_{n,3}\mathbf{Q}_{n,1}^*) - 9S_{1,2}|\mathbf{Q}_{2n,2}|^2 + 36\mathcal{R}e(\mathbf{Q}_{2n,4}\mathbf{Q}_{2n,2}^*) - 12\mathcal{R}e(\mathbf{Q}_{3n,3}\mathbf{Q}_{2n,2}^*\mathbf{Q}_{n,1}^*) \\ &\quad + 4|\mathbf{Q}_{3n,3}|^2 + 54S_{1,4}S_{1,2} - 6S_{3,2} - 120S_{1,6})/(S_{6,1} - 15S_{1,2}S_{4,1} + 40S_{1,3}S_{3,1} + 45S_{2,2}S_{2,1} \\ &\quad - 90S_{1,4}S_{2,1} - 120S_{1,3}S_{1,2}S_{1,1} - 15S_{3,2} + 144S_{1,5}S_{1,1} + 90S_{1,4}S_{1,2} + 40S_{2,3} - 120S_{1,6}) \end{aligned} \quad (11)$$

⁴⁷⁴ **5.2.2 3-subevent Q -cumulant method**

⁴⁷⁵ Compared with standard method, the format of $\text{corr}_n\{2k\}$ are slightly altered in the 3-subevent method:

$$\begin{aligned} \text{corr}_n^{a|b}\{2\} &\equiv \left\langle e^{in(\phi_a - \phi_b)} \right\rangle \\ \text{corr}_n^{a,a|b,c}\{4\} &\equiv \left\langle e^{in(\phi_a + \phi'_a - \phi_b - \phi_c)} \right\rangle \end{aligned} \quad (12)$$

⁴⁷⁶ where notation $a|b$ and $a,a|b,c$ are added to the superscript of $\text{corr}_n\{2k\}$ to distinguish formula from the
⁴⁷⁷ standard method. Moreover, particles i, j, k and l come from 3 subevents with different η ranges:

- ⁴⁷⁸ • ϕ_a : ϕ angle of particle from subevent a;
- ⁴⁷⁹ • ϕ_b : ϕ angle of particle from subevent b;
- ⁴⁸⁰ • ϕ_c : ϕ angle of particle from subevent c;
- ⁴⁸¹ • ϕ'_a : ϕ angle of particle from subevent a, but different from ϕ_a ;

⁴⁸² One of the main reasons to measure cumulant is to suppress non-flow contribution, which originates
⁴⁸³ from resonance decay, HBT, jet correlation and so on. In contrast to flow, non-flow usually has fewer
⁴⁸⁴ particles associated with. By measuring the multi-particle correlation, those non-flow contributions can
⁴⁸⁵ be mostly removed. However, for example, in the jet scenario, more than 3 particles can be correlated
⁴⁸⁶ with each other, which can not be removed using the standard cumulant method. Due to this reason,
⁴⁸⁷ subevent cumulant method is introduced to suppress the residual non-flow. In 3 subevent method, since
⁴⁸⁸ the 4 particles are required to come from 3 subevents across the whole η range, short-range (in η) non-
⁴⁸⁹ flow correlations are greatly suppressed. Furthermore, 3-subevent is also robust at reducing long-range
⁴⁹⁰ non-flow correlations, i.e. back-to-back di-jet correlation. The two correlated jets can only fall into two
⁴⁹¹ out of the three subevents, thus there will always be at least one particle in $\text{corr}_n\{4\}$ that is not associated
⁴⁹² with the di-jet. After averaging all the combinations, the di-jet correlation is significantly suppressed.
⁴⁹³ The residual di-jet contribution can be easily evaluated by introducing small η gaps between 3 subevents.

⁴⁹⁴ The subevent method has been extensively studied and validated in Monte-Carlo models as well as
⁴⁹⁵ pp data, where the non-flow contribution is much larger than Pb+Pb . The whole purpose of showing
⁴⁹⁶ subevent results is to confirm that the non-flow is negligible in Pb+Pb : the final results will be pre-
⁴⁹⁷ sented using standard cumulant method after showing it gives same results as subevent method, since
⁴⁹⁸ one advantage of standard method is that it has smaller statistical uncertainties. Due to the same reason,
⁴⁹⁹ 6-particle cumulant is only calculated using standard method, as the fraction of non-flow that containing
⁵⁰⁰ 6 or more particles is significantly lower.

⁵⁰¹ Due to symmetry, there are other five ways to construct $\text{corr}_n\{4\}$ in 3-subevent:

$$\begin{aligned} \text{corr}_n^{b,b|c,a}\{4\} &\equiv \left\langle e^{in(\phi_b + \phi'_b - \phi_c - \phi_a)} \right\rangle \\ \text{corr}_n^{c,c|a,b}\{4\} &\equiv \left\langle e^{in(\phi_c + \phi'_c - \phi_a - \phi_b)} \right\rangle \\ \text{corr}_n^{a,b|a,c}\{4\} &\equiv \left\langle e^{in(\phi_a + \phi_b - \phi'_a - \phi_c)} \right\rangle \\ \text{corr}_n^{b,c|b,a}\{4\} &\equiv \left\langle e^{in(\phi_b + \phi_c - \phi'_b - \phi_a)} \right\rangle \\ \text{corr}_n^{c,a|c,b}\{4\} &\equiv \left\langle e^{in(\phi_c + \phi_a - \phi'_c - \phi_b)} \right\rangle \end{aligned} \quad (13)$$

⁵⁰² where the first two cases are simply permutations on the default configuration of four particles: 2 particles
⁵⁰³ can come from either subevent a, b or c; These two cases are independent from the default and together

504 all three cases will be included in the 3-subevent cumulant calculation of this analysis. We will briefly
 505 discuss how to merge the $\text{corr}_n\{4\}$ from these three cases later. While for the last three cases, since
 506 terms like $\phi_a - \phi'_a$ calculates the correlation within one subevent, which contains much larger fraction of
 507 short-range non-flow contribution. So in this analysis, we will not include the last three cases.

508 Compared with standard cumulant method, since the number of duplicates in summation \sum are sig-
 509 nificantly less, the formula of $\text{corr}_n\{2k\}$ for 3-subevent is much simpler:

$$\begin{aligned} \text{corr}_n^{a|b}\{2\} &= \frac{\mathcal{R}e(\mathbf{Q}_{n,1}^a \mathbf{Q}_{n,1}^{b*})}{S_{1,1}^a S_{1,1}^b} \\ \text{corr}_n^{a,a|b,c}\{4\} &= \frac{\mathcal{R}e(\mathbf{Q}_{n,1}^a \mathbf{Q}_{n,1}^{b*} \mathbf{Q}_{n,1}^a \mathbf{Q}_{n,1}^{c*}) - \mathcal{R}e(\mathbf{Q}_{n,1}^a \mathbf{Q}_{n,1}^{b*} \mathbf{Q}_{n,1}^c)}{(S_{2,1}^a - S_{1,2}^a) S_{1,1}^b S_{1,1}^c} \end{aligned} \quad (14)$$

510 The other similar configurations $\text{corr}_n^{b|c}\{2\}$, $\text{corr}_n^{c|a}\{2\}$, $\text{corr}_n^{b,b|c,a}\{4\}$ and $\text{corr}_n^{c,c|a,b}\{4\}$ can be easily
 511 written by permutations of the indices a , b and c .

512 5.3 Calculation of 2-, 4- and 6-particle cumulant $c_n\{2k\}$

513 In the last section, event-by-event $2k$ -particle correlation $\text{corr}_n\{2k\}$ has been calculated. In this section,
 514 we will calculate the $2k$ -particle cumulant by combining $\text{corr}_n\{2k\}$ with different orders.

515 Cumulant is defined on the ensemble of similar events, noted as "event class". The average of
 516 $\text{corr}_n\{2k\}$ in each event class is defined as:

$$\langle \text{corr}_n\{2k\} \rangle \equiv \frac{\sum W_i\{2k\} \text{corr}_n\{2k\}}{\sum W_i\{2k\}} \quad (15)$$

517 where the summation \sum is over every event in one event class. $W_i\{2k\}$ is the number of unique multi-
 518 plets in each event, which will be defined later. Event weight from trigger prescale w_{trig} should also be
 519 multiplied to $W_i\{2k\}$ (see Sec.6). Since cumulant measures the flow fluctuation within one event class,
 520 how the event class is defined could change the magnitude, even the sign of cumulants. For the analysis
 521 the default event class definition is centrality, with 1% as the bin width. But in the analysis section we
 522 will dive into more variations of the definitions of event class.

523 $2k$ -particle cumulant is defined as a combination of 2-, 4- ... $2k$ -particle correlation:

$$c_n\{2k\} \equiv f(\text{corr}_n\{2\}, \text{corr}_n\{4\}, \dots, \text{corr}_n\{2k\}) \quad (16)$$

524 where all the lower order terms $\text{corr}_n\{2\}$, $\text{corr}_n\{4\}$, ..., $\text{corr}_n\{2k-2\}$ are used to remove the lower-order-
 525 particle correlation from $2k$ -particle correlation and the final remaining $c_n\{2k\}$ is referred as "genuine"
 526 particle correlation, which corresponds to flow or collectivity. With the idea of subevent introduced, the
 527 formula of subevent cumulant will also slightly change compared with standard cumulant, which will be
 528 discussed in details in the following sections.

529 5.3.1 Standard cumulant

530 Without particle weights, the event weight is simply defined as number of combinations in an event:

$$\begin{aligned} W\{2\} &\equiv M(M-1) \\ W\{4\} &\equiv M(M-1)(M-2)(M-3) \\ W\{6\} &\equiv M(M-1)(M-2)(M-3)(M-4)(M-5) \end{aligned} \quad (17)$$

531 where M is the multiplicity in each event. With particle weights, the formula are more complicated due
 532 to the duplicates (correlation among same particles):

$$\begin{aligned} W\{2\} &\equiv S_{2,1} - S_{1,2} \\ W\{4\} &\equiv S_{4,1} + 8S_{1,3}S_{1,1} - 6S_{1,2}S_{2,1} + 3S_{2,2} - 6S_{1,4} \\ W\{6\} &\equiv S_{6,1} - 15S_{1,2}S_{4,1} + 40S_{1,3}S_{3,1} + 45S_{2,2}S_{2,1} - 90S_{1,4}S_{2,1} - 120S_{1,3}S_{1,2}S_{1,1} - 15S_{3,2} \\ &\quad + 144S_{1,5}S_{1,1} + 90S_{1,4}S_{1,2} + 40S_{2,3} - 120S_{1,6} \end{aligned} \quad (18)$$

533 where $S_{p,k}$ is defined in earlier sections. Note that the event weights are also the denominators of the
 534 $2k$ -particle correlations.

535 Finally, 2-, 4- and 6-particle cumulants are defined as:

$$\begin{aligned} c_n\{2\} &= \langle \text{corr}_n\{2\} \rangle; \\ c_n\{4\} &= \langle \text{corr}_n\{4\} \rangle - 2 \langle \text{corr}_n\{2\} \rangle^2; \\ c_n\{6\} &= \langle \text{corr}_n\{6\} \rangle - 9 \langle \text{corr}_n\{4\} \rangle \langle \text{corr}_n\{2\} \rangle + 12 \langle \text{corr}_n\{2\} \rangle^3; \end{aligned} \quad (19)$$

536 5.3.2 3-subevent cumulant

537 Without particle weights, the event weight is simply defined as number of combinations in an event:

$$\begin{aligned} W^{a|b}\{2\} &\equiv M_a M_b \\ W^{a,a|b,c}\{4\} &\equiv M_a(M_a - 1)M_b M_c \end{aligned} \quad (20)$$

538 where M_a and M_b are multiplicity in subevent a and b repectively. Superscripts $a|b$ and $a,a|b,c$ are used
 539 to label the configurations of 3-subevents, and there are other two configurations for $W\{4\}$: $W^{b,b|c,a}\{4\}$
 540 and $W^{c,c|a,b}\{4\}$, which can be easily derived by permutation of the indices a, b and c . Similarly, the event
 541 weights with particle weights are:

$$\begin{aligned} W^{a|b}\{2\} &\equiv S_{1,1}^a S_{1,1}^b \\ W^{a,a|b,c}\{4\} &\equiv (S_{2,1}^a - S_{1,2}^a) S_{1,1}^b S_{1,1}^c \end{aligned} \quad (21)$$

542 2- and 4-particle cumulants are defined as:

$$\begin{aligned} c_n^{a|b}\{2\} &= \langle \text{corr}_n^{a|b}\{2\} \rangle; \\ c_n^{a,a|b,c}\{4\} &= \langle \text{corr}_n^{a,a|b,c}\{4\} \rangle - 2 \langle \text{corr}_n^{a|b}\{2\} \rangle \langle \text{corr}_n^{a|c}\{2\} \rangle \end{aligned} \quad (22)$$

543 Once $c_n^{a,a|b,c}\{4\}$, $c_n^{b,b|c,a}\{4\}$ and $c_n^{c,c|a,b}\{4\}$ are calculated, they will be combined, weighted by the
 544 corresponding event weight, to make the final $c_n^{3-\text{sub}}\{4\}$ in 3-subevent cumulant method. This will triple
 545 the total statistical of 3-subevent method, since all the three configurations are statistically independent.

$$c_n^{3-\text{sub}}\{4\} \equiv \frac{(\sum W^{a,a|b,c}\{4\})c_n^{a,a|b,c}\{4\} + (\sum W^{b,b|c,a}\{4\})c_n^{b,b|c,a}\{4\} + (\sum W^{c,c|a,b}\{4\})c_n^{c,c|a,b}\{4\}}{\sum W^{a,a|b,c}\{4\} + \sum W^{b,b|c,a}\{4\} + \sum W^{c,c|a,b}\{4\}} \quad (23)$$

546 Due to event-by-event multiplicity fluctuation along η , $\sum W^{a,a|b,c}\{4\}$, $\sum W^{b,b|c,a}\{4\}$ and $\sum W^{c,c|a,b}\{4\}$
 547 will not be same with each other. This will cause different statistical significance among $c_n^{a,a|b,c}\{4\}$,
 548 $c_n^{b,b|c,a}\{4\}$ and $c_n^{c,c|a,b}\{4\}$. Due to this reason, the total summation are weighted by the corresponding
 549 total event weight.

550 5.4 Calculation of 2-, 4- and 6-particle flow signal $v_n\{2k\}$

551 Before converting the cumulant to flow signal, in order to increase the statistical significance, the cumu-
 552 lant are re-binned to larger bin width, e.g. from 1% to 10% centrality, weighted by the total number of
 553 events in each event class N_{evt} :

$$c_n^{rebin}\{4\} \equiv \frac{\sum_{i \in \text{event classes}} (N_{evt}^i) c_n^i\{4\}}{N_{evt}^i} \quad (24)$$

554 Different order cumulants provide independent estimates for the same reference harmonic v_n . If the
 555 underlying v_n fluctuation is Bessel-Gaussian or close to Bessel-Gaussian (e.g. power-law function), then
 556 the $2k$ -particle cumulant can be expanded as:

$$\begin{aligned} c_n\{2\} &= \bar{v}_n^2 + 2\delta_n^2 \\ c_n\{4\} &= -\bar{v}_n^4 \\ c_n\{6\} &= \bar{v}_n^6 \end{aligned} \quad (25)$$

557 where \bar{v}_n denotes the mean value of v_n and δ_n describes the Gaussian fluctuation width of v_n . Thus flow
 558 signal $v_n\{2k\}$ for the corresponding cumulant $c_n\{2k\}$ can be defined as:

$$\begin{aligned} v_n\{2\} &= \sqrt{c_n\{2\}} \\ v_n\{4\} &= \sqrt[4]{-c_n\{4\}} \\ v_n\{6\} &= \sqrt[6]{\frac{1}{4}c_n\{6\}} \end{aligned} \quad (26)$$

559 where above equations are universal for standard and subevent cumulant methods.

560 5.5 Calculation of normalized cumulant $nc_n\{2k\}$

561 Multi-particle cumulant not only is affected by the flow fluctuation, but also changes with the mean
 562 value of flow \bar{v}_n . So the centrality and p_T dependence of cumulant partially originated from the centrality
 563 and p_T dependence of \bar{v}_n . In order to disentangle the flow fluctuation from the mean value of flow, an
 564 observable was previously defined to show relative flow fluctuation:

$$\sqrt{\frac{v_n^2\{2\} - v_n^2\{4\}}{v_n^2\{2\} + v_n^2\{4\}}} = \frac{\sigma_v}{\bar{v}} \quad (27)$$

565 where σ_v reflects the fluctuation width of the event-by-event v_n . However, one main defect of this observ-
 566 able is that in order to obtain the R.H.S. of the formula, one has to assume the underlying flow fluctuation
 567 is Gaussian. As will be seen in this analysis, this assumption is not true, especially in peripheral and cen-
 568 tral collision.

569 Instead, a simpler observable is defined that is related to the cumulant ratios [19], and it's notated as
 570 the "normalized cumulant":

$$\begin{aligned} nc_n\{4\} &\equiv \frac{c_n\{4\}}{c_n^2\{2\}} = \left(\frac{v_n\{4\}}{v_n\{2\}}\right)^4 \\ nc_n\{6\} &\equiv \frac{c_n\{6\}}{4c_n^3\{2\}} = \left(\frac{v_n\{6\}}{v_n\{2\}}\right)^6 \end{aligned} \quad (28)$$

571 where a factor of 4 in the definition of $nc_n\{6\}$ is to properly remove the normalization factor in the
 572 definition of $c_n\{6\}$, so that the normalized cumulant falls into the range of $(-1, 1)$. This observable is

573 named as the normalized cumulant since it follows the definition of normalized symmetric cumulant,
 574 where similar normalization terms are applied to the symmetric cumulant. The centrality and p_T depen-
 575 dence of $c_n\{2k\}$ partially originates from those dependence of $\langle v_n^2 \rangle$, so that after normalization, $nc_n\{2k\}$
 576 mainly reflects the fluctuation itself. Another advantage of using normalized cumulant is for the plotting
 577 purpose: there is no longer need to zoom in the Y-axis when the $c_n\{2k\}$ is too small.

578 5.6 Universality check of flow fluctuation models

579 Following the previous discussions, if the flow fluctuation is Gaussian, the 4- and higher even-order
 580 particle cumulants should result in the same flow signal $v_n\{2k\}$. In this section, we will quantify the flow
 581 fluctuation and compare two competing models. [22]

582 For the eccentricity ϵ_n in the initial stage, based on previous theoretical studies [22], there are two
 583 major fluctuation models on the market: Gaussian and power-law. If the eccentricity fluctuation is Gaus-
 584 sian, then the cumulants of eccentricity can be calculated explicitly:

$$\begin{aligned}\epsilon_n\{2\} &= \sqrt{\bar{\epsilon}^2 + \sigma^2} \\ \epsilon_n\{4\} &= \bar{\epsilon} \\ \epsilon_n\{6\} &= \bar{\epsilon}\end{aligned}\tag{29}$$

585 where $\bar{\epsilon}$ is the mean value of the eccentricity and σ^2 is the variance. Similarly, if the eccentricity fluctu-
 586 ation is power-law, then the cumulant of eccentricity can also be calculated explicitly:

$$\begin{aligned}\epsilon_n\{2\} &= \sqrt{\frac{1}{1+\alpha}} \\ \epsilon_n\{4\} &= \sqrt[4]{\frac{2}{(1+\alpha)^2(2+\alpha)}} \\ \epsilon_n\{6\} &= \sqrt[6]{\frac{6}{(1+\alpha)^3(2+\alpha)(3+\alpha)}}\end{aligned}\tag{30}$$

587 where α is the single parameter in the power-law function.

588 In the hydro-dynamical picture, the eccentricity ϵ_n in the initial stage and flow v_n are linearly corre-
 589 lated:

$$v_n\{2k\} = \kappa_n \epsilon_n\{2k\}\tag{31}$$

590 where κ_n is the scaling factor and depends on the harmonic n .

591 In order to derive a universality check for the Gaussian fluctuation, both ϵ and κ_n need to be canceled
 592 out, then we get:

$$\frac{c_n\{6\}}{4(-c_n\{4\})^{\frac{3}{2}}} = 1\tag{32}$$

593 where $c_n\{4\}$ and $c_n\{6\}$ are 4- and 6-particle cumulants respectively. By universality, it means that if the
 594 flow fluctuation is Gaussian, then the quantity on the L.H.S. should be equal to 1. Any derivation from 1
 595 will indicate that the fluctuation is away from Gaussian. Similarly, the universality check for power-law
 596 fluctuation can also be calculated:

$$\frac{c_n\{6\}(2c_n\{2\} - c_n\{4\})}{12c_n\{2\}c_n^2\{4\}} = 1\tag{33}$$

597 where 2-particle cumulant $c_n\{2\}$ is also included. Note that the inclusion of 2-particle cumulant might
 598 introduce non-flow, but for the universality check, we are only focusing central and mid-central colli-
 599 sions, where the non-flow contributions are minimal compared with flow. The results of both checks will
 600 be compared in the measurement section.

5.7 Calculation of symmetric cumulant $sc_{n,m}\{4\}$ and $nsc_{n,m}\{4\}$

5.7.1 Standard symmetric cumulant

The symmetric cumulant measures the correlation and fluctuation between harmonics v_n and v_m ($n < m$).

The 4-particle correlation with mixed harmonics is defined as:

$$corr_{n,m}\{4\} \equiv \left\langle e^{i(n\phi_i+m\phi_j-n\phi_k-m\phi_l)} \right\rangle \quad (34)$$

where n and m denote the order of harmonics v_n and v_m . " $\langle \rangle$ " is the event-by-event mean value weighted by the particle weight. Similarly, we can apply the Q-cumulant technique to calculate $corr_{n,m}\{4\}$ in a single loop [8]:

$$\begin{aligned} corr_{n,m}\{4\} = & (|Q_{n,1}|^2 |Q_{m,1}|^2 - 2\Re(\mathbf{Q}_{n+m,2} \mathbf{Q}_{n,1}^* \mathbf{Q}_{m,1}^*) - 2\Re(\mathbf{Q}_{m-n,2} \mathbf{Q}_{n,1} \mathbf{Q}_{m,1}^*) + |Q_{n+m,2}|^2 \\ & + |Q_{m-n,2}|^2 + 4\Re(\mathbf{Q}_{n,3} \mathbf{Q}_{n,1}^*) + 4\Re(\mathbf{Q}_{m,3} \mathbf{Q}_{m,1}^*) - S_{1,2} |Q_{n,1}|^2 - S_{1,2} |Q_{m,1}|^2 \\ & + S_{2,2} - 6S_{1,4}) / (S_{4,1} + 8S_{1,3} - 6S_{1,2}S_{2,1} + 3S_{2,2} - 6S_{1,4}) \end{aligned} \quad (35)$$

where note that the denominator is same as the denominator of the 4-particle correlation $corr_n\{4\}$.

Then the event-by-event $corr_{n,m}\{4\}$ is averaged within each event class, with the weight $W\{4\}$:

$$W\{4\} \equiv S_{4,1} + 8S_{1,3} - 6S_{1,2}S_{2,1} + 3S_{2,2} - 6S_{1,4} \quad (36)$$

Finally, the symmetric cumulant, $sc_{n,m}\{4\}$, is defined as:

$$sc_{n,m}\{4\} = \langle corr_{n,m}\{4\} \rangle - \langle corr_n\{2\} \rangle \langle corr_m\{2\} \rangle \quad (37)$$

where $corr_n\{2\}$ is simply the 2-particle correlation calculated in the cumulant section.

One caveat of symmetric cumulant is that it not only reflects the correlation between v_n and v_m , but also is scaled by the magnitudes of v_n and v_m . To show the correlation part only, normalized cumulant, $nsc_{n,m}\{4\}$, is defined as:

$$nsc_{n,m}\{4\} = \frac{sc_{n,m}\{4\}}{\langle v_n^2 \rangle \langle v_m^2 \rangle} \quad (38)$$

where by dividing the flow magnitudes of v_n and v_m , only correlation remains in the $nsc_{n,m}\{4\}$. $\langle v_n^2 \rangle$ denotes the mean value of 2-particle v_n , which has been calculated by the previous 2-particle correlation. In order to reduce the non-flow in the estimate of $\langle v_n^2 \rangle$, we will use the calculated 3-subevent $c_n^{b|c}\{2\}$, with an η gap between subevent b and c :

$$\begin{aligned} \langle v_n^2 \rangle &= c_n^{b|c}\{2\} \\ \langle v_m^2 \rangle &= c_m^{b|c}\{2\} \end{aligned} \quad (39)$$

5.7.2 3-subevent symmetric cumulant

Similarly, 4-particle correlation with mixed harmonics can be defined in 3-subevent:

$$corr_{n,m}^{a,a|b,c}\{4\} \equiv \left\langle e^{i(n\phi_i+m\phi_j-n\phi_k-m\phi_l)} \right\rangle \quad (40)$$

where the superscript $a, a|b, c$ represents the subevent that particles i, j, k, l come from:

- particles i and j come from subevent a ;

- particle k comes from subevent b ;

- 624 • particle l comes from subevent c ;

625 There are 12 different unique permutation for $\text{corr}_{n,m}^{a,a|b,c}\{4\}$, where 6 of them have small non-flow
626 since two particles that come from the same subevent have the same sign in $n\phi_i + m\phi_j - n\phi_k - m\phi_l$. In
627 this analysis, we will calculate the following 6 configurations then combine them on the cumulant level:

628 • $\text{corr}_{n,m}^{a,a|b,c}\{4\}$

629 • $\text{corr}_{n,m}^{a,a|c,b}\{4\}$

630 • $\text{corr}_{n,m}^{b,b|c,a}\{4\}$

631 • $\text{corr}_{n,m}^{b,b|a,c}\{4\}$

632 • $\text{corr}_{n,m}^{c,c|a,b}\{4\}$

633 • $\text{corr}_{n,m}^{c,c|b,a}\{4\}$

634 and for simplicity, we will only list the formula for the first case. The formula for other cases can be
635 derived easily by permutations.

636 After applying the Q-cumulant technique, $\text{corr}_{n,m}^{a,a|b,c}\{4\}$ can be calculated in a single loop:

$$\text{corr}_{n,m}^{a,a|b,c}\{4\} = \frac{\mathcal{R}e(\mathbf{Q}_{n,1}^a \mathbf{Q}_{m,1}^a \mathbf{Q}_{n,1}^{b*} \mathbf{Q}_{m,1}^{c*}) - \mathcal{R}e(\mathbf{Q}_{n+m,2}^a \mathbf{Q}_{n,1}^{b*} \mathbf{Q}_{m,1}^{c*})}{(S_{2,1}^a - S_{1,2}^a) S_{1,1}^b S_{1,1}^c} \quad (41)$$

637 where all the variables are defined previously.

638 The symmetric cumulant using 3-subevent method, $sc_{n,m}^{3-\text{sub}}\{4\}$, is defined as:

$$sc_{n,m}^{3-\text{sub}}\{4\} = \left\langle \text{corr}_{n,m}^{a,a|b,c}\{4\} \right\rangle - \left\langle \text{corr}_n^{a|b}\{2\} \right\rangle \left\langle \text{corr}_m^{a|c}\{2\} \right\rangle \quad (42)$$

639 where $\text{corr}_n^{a|b}\{2\}$ is the 2-particle correlation calculated in the 3-subevent cumulant section.

640 Similarly, the normalized symmetric cumulant using 3-subevent method, $nsc_{n,m}^{3-\text{sub}}\{4\}$, is defined as:

$$nsc_{n,m}^{3-\text{sub}}\{4\} = \frac{sc_{n,m}^{3-\text{sub}}\{4\}}{\langle v_n^2 \rangle \langle v_m^2 \rangle} \quad (43)$$

641 where the denominator is calculated in the same way as normalized symmetric cumulant with standard
642 method. Note that $\langle v_n^2 \rangle$ are not calculated in adjacent subevents as $\text{corr}_n^{a|b}\{4\}$, otherwise non-flow will
643 contribute to the normalization factors.

644 5.8 Calculation of asymmetric cumulant $ac_{n,n+m}\{3\}$ and $nac_{n,n+m}\{3\}$

645 5.8.1 Standard asymmetric cumulant

646 Symmetric cumulant measures the correlation between flow harmonics v_n and v_m , to further evaluate the
647 correlation among more harmonics v_n , v_m and v_{n+m} , the asymmetric cumulant is proposed. 3-particle
648 correlation with mixed harmonics is defined as:

$$\text{corr}_{n,m,n+m}\{3\} \equiv \left\langle e^{i(n\phi_i + m\phi_j - (n+m)\phi_k)} \right\rangle \quad (44)$$

649 where note that the coefficient of the third particle k need to be $n + m$ otherwise the mean value is 0. One
650 advantage of asymmetric cumulant is that it only requires 3-particle correlation, which results in much
651 better statistics than symmetric cumulant.

652 To calculate the 3-particle correlation in a single loop, formula with Q-cumulant technique is derived
653 as [8]:

$$\begin{aligned} corr_{n,m,n+m}\{3\} &= (\mathcal{R}e(\mathbf{Q}_{n,1}\mathbf{Q}_{m,1}\mathbf{Q}_{n+m,1}^*) - \mathcal{R}e(\mathbf{Q}_{n+m,1}\mathbf{Q}_{n+m,2}^*) - \mathcal{R}e(\mathbf{Q}_{n,1}\mathbf{Q}_{n,2}^*) \\ &\quad - \mathcal{R}e(\mathbf{Q}_{m,1}\mathbf{Q}_{m,2}^*) + 2S_{1,3}) / (S_{3,1} - 3S_{1,2}S_{1,1} + 2S_{1,3}) \end{aligned} \quad (45)$$

654 where all the variables are same as those in the cumulant section.

655 The event-by-event $corr_{n,m,n+m}\{3\}$ is then averaged within each event class, with the event weight
656 $W\{3\}$:

$$W\{3\} = S_{3,1} - 3S_{1,2}S_{1,1} + 2S_{1,3} \quad (46)$$

657 Finally, the asymmetric cumulant, $ac_{n,n+m}\{3\}$, is calculated:

$$ac_{n,n+m}\{3\} = \langle corr_{n,m,n+m}\{3\} \rangle \quad (47)$$

658 where unlike cumulant or symmetric cumulant, the asymmetric cumulant is simply the average of 3-
659 particle correlation with mixed harmonics. Like symmetric cumulant, in order to measure the pure
660 correlation among v_n , v_m and v_{n+m} , normalized asymmetric cumulant, $nac_{n,n+m}\{3\}$, is defined as:

$$nac_{n,n+m}\{3\} = \frac{ac_{n,n+m}\{3\}}{\sqrt{\langle v_n^2 v_m^2 \rangle \langle v_{n+m}^2 \rangle}} \quad (48)$$

661 where v_n^2 denotes the 2-particle v_n . In the case where $n = m$:

$$\langle v_n^2 v_m^2 \rangle = \langle v_n^4 \rangle \quad (49)$$

662 where $\langle v_n^4 \rangle$ is related to the 4-particle cumulant, after non-flow is suppression. Using 3-subevent method:
663

$$\langle v_n^4 \rangle = c_n^{3-sub}\{4\} + 2(c_n^{3-sub}\{2\})^2 \quad (50)$$

664 In this analysis, since only $nac_{2,4}\{3\}$ is measured, there is no need to evaluate $\langle v_n^2 v_m^2 \rangle$ separately: it can
665 be calculated by reusing 3-subevent 2- and 4-particle cumulant results.

666 5.8.2 3-subevent asymmetric cumulant

667 In a similar way, 3-particle with mixed harmonics, using 3-subevent method, is defined as:

$$corr_{n,m,n+m}^{a,b|c}\{3\} \equiv \left\langle e^{i(n\phi_i+m\phi_j-(n+m)\phi_k)} \right\rangle \quad (51)$$

668 where the superscript $a, b|c$ represents the subevent that particles i, j, k come from:

- 669 • particle i comes from subevent a ;
- 670 • particle k comes from subevent b ;
- 671 • particle l comes from subevent c ;

672 There are 6 different unique permutation for $corr_{n,m}^{a,b|c}\{3\}$, which reduced to 3 unique cases in the
673 case $n = m$. In this analysis, we will calculate the following 3 configurations then combine them on the
674 cumulnat level:

- 675 • $corr_{n,n,2n}^{a,b|c}\{3\}$

676 • $\text{corr}_{n,n,2n}^{b,c|a}\{3\}$

677 • $\text{corr}_{n,n,2n}^{c,a|b}\{3\}$

678 and for simplicity, we will only list the formula for the first case. The formula for other cases can be
679 derived easily by permutations.

680 After applying the Q-cumulant technique, event-by-event $\text{corr}_{n,m,n+m}^{a,b|c}$ can be calculated in a single
681 loop:

$$\text{corr}_{n,m,n+m}^{a,b|c}\{3\} = \frac{\mathcal{Re}(\mathbf{Q}_{n,1}^a \mathbf{Q}_{m,1}^b \mathbf{Q}_{n+m,1}^{c*})}{S_{1,1}^a S_{1,1}^b S_{1,1}^c} \quad (52)$$

682 where all the variables are defined previously.

683 The asymmetric cumulant using 3-subevent method, $ac_{n,n+m}^{3-\text{sub}}\{3\}$, is defined as:

$$ac_{n,n+m}^{3-\text{sub}}\{3\} = \langle \text{corr}_{n,m,n+m}^{a,b|c}\{3\} \rangle \quad (53)$$

684 Similarly, the normalized asymmetric cumulant using 3-subevent method, $nac_{n,n+m}^{3-\text{sub}}\{3\}$, is defined as:
685

$$nac_{n,n+m}^{3-\text{sub}}\{3\} = \frac{ac_{n,n+m}^{3-\text{sub}}\{3\}}{\sqrt{\langle v_n^2 v_m^2 \rangle \langle v_{n+m}^2 \rangle}} \quad (54)$$

686 where the denominator is calculated in the same way as normalized asymmetric cumulant using standard
687 method.

6 Analysis

6.1 Particle phase space

In the cumulant analysis, measurements are repeated with particles coming from different phase space (η, ϕ). There are four different p_T ranges:

- $0.5 < p_T < 5.0 \text{ GeV}$;
- $1.0 < p_T < 5.0 \text{ GeV}$;
- $1.5 < p_T < 5.0 \text{ GeV}$;
- $2.0 < p_T < 5.0 \text{ GeV}$;

While calculating the $2k$ -particle correlations, all the $2k$ particles will come from the same p_T window. Note it is different from traditional differential cumulant measurements, where only one out of $2k$ particles comes from the assigned p_T range. The traditional differential cumulant measurement assumes that the flow in different p_T ranges share the same event plane, however, measurement of flow decorrelation in p_T shows that such assumption is ungrounded. In this analysis, all the particles are coming from the same p_T range, which also simplifies the differential cumulant formula, without special treatment of reference particles.

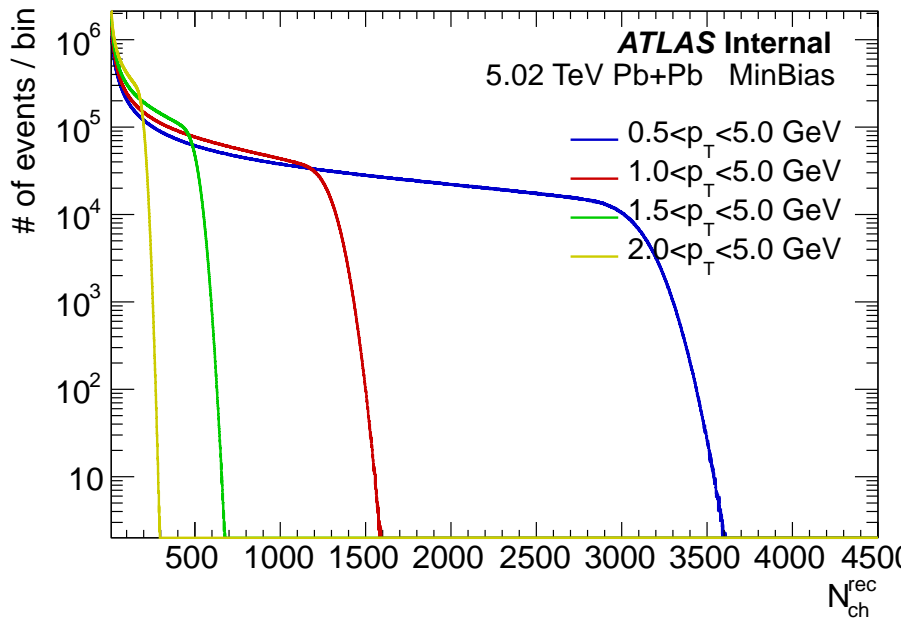


Figure 12: Distribution of reconstructed tracks from different p_T ranges.

To get an idea of how many particles are included with different p_T cuts, Fig. 12 shows the distributions of reconstructed tracks N_{ch}^{rec} from different p_T ranges. For $0.5 < p_T < 5.0 \text{ GeV}$, the N_{ch}^{rec} extends to 3600, while for the highest p_T cut $2.0 < p_T < 5.0 \text{ GeV}$, the largest N_{ch}^{rec} is less than 300. This means that the statistical errors for the highest p_T cut will be quite large.

In the standard cumulant method, all the particles have $-2.5 < \eta < 2.5$, while in the subevent method, the subevent is defined based on η :

- Subevent a : particles from $-2.5/3 < \eta < 2.5/3$;

- 710 • Subevent *b*: particles from $-2.5 < \eta < -2.5/3$;
 711 • Subevent *c*: particles from $2.5/3 < \eta < 2.5$;

712 where additional η gaps can be applied between subevent *a* and *b*(*c*) to further suppress the long-range
 713 non-flow correlations.

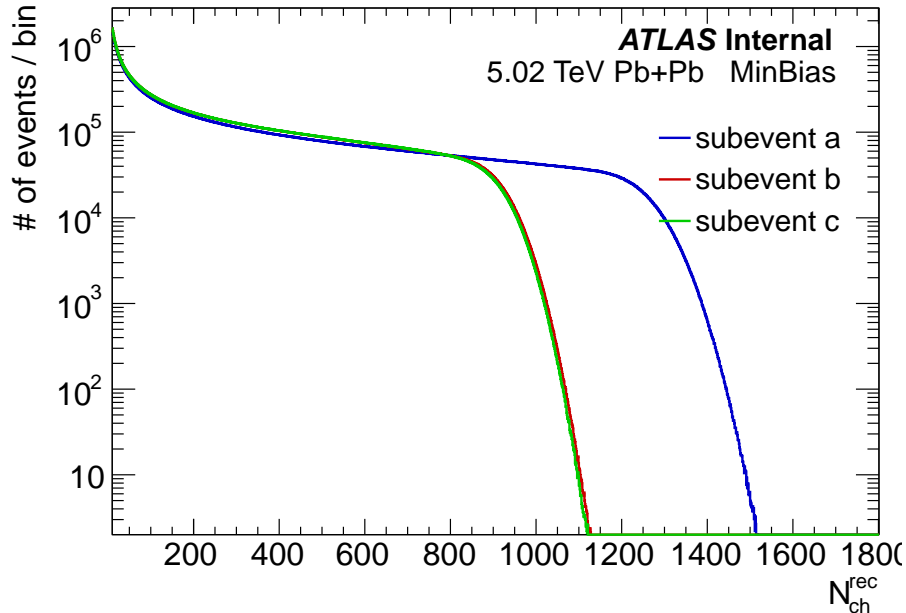


Figure 13: Distribution of reconstructed tracks from different η ranges (subevents).

714 Fig. 13 shows the distribution of reconstructed tracks from different η ranges, which are defined as
 715 subevent *a*, *b* and *c*. N_{ch}^{rec} is largest in subevent *a* with $-2.5/3 < \eta < 2.5/3$, mainly due to two reasons:
 716 truth N_{ch} slightly decreases as $|\eta|$ grows and the tracking efficiency also decrease at large $|\eta|$. Meanwhile,
 717 N_{ch}^{rec} from subevent *b* and *c* are slightly different, which originates from the facts that: 1) mean of z
 718 position of primary vertex is slightly shifted to the negative side, 2) tracking efficiency is not symmetric
 719 between positive and negative η .

720 6.2 Trigger weighting

721 Events in this analysis are collected by two minimum bias triggers and multiple UCC triggers. The
 722 statistics of collected events are shown in the left panel of Fig. 14, where the UCC triggers greatly
 723 enhanced the statistics in the region of FCal $E_T > 4.2$ TeV. However, such enhancement will introduce
 724 potential bias when calculating cumulants in the event class defined by N_{ch}^{rec} .

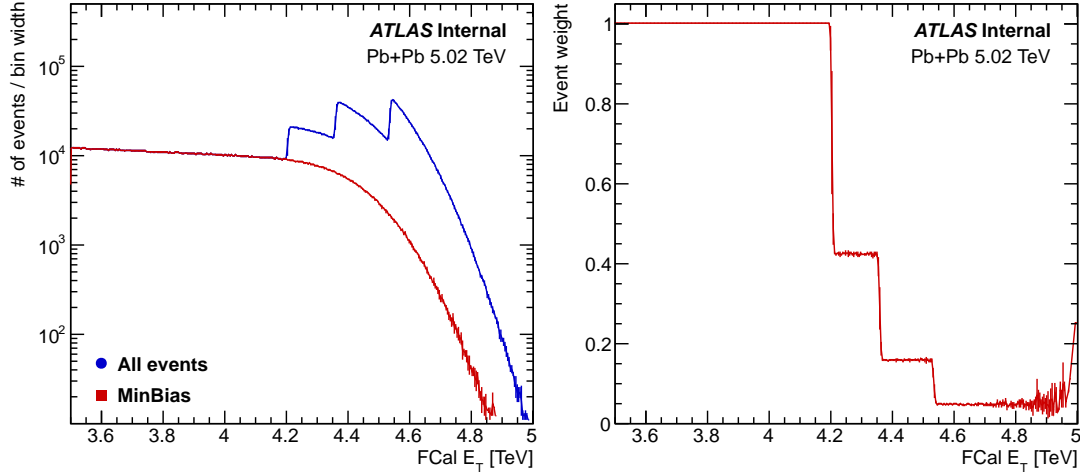


Figure 14: Additional event weights applied in order to properly include the UCC events.

To properly include the events that passed UCC trigger, an event weight w_{trig} has been applied to the $\langle \text{corr}_n\{2k\} \rangle$ calculation:

$$w_{trig} \equiv \frac{\text{events passed MinBias}}{\text{event passed MinBias and UCC}} \quad (55)$$

where w_{trig} is only estimated as a function of FCal E_T , as shown in the right panel of Fig. 14. w_{trig} equals 1 for minimum-bias events and it lowers to three steps as FCal E_T increases.

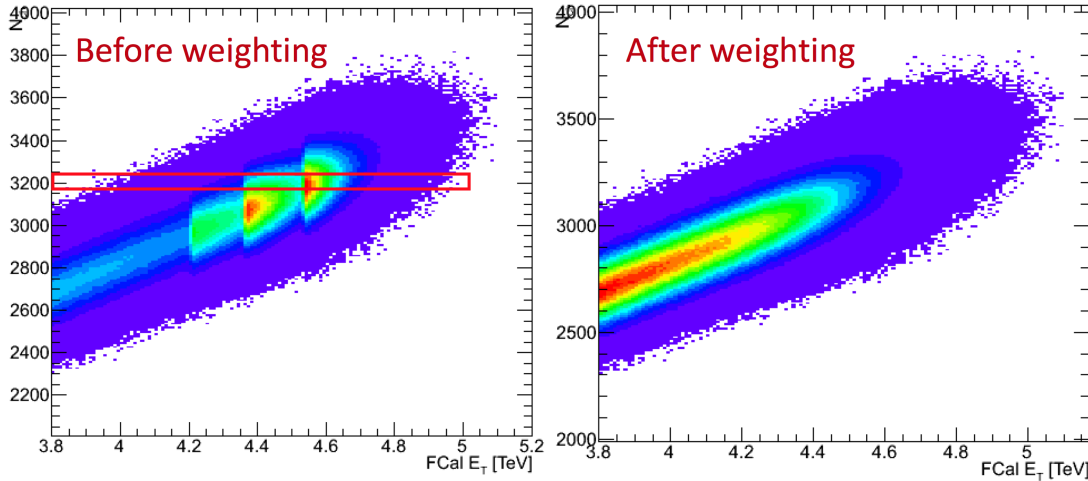


Figure 15: Correlation between FCal sum E_T and reconstructed tracks N_{ch}^{rec} , before (left) and after (right) applying the UCC trigger weights.

As one demonstration of how this event weight works, the correlation between FCal E_T and number of reconstructed tracks N_{ch}^{rec} is shown in Fig. 15. Before w_{trig} is applied, enhancement of statistics is observed in the large FCal E_T region, while after applying w_{trig} , the minimum-bias + UCC distribution behaves just like the minimum-bias events as expected.

733 6.3 Flattening procedure

734 In heavy ion collisions, since the event plane angle fluctuates randomly event-by-event, the particle
 735 ϕ angle distribution averaged over many events should be flat, and the discrepancy is denoted as the
 736 detector effects. From the Monte-Carlo sample, tracking efficiency and fakes can be estimated as a
 737 function of η and p_T , but the residual detector effects in the ϕ plane needs further correction, and the
 738 procedure is named as "flattening".

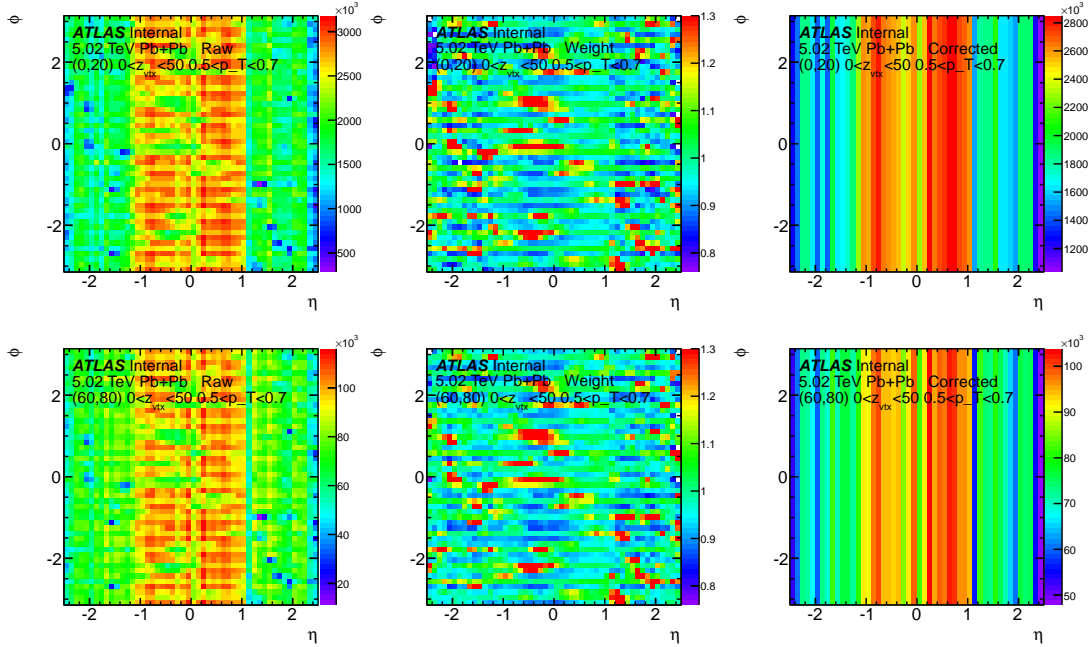


Figure 16: Demonstration of flattening procedure in different centralities: top row is 0 – 20% and bottom row is 60 – 80%. Left column are the raw (η, ϕ) distributions, middle column are the estimated correction factor w_ϕ , right column are the corrected (η, ϕ) distributions.

739 Left column of Fig. 16 shows the raw (η, ϕ) distribution without any correction, and several "holes"
 740 are clearly observed in the transverse plane. In order to correct this detector effect, the correction factor
 741 w_ϕ is defined as:

$$w_\phi(\eta, \phi) \equiv \frac{\langle N(\delta\eta) \rangle}{N(\delta\eta, \delta\phi)} \quad (56)$$

742 where $N(\delta\eta, \delta\phi)$ is the number of particles in the small (η, ϕ) phase-space window; and $\langle N(\delta\eta) \rangle$ is the
 743 mean number of particles in the small η window averaged over the whole ϕ range. The middle panel gives
 744 an example of the $w_\phi(\eta, \phi)$: for the "holes" in raw (η, ϕ) distributions, w_ϕ is larger than 1. Right column
 745 shows the (η, ϕ) distribution after the correction, and as expected, for each narrow η slice, the corrected
 746 ϕ distribution is uniform. This correction w_ϕ will be applied as the particle weight when calculating the
 747 $\langle \text{corr}_n\{2k\} \rangle$.

748 Since the detector effect depends on the occupancy of the detector, w_ϕ is evaluated in different cen-
 749 trality ranges. Fig. 16 shows a comparison between centrality 0 – 20% and 60 – 80%. The correction
 750 factors are not identical, but very similar between the two centralities.

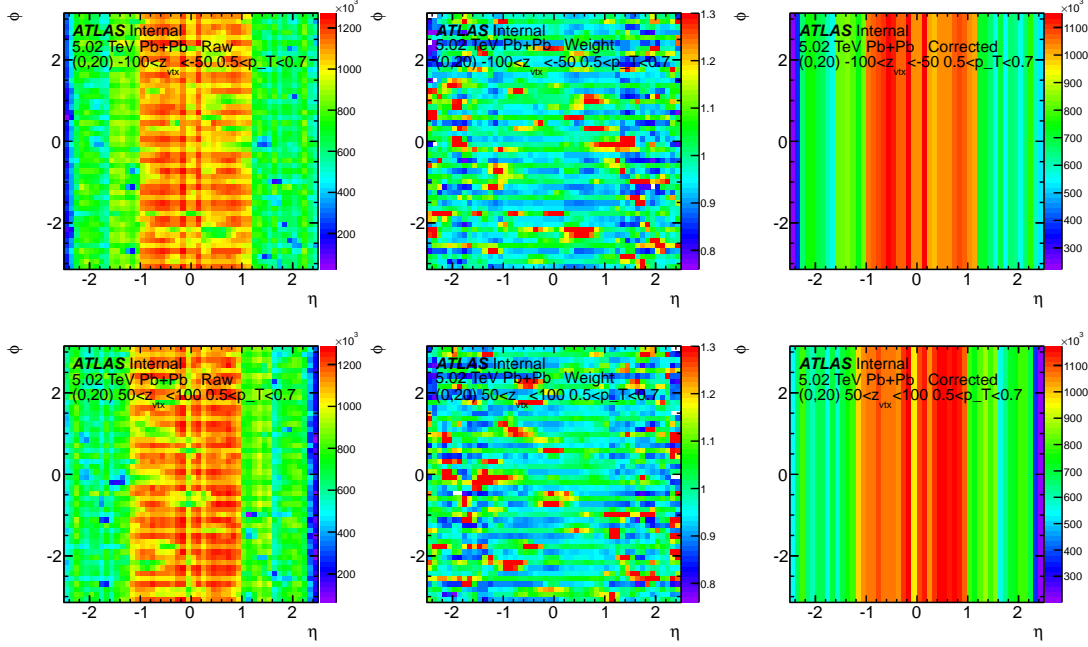


Figure 17: Demonstration of flattening procedure in different z_{vtx} ranges: top row is from $-100 \text{ mm} < z_{\text{vtx}} < -50 \text{ mm}$ and bottom row is from $50 \text{ mm} < z_{\text{vtx}} < 100 \text{ mm}$. Left column are the raw (η, ϕ) distributions, middle column are the estimated correction factor w_ϕ , right column are the corrected (η, ϕ) distributions.

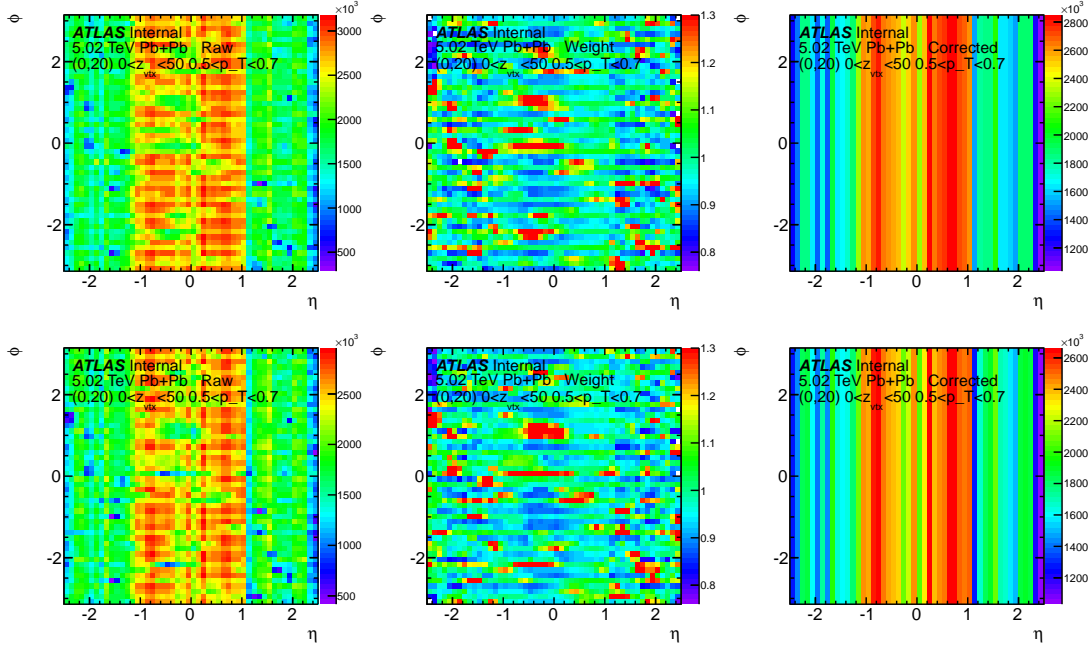


Figure 18: Demonstration of flattening procedure with particles of different charges: top row is for negative-charged particles and bottom row is for positive-charged particles. Left column are the raw (η, ϕ) distributions, middle column are the estimated correction factor w_ϕ , right column are the corrected (η, ϕ) distributions.

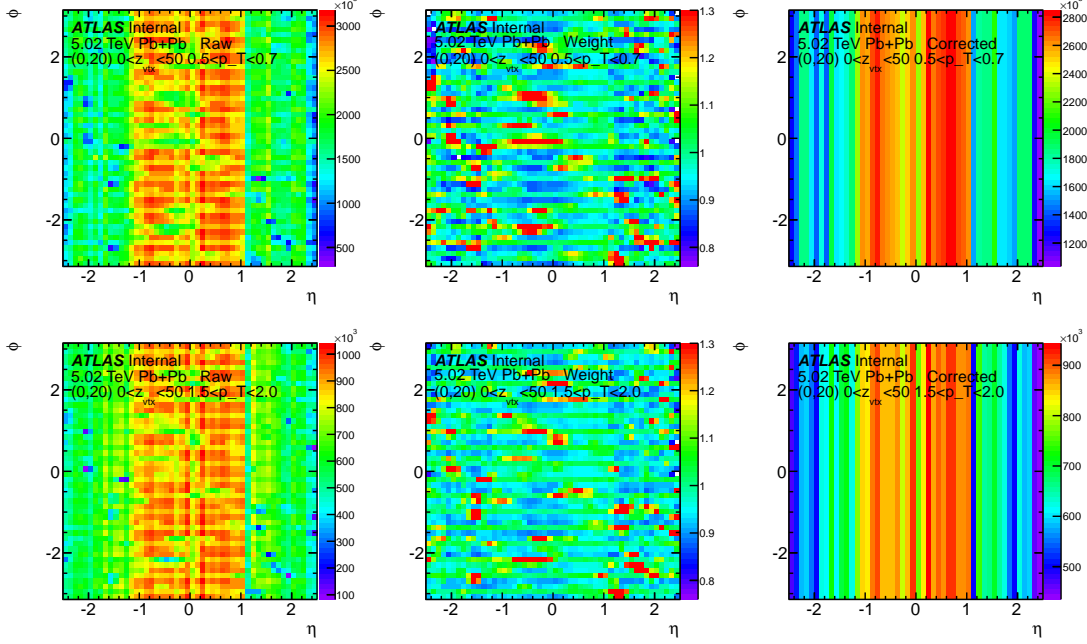


Figure 19: Demonstration of flattening procedure with particles from different p_T ranges: top row has $0.5 < p_T < 0.7$ GeV and bottom row has $1.5 < p_T < 2.0$ GeV. Left column are the raw (η, ϕ) distributions, middle column are the estimated correction factor w_ϕ , right column are the corrected (η, ϕ) distributions.

In additional, the fluctuation of z position of the primary vertex will cause the N_{ch} distribution to shift in η . To compensate this effect, w_ϕ is also estimated in different z_{vtx} ranges. Fig. 17 shows a comparison between $-150 \text{ mm} < z_{vtx} < -100 \text{ mm}$ and $100 \text{ mm} < z_{vtx} < 150 \text{ mm}$. From the left column, it is clear that the η distributions are shifted together with z_{vtx} position, which means that a z_{vtx} -dependent w_ϕ correction is needed.

Furthermore, the w_ϕ corrections are also evaluated for negative- and positive-charged particles separately, as shown in Fig. 18. From the raw distribution, differences have already been observed: there are slightly more holes for positive particles than negative ones.

In the end, Fig. 19 shows the comparison of w_ϕ estimated from particles in two different p_T ranges: $0.3 < p_T < 0.5$ GeV and $1.5 < p_T < 2.0$ GeV. As a results, particles with higher p_T are more uniformly distributed, which is consistent with the fact that tracking efficiency increases towards higher p_T .

6.4 Event class

Event-by-event multi-particle correlation $corr_n\{2k\}$ is averaged within bunch of similar events, which are denoted as event class. Since cumulant measures the flow fluctuation in certain event class, how event class is defined will have an effect on the cumulant magnitude. In previous ATLAS paper on cumulant in small systems, we have shown that even the sign of cumulant can change if the event class definition is changed. In this section, we will discuss the definition of event class in this analysis and its potential impact on the cumulant results.

Since flow in the final stage is strongly correlated with the eccentricity from the initial stage, an optimal quantity to model the eccentricity changing would be centrality, which reflects the overlapping region of the two nucleus. In heavy ion collision, since centrality is not a direct-measurable quantity, total transverse energy E_T in the FCal detector is used as an indicator for centrality, which means the centrality percentile is calculated based on the FCal E_T distribution (see the Dataset section for details). In this analysis, the default event class will be defined by centrality.

775 The following question is how large the event class bin width should be. In principle, narrower bin
 776 width is always preferred, since wider bin width will include events from different centralities, which can
 777 result in different flow fluctuation. However, there will be not enough events to calculate the higher order
 778 cumulants if the bin width is too narrow. In practice we choose 1% centrality percentile as the default
 779 event class bin width.

780 To show that 1% bin width will not introduce any bias to the measurement, we have also tested the
 781 following bin widths:

- 782 • Event class bin width: 2%;
- 783 • Event class bin width: 5%;
- 784 • Event class bin width: 10%;

785 and the results will be discussed in the systematic section.

786 As discussed in the methodology section, even though the event class bin width is only 1% centrality,
 787 neighbouring bins will be merged together at the cumulant level to increase the statistics. Note that since
 788 the re-bin is performed on the cumulant, it does not change the underlying flow fluctuation.

789 The event class definition is specially treated in the ultra-central collision, simply because 1% cen-
 790 trality bin width is not narrow enough to constrain the fluctuation of flow. Instead, the following event
 791 class criteria are used:

- 792 • Event class defined by FCal E_T , with bin width = 6 GeV;
- 793 • Event class defined by number of reconstructed tracks N_{ch}^{rec} , with p_T range always $0.5 < p_T < 5.0$
 794 GeV, no matter the p_T range for the cumulant calculation. The bin width is 5 track;

795 where the purpose of the second criteria is to evaluate the flow fluctuation by changing the centrality
 796 definition, which will be discussed in the results section.

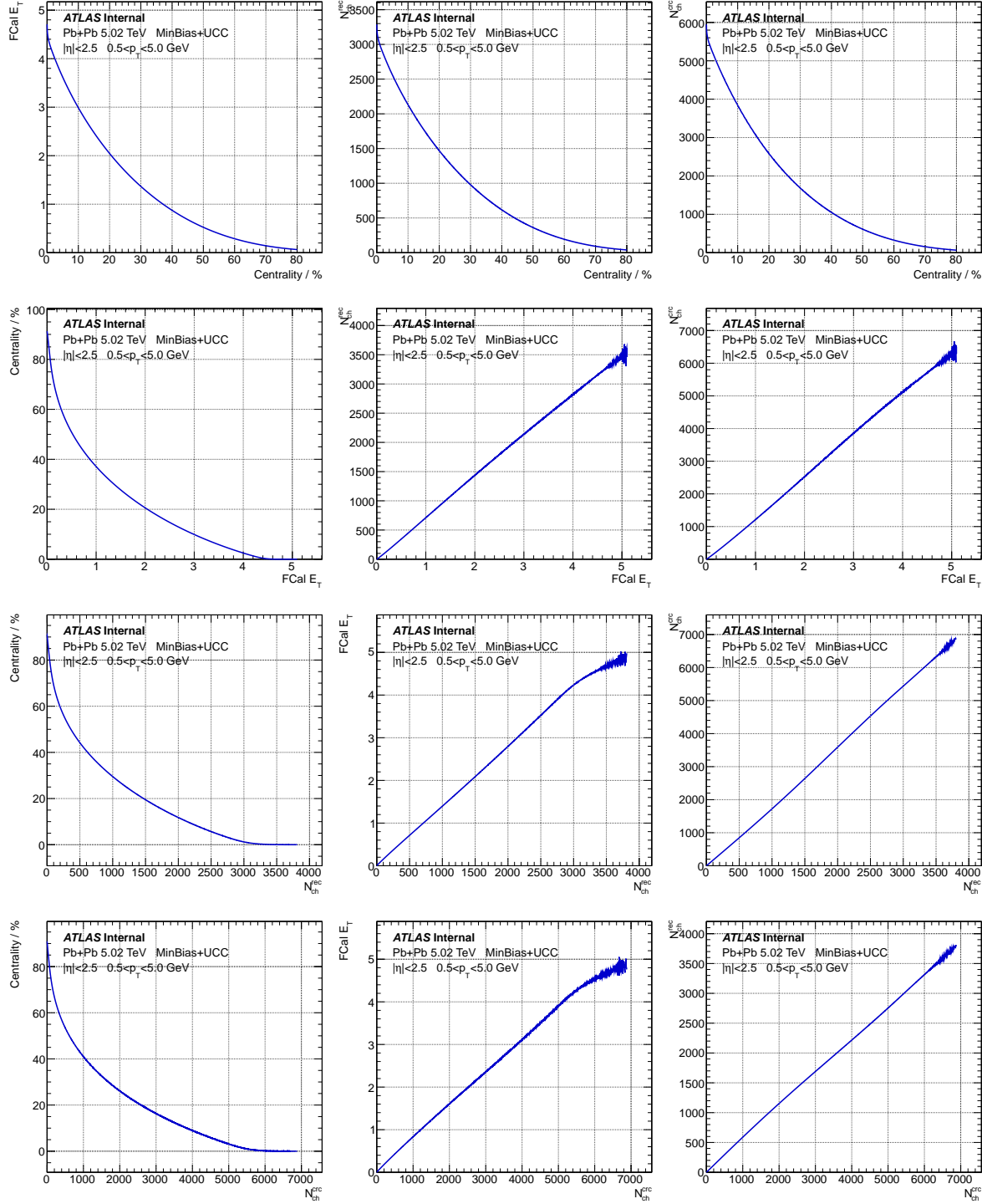


Figure 20: Conversion maps among centrality, FCal E_T , reconstructed tracks N_{ch}^{rec} and tracking efficiency corrected reconstructed tracks N_{ch}^{crc} . The Y-axis shows the mean value calculated in the event class defined by X-axis.

797 The conversion maps among centrality, FCal E_T , number of reconstructed tracks N_{ch}^{rec} and number
 798 of corrected reconstructed tracks N_{ch}^{crc} are listed in Fig. 20, where the Y-axis indicates the mean value
 799 calculated in the event class defined by the X-axis. When necessary, these maps are used to convert

800 results with different event class definitions into the same X-axis.

801 6.5 Mixed events

802 To correct the detector effects, we weighted the tracks by the tracking efficiency and fraction of fake
 803 tracks obtained from Monte-Carlo plus the detector simulation. In additional, w_ϕ obtained from flattening
 804 procedure is applied as the event weight to further suppress the detector effects in the transverse plane.
 805 To estimate the residual detector effects, a mixed event technique can be implemented. In this section,
 806 we will discuss why mixed event work and how to implement it.

807 Compared with the physics signal, the major feature of detector effect is that it does not fluctuate
 808 from event to event. In other words, detector effects are correlated across "similar" events that are
 809 neighbouring in time. By "similar", it requires those events have the similar centrality and z position of
 810 primary vertex z_{vtx} . On the other hand, the physics signal, like flow, are correlated within a single event,
 811 but uncorrelated between different events. Using these features, the mixed event can be reconstructed by
 812 measuring the correlation among different events.

813 In the following we will take the calculation of $c_n\{4\}$ as one example to show how to calculate the
 814 corresponding mixed events. The definition of 2- and 4-particle correlation in mixed events is written as:

815

$$\begin{aligned} corr_n^{bk}\{2\} &\equiv \langle e^{in(\phi_i - \phi_j)} \rangle \\ corr_n^{bk}\{4\} &\equiv \langle e^{in(\phi_i + \phi_j - \phi_k - \phi_l)} \rangle \end{aligned} \quad (57)$$

816 where bk in the superscript is used to separate the mixed event (background) from the original signal
 817 (foreground). The definition seems to be identical to the $corr_n\{2k\}$ in a single event, however, now i, j, k
 818 and l are particles coming from 4 different events that are neighbouring in time. Note that there are 3
 819 equivalent permutation of i, j, k and l : $(\phi_i + \phi_j - \phi_k - \phi_l)$, $(\phi_i + \phi_k - \phi_j - \phi_l)$ and $(\phi_i + \phi_l - \phi_j - \phi_k)$ and
 820 they should all be included when calculating the background.

821 In the definition of $corr_n^{bk}\{2\}$ and $corr_n^{bk}\{4\}$, since particle can never be correlated with itself, all
 822 duplicates are gone. Thus the Q-cumulant formula are much simpler compared with the calculation of
 823 foreground:

$$\begin{aligned} corr_n^{bk}\{2\} &= \frac{\text{Re}(\mathbf{Q}_{n,1}^i \mathbf{Q}_{n,1}^{j*})}{S_{1,1}^i S_{1,1}^j} \\ corr_n^{bk}\{4\} &= \frac{\text{Re}(\mathbf{Q}_{n,1}^i \mathbf{Q}_{n,1}^j \mathbf{Q}_{n,1}^{k*} \mathbf{Q}_{n,1}^{l*})}{S_{1,1}^i S_{1,1}^j S_{1,1}^k S_{1,1}^l} \end{aligned} \quad (58)$$

824 where i, j, k and l denotes 4 different events.

825 Then followed the same procedure, the $corr_n^{bk}\{2k\}$ are averaged in each event class to get $\langle corr_n^{bk}\{2k\} \rangle$.
 826 The 4-particle cumulant from background can also be defined in the same way:

$$c_n^{bk}\{4\} = \langle corr_n^{bk}\{4\} \rangle - 2 \langle corr_n^{bk}\{2\} \rangle^2 \quad (59)$$

827 where the event class is defined by the first event i in the mixed events.

828 In the end, we subtract the cumulant calculated in mixed events from the foreground, to obtain the
 829 corrected cumulant:

$$c_n^{crt}\{4\} \equiv c_n\{4\} - c_n^{bk}\{4\} \quad (60)$$

830 In the measurement section, without special mention, All cumulant results are using $c_n^{crt}\{2k\}$ as the
 831 default.

6.6 Statistical uncertainty

Cumulant analysis, especially for higher order cumulant, suffers from statistics, which makes it crucial to correctly calculate the statistical uncertainty. The errors can be directly calculated from the cumulant definition, by using appropriate error propagation. Take 4-particle standard cumulant as an example:

$$c_n\{4\} = \langle \text{corr}_n\{4\} \rangle - 2 \langle \text{corr}_n\{2\} \rangle^2 \quad (61)$$

where both $\langle \text{corr}_n\{4\} \rangle$ and $\langle \text{corr}_n\{2\} \rangle$ are averaged over many events, so the errors are calculated as:

$$\begin{aligned} \delta^2(\langle \text{corr}_n\{4\} \rangle) &\equiv \frac{\sum_i W^i\{4\} (\text{corr}_n^i\{4\} - \langle \text{corr}_n\{4\} \rangle)^2}{\sum_i W^i\{4\}} \\ \delta^2(\langle \text{corr}_n\{2\} \rangle) &\equiv \frac{\sum_i W^i\{2\} (\text{corr}_n^i\{2\} - \langle \text{corr}_n\{2\} \rangle)^2}{\sum_i W^i\{2\}} \end{aligned} \quad (62)$$

However, since the weights $W^i\{4\}$ and $W^i\{2\}$ are not random, there is a correction factor to yield an unbiased estimator:

$$\begin{aligned} \delta^2(\langle \text{corr}_n\{4\} \rangle) &= (1 - \frac{\sum_i (W^i\{4\})^2}{(\sum_i W^i\{4\})^2}) \delta_{\text{real}}^2(\langle \text{corr}_n\{4\} \rangle) \\ \delta^2(\langle \text{corr}_n\{2\} \rangle) &= (1 - \frac{\sum_i (W^i\{2\})^2}{(\sum_i W^i\{2\})^2}) \delta_{\text{real}}^2(\langle \text{corr}_n\{2\} \rangle) \end{aligned} \quad (63)$$

where δ_{real} means the correct, unbiased statistical error estimator.

Note that both $\langle \text{corr}_n\{4\} \rangle$ and $\langle \text{corr}_n\{2\} \rangle$ measure the flow sign, so they are not independent variables. Thus the covariance needs to be considered while calculating the statistical errors for $c_n\{4\}$:

$$\delta^2(c_n\{4\}) = \delta_{\text{real}}^2(\langle \text{corr}_n\{4\} \rangle) + (4 \langle \text{corr}_n\{2\} \rangle)^2 \delta_{\text{real}}^2(\langle \text{corr}_n\{4\} \rangle) - 8 \langle \text{corr}_n\{2\} \rangle \text{cov}(\langle \text{corr}_n\{4\} \rangle, \langle \text{corr}_n\{2\} \rangle) \quad (64)$$

where the covariance between $\langle \text{corr}_n\{4\} \rangle$ and $\langle \text{corr}_n\{2\} \rangle$ is denoted as $\text{cov}(\langle \text{corr}_n\{4\} \rangle, \langle \text{corr}_n\{2\} \rangle)$.

As can be seen, it is quite cumbersome to calculate statistical error in this way: many histograms need to be saved in order to calculate the covariance. Furthermore, the formula are more complicated in subevent methods: up to 10 covariances will show up in the formula! Due to this reason, in this analysis, sub-sample technique is used to determine the statistical errors.

The sub-sample technique is a data-driven way to calculate the statistical errors, which is much easier to implement in the code. The first step is to randomly divide the whole data set into N sub-samples ($N = 20$ in this analysis). To guarantee that each sub-sample are not biased by run configuration like trigger setup and detector effects, in practice, we used random seeds to determine which sub-sample each event will fall into, which guarantees the dividing procedure to be random.

To demonstrate the random seed works, we have tested this produce on the 2015+2016 13 TeV low- μ pp sample. The reason of choosing pp is because the runs are throughout two years and run conditions as well as trigger setups are very different. The results are presented in Fig. 21. Left plot shows the N_{ch} distribution for the whole sample, where several "bumps" are from the high-multiplicity track (HMT) triggers. Right plot shows the relative difference of the statistics between sub-samples (indicated by different colors) and the mean (5% statistics of the whole sample), as a function of N_{ch} . As can be seen, the relative difference is within 1% in the region where statistics are good. This demonstrates the dividing procedure produces randomly divided sub-samples.

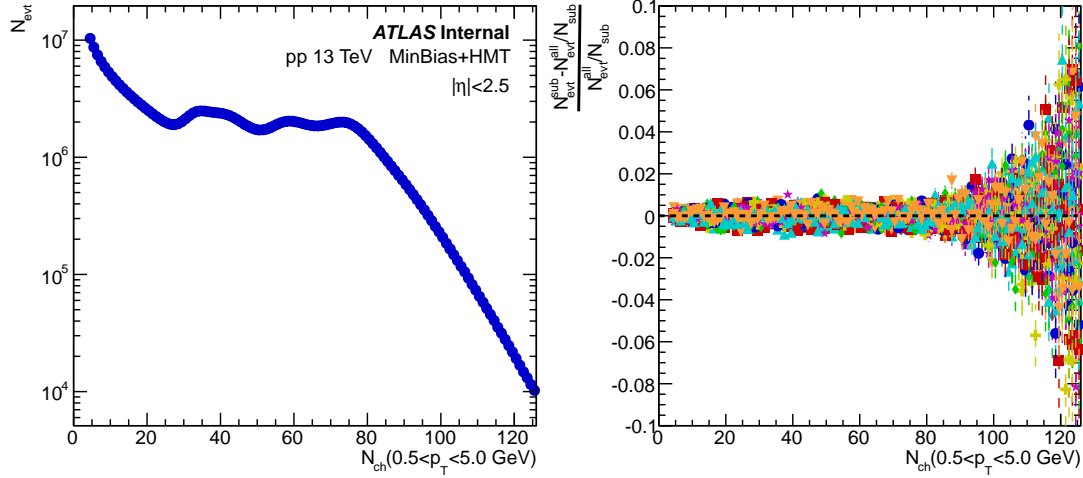


Figure 21: N_{ch} distribution for the whole 13 TeV pp data sample (left); Right plot shows the relative difference of the statistics between sub-samples (indicated by different markers and colors) and the mean (5% statistics of the whole sample). The results are shown as a function of N_{ch} .

860 Then the $2k$ -particle cumulant are calculated in whole sample, as well as in each sub-sample respec-
 861 tively. The standard deviation of cumulants calculated from all sub-samples are quoted as the statistical
 862 uncertainty of the cumulant for the whole sample.

863 7 Systematics and cross-checks

864 7.1 Outline

865 The systematics and cross-checks are presented in this section, with relative errors δ calculated in the
 866 following two scenarios:

- 867 • if one check is to compare with default: $\delta \equiv \frac{\mathcal{O}_{\text{check}} - \mathcal{O}_{\text{default}}}{\mathcal{O}_{\text{default}}}$;
- 868 • if two checks (from sub-samples) are compared with each other: $\delta \equiv \frac{\mathcal{O}_{\text{check 1}} - \mathcal{O}_{\text{check 2}}}{\mathcal{O}_{\text{check 1}} + \mathcal{O}_{\text{check 2}}}$;

869 where \mathcal{O} denotes the observable: 2-, 4- or 6-particle cumulant, and subscripts "default" and "check" are
 870 used to distinguish the different criteria.

871 The main systematic sources in this analysis are listed as follows:

- 872 • Monte-Carlo closure;
- 873 • UCC trigger selection bias;
- 874 • Loose v.s. tight track selection;
- 875 • Low v.s. high tracking efficiency;
- 876 • Impact of pileup rejection;
- 877 • Flattening procedure;
- 878 • Centrality definition;

879 The main cross-checks in this analysis are listed as follows:

- 880 • Event class bin width;
- 881 • η gap for subevent;

882 For simplicity, only systematics in standard cumulant are discussed, with following p_{T} ranges:

- 883 • $c_1\{4\}$: $1.8 < p_{\text{T}} < 5.0 \text{ GeV}$;
- 884 • $c_2\{4\}$: $0.5 < p_{\text{T}} < 5.0 \text{ GeV}$;
- 885 • $c_3\{4\}$: $0.5 < p_{\text{T}} < 5.0 \text{ GeV}$;
- 886 • $c_4\{4\}$: $0.5 < p_{\text{T}} < 5.0 \text{ GeV}$;

887 and for UCC trigger efficiency and pileup rejection, only systematics in ultra-central events are shown.

888 At the end of this section, the summary of systematics are shown for all the observables.

889 7.2 Ultra-central collision trigger efficiency

890 In order to have enough statistics to study the cumulant in ultra-central collisions, ultra-central collision
 891 (UCC) triggered events are included. The trigger efficiencies are evaluated for all the UCC triggers
 892 separately. In the FCal E_T region where trigger efficiency is less than 1 (turn-on region), due to the
 893 different tracking reconstructions between online and offline, event selection bias might be introduced to
 894 the analysis.

895 As one example, Fig. 22 shows the FCal E_T distributions from MinBias and one of the UCC triggers:
 896 HLT_hi_th1_ucc_L1TE10000 (left). This UCC trigger provides 2 times statistics than the MinBias
 897 trigger, in high FCal E_T region, while the other UCC triggers provides more than 5 times statistics. The
 898 right plot shows the trigger efficiency. During the data taking, both MinBias and UCC triggers are heavily
 899 prescaled (except for the UCC triggers with highest threshold, which is running un-prescaled in most of
 900 the runs), and this means that the number of recorded events passing both MinBias and UCC triggers are
 901 extremely small. In order to evaluate the efficiency, we define the trigger "efficiency" on the statistical
 902 level:

$$\epsilon \equiv \frac{\sum (\text{event passing UCC} * \text{prescale})}{\sum (\text{event passing MinBias trigger} * \text{prescale})} \quad (65)$$

903 Since the efficiency is defined on the statistical level, at large FCal E_T , the efficiency saturates towards
 904 1, but not exactly at 1, as shown in the right plot of Fig. 23. Due to the strong correlation between
 905 online and offline FCal E_T , the turn-on curve of UCC triggers are very sharp, meaning that the selection
 906 bias due to UCC triggers are minimal. To be conservative, we still determined the FCal E_T cut at 80%
 907 efficiency for 3 sets of UCC triggers:

- 908 • FCal E_T cut = 4.209 TeV for th1;
- 909 • FCal E_T cut = 4.364 TeV for th2;
- 910 • FCal E_T cut = 4.541 TeV for th3;

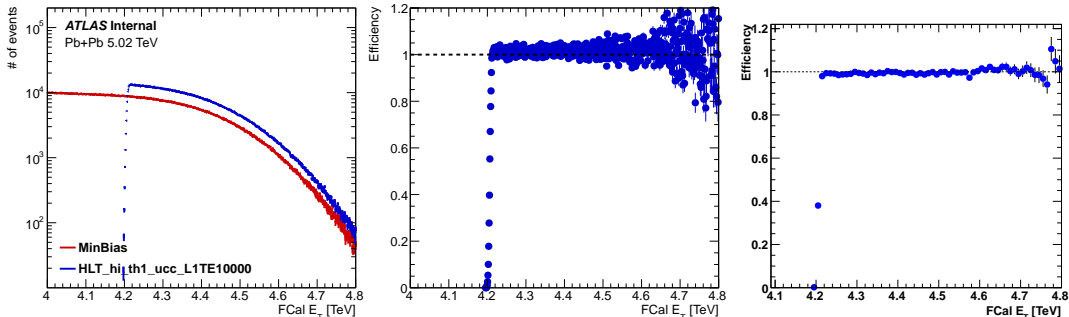


Figure 22: N_{ch} distributions from MinBias and one UCC trigger (left), trigger "efficiency" as a function of FCal E_T (middle) and a zoomed-in version (right) to better see the plateau.

911 In order to evaluate the potential selection bias, we performed the following two checks:

- 912 • Default: include UCC events with efficiency higher than 80%;
- 913 • Check: include all UCC events;

914 Fig. 23 shows the comparison of $c_n\{4\}$ calculated with (default) and without (check) the trigger
 915 efficiency selection, as a function of FCal E_T in central collision (Note UCC triggers have no impact

on events with centrality > 1%). For all the four harmonics, the relative uncertainties are much smaller compared with statistical uncertainties. This is as expected because the turn-on curve of the trigger efficiency is very sharp: not many events are rejected because of the 80% trigger efficiency selection.

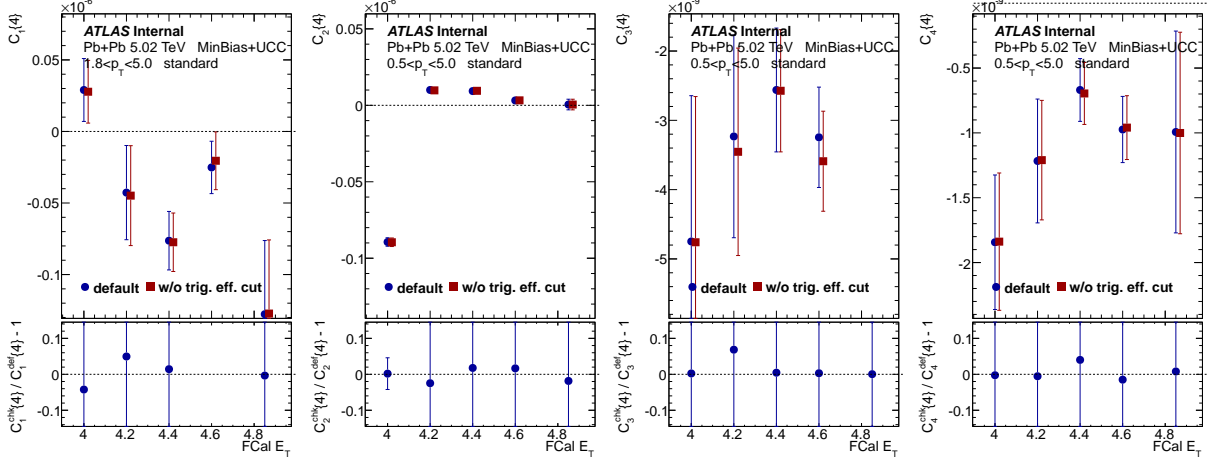


Figure 23: Systematics of $c_n\{4\}$ from UCC trigger efficiency: with v.s. without trigger efficiency cut. Bottom panels are the relative uncertainties between the default and check.

Due to much smaller systematic uncertainty compared with statistical uncertainty, trigger efficiency cut will not be quoted as part of the systematics.

7.3 Monte-Carlo closure

The HIJING Monte Carlo simulations were used to evaluate the difference between multi-particle cumulants in Pb+Pb data calculated using the generated and reconstructed charged particles obtained using the same analysis method. In some analysis it is considered as a crosscheck, since it assesses the quality of tracking, which are separately accounted for in previous systematics. The argument for not accounting it as a systematic uncertainties also relies on the fact that MC generators do not properly describe the investigated particle correlations. However, in this analysis, we are conservative to include the Monte-Carlo closure as part of the systematics.

Four million HIJING events with flow after-burner implemented are used for the MC closure (more details in ATLHI-116). Note that both tracking and FCal E_T are different between generated (truth) and reconstructed events, but in order to only evaluate the impact from offline tracking reconstruction, reconstructed FCal E_T , should be used for binning in both generated and reconstructed. Otherwise the differences between generated and reconstructed FCal E_T will convolute with the tracking reconstruction, and that is not the purpose of this systematic check. However, the Monte-Carlo samples are generated using fast MC simulation configurations, which creates discrepancy of Calorimeter E_T between data and MC. Due to this reason, the closure test was first binned in N_{ch}^{rec} , which is consistent with data, then mapped to the FCal $\langle E_T \rangle$ of data. In this case, the mismatch of FCal E_T between data and MC plays little role. The procedure is similar as the Run 2 v_n analysis [21].

For the reconstructed tracks, it is not required to be associated with truth track, and both efficiency and fake rates are needed for the correction. Meanwhile, we do observe that the average of ϕ distribution is not very uniform in reconstructed tracks due to the simulation of detector effects, so flattening procedure is also applied in this Monte-Carlo check. In summary, all the corrections that has been applied in data analysis are also repeated with the Monte-Carlo test.

Fig. 24 shows the $c_n\{4\}$ calculated from generated and reconstructed particles. Since the HIJING sample has flow implemented, both $c_2\{4\}$ and $c_3\{4\}$ show similar centrality dependence as data: largest in mid-central and approaches 0 in central and peripheral. The relative differences are largest in central: reaching 3%, even after the efficiency and fake corrections are applied to the reconstructed tracks. As to $c_1\{4\}$ and $c_4\{4\}$, the centrality dependence is very different compared with data and the statistical errors are quite large. Due to these reasons, relative differences for $c_1\{4\}$ and $c_4\{4\}$ are not quoted as part of the systematics.

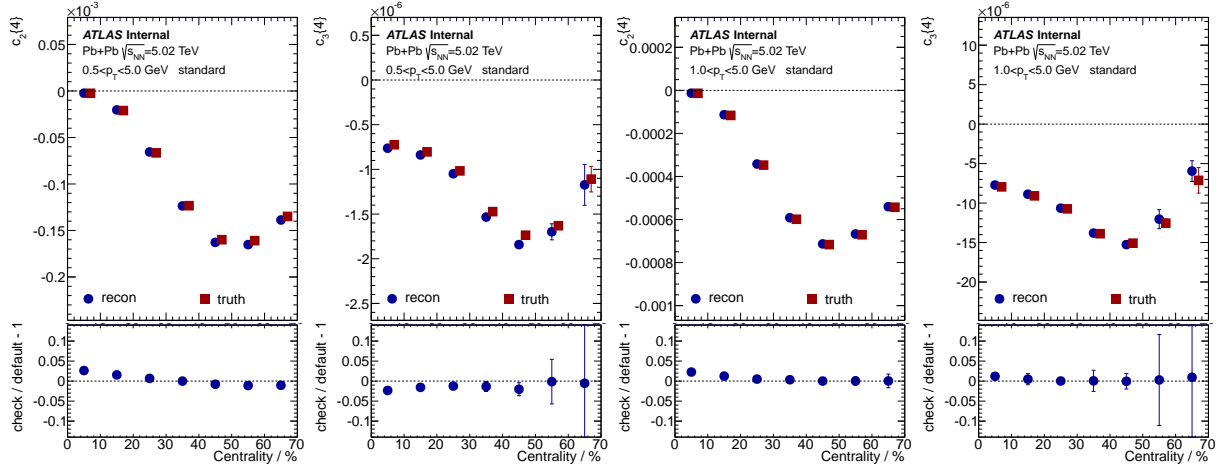


Figure 24: Systematics of $c_n\{4\}$ from MC closure: generated v.s. reconstructed. Bottom panels are the relative uncertainties between the default and check. Note that the relative difference for $c_1\{4\}$ and $c_4\{4\}$ are set to be 0 (see main text).

In addition, we have tested the following checks trying to diminish the 10% differences observed in $c_2\{4\}$ and $c_3\{4\}$:

- Using a different 0.5 million HIJING sample (see in ATLHI-84): similar outcome;
- Do not apply efficiency or fake correction to reconstructed tracks: larger difference;
- Only apply tracking efficiency: larger difference in central;
- Apply flattening procedure on reconstructed tracks: similar outcome;
- Apply additional d_0 and z_0 significance cuts to reconstructed tracks: larger difference;

Unfortunately, average efficiency and fake corrections will not compensate the inefficiency of reconstruction of tracks. To be conservative, the relative differences are quoted as systematics for both $c_2\{4\}$ and $c_3\{4\}$. As to the systematics in ultra-central collisions, since this HIJING sample does not contain enough ultra-central events, the systematic errors in UCC events are quoted from the plots above (error from the most central bin).

Since HIJING simulation does not implement correlation between flow harmonics, as shown in Fig. 25(the signals are much smaller compared with data), systematics from MC closure for symmetric and asymmetric cumulant are set to be 0.

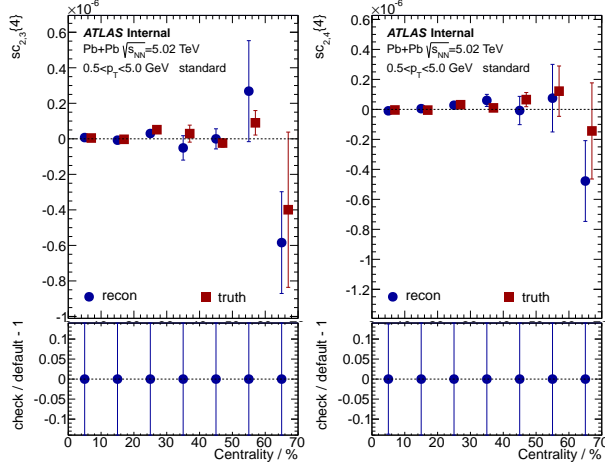


Figure 25: Systematics of symmetric cumulants from MC closure: generated v.s. reconstructed. Bottom panels are the relative uncertainties between the default and check. Note that the relative differences are set to be 0 (see main text).

966 7.4 Loose and tight track selection

967 As default, the heavy ion loose track quality cut is applied in this analysis. In order to check stability of
968 the track selection cuts, analysis is also repeated with tight track quality cut:

- 969 • Default: HI loose quality cut;
- 970 • Check: HI tight quality cut;

971 where the definitions of loose and tight are listed in Section 4.

972 Fig. 26 compares the $c_n\{4\}$ calculated with HI loose and tight track selection. For $c_2\{4\}$ and $c_3\{4\}$,
973 the relative differences are within 3% for all centralities. While for $c_1\{4\}$ and $c_4\{4\}$, since the signal is
974 much smaller, the relative errors go up to 10%, but still within statistical uncertainties. This is not sur-
975 prising because even though different track selections give different fake rates, they are already corrected
976 using Monte-Carlo. Systematics from track selection are quoted as part of the combined systematics, for
977 all the harmonics.

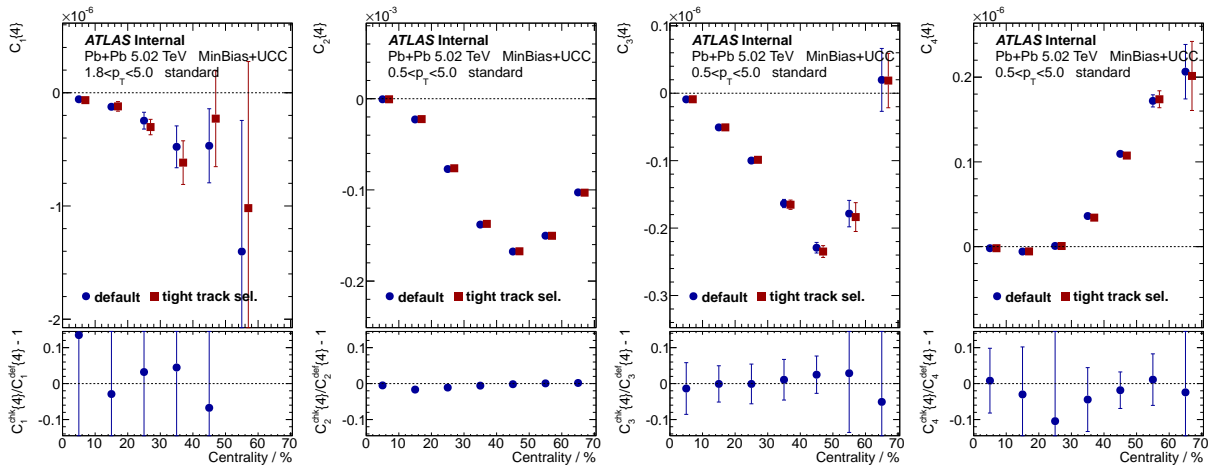


Figure 26: Systematics of $c_n\{4\}$ from track selections: HI loose v.s. HI tight. Bottom panels are the relative uncertainties between the default and check.

978 7.5 Lower and higher tracking efficiency

979 In this analysis, tracking efficiency is evaluated as a function of p_T , η and centrality. Previous flow
 980 measurements have shown that v_n strongly depends on p_T : it increases then decreases as p_T increases.
 981 Meanwhile, differential flow measurements also shows that v_n is weakly dependent of η . Due to these
 982 reasons, the p_T weighting in tracking efficiency could introduce uncertainty to the results.

983 To evaluate the impact from uncertainty in the tracking efficiency, the following checks are per-
 984 formed:

- 985 • Default ϵ : particles weighted by tracking efficiency;
- 986 • Check 1 higher efficiency ϵ_+ : tracking efficiency in high p_T is increased to its maximum within
 987 uncertainty; while tracking efficiency in low p_T is decreased to its minimum within uncertainty;
- 988 • Check 2 lower efficiency ϵ_- : tracking efficiency in high p_T is decreased to its minimum within
 989 uncertainty; while tracking efficiency in low p_T is increased to its maximum within uncertainty;

990 where the two checks can be parameterized as:

$$\epsilon_{\pm}(p_T) \equiv \epsilon(p_T) \pm 0.06 \frac{\epsilon(p_T) - \epsilon(p_T^{\text{low}})}{\epsilon(p_T^{\text{high}}) - \epsilon(p_T^{\text{low}})} \mp 0.03 \quad (66)$$

991 where p_T^{low} is 0.5 GeV while p_T^{high} is 5.0 GeV, which are the minimum and maximum p_T ranges of this
 992 analysis.

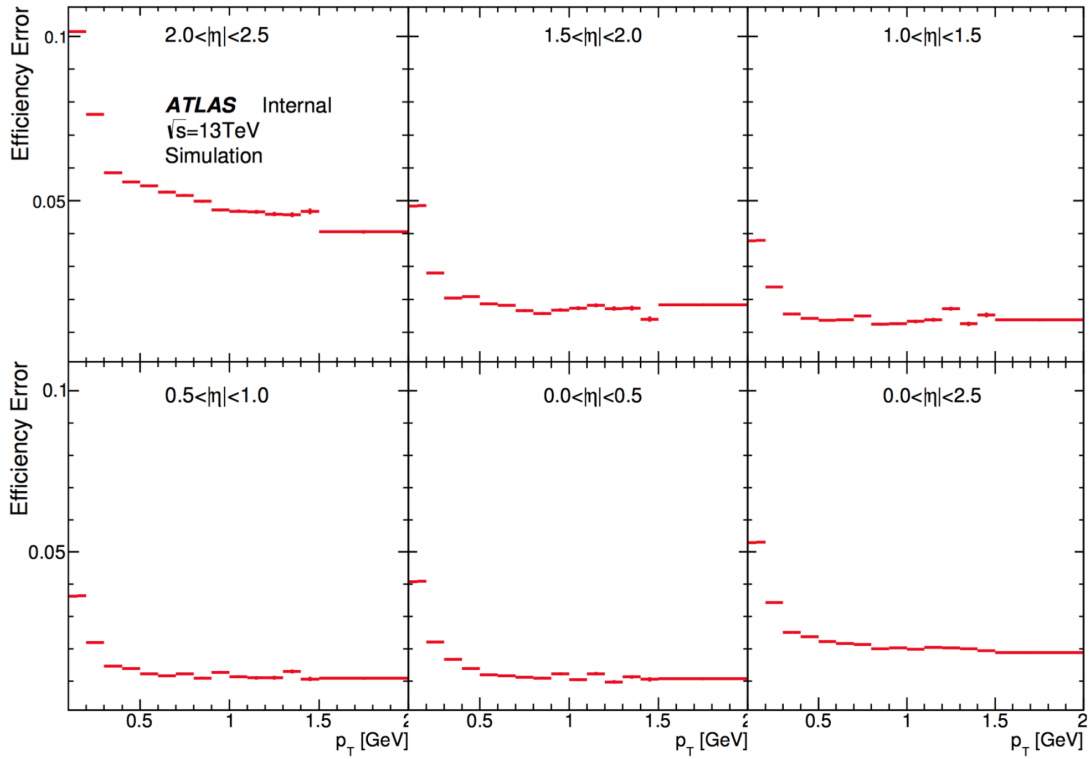


Figure 27: The systematic uncertainties of the tracking efficiency plotted as a function of p_T for several $|\eta|$ slices. These include the material uncertainties. These were obtained from the 13 TeV multiplicity analysis. [23]

Note that 0.03 was selected as the variation of the tracking efficiency, which has been evaluated in the Minimum Bias multiplicity in 13 TeV pp analysis [23]. The total uncertainty in tracking is shown in Fig. 27, and the maximum variation for $p_T > 0.5$ GeV is about 3%.

Fig. 28 and fig. 29 show the comparison of $c_n\{4\}$ calculated using default tracking efficiency and lower/higher variations. For all the harmonics, the relative differences have opposite sign between lower and higher efficiency, as expected due to the p_T dependence of flow. The largest relative differences come from low p_T range, and decrease quickly as minimum p_T cut increase. This check will be quoted as part of the combined systematics.

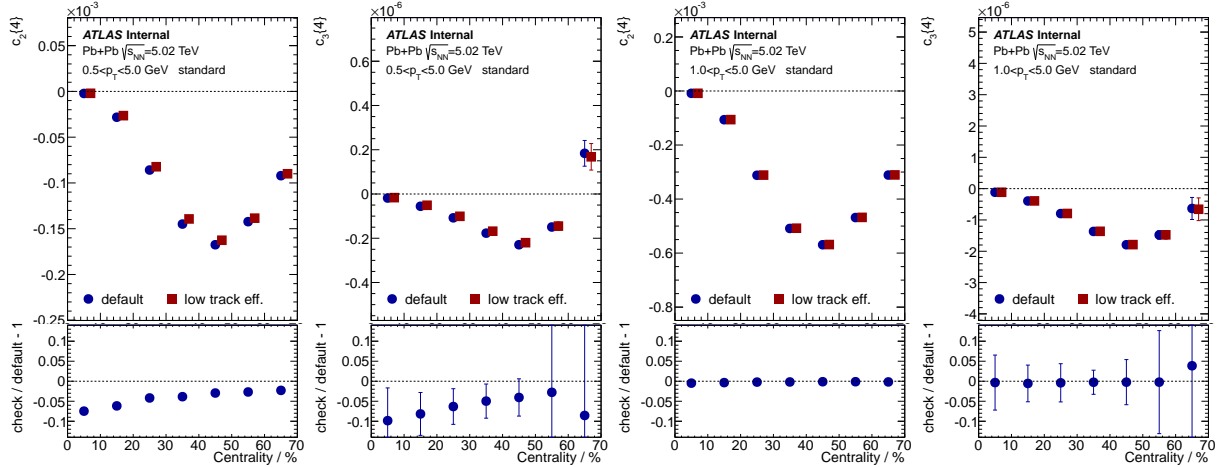


Figure 28: Systematics of $c_n\{4\}$ from tracking efficiency: default v.s. lower efficiency. Bottom panels are the relative uncertainties between the default and check.

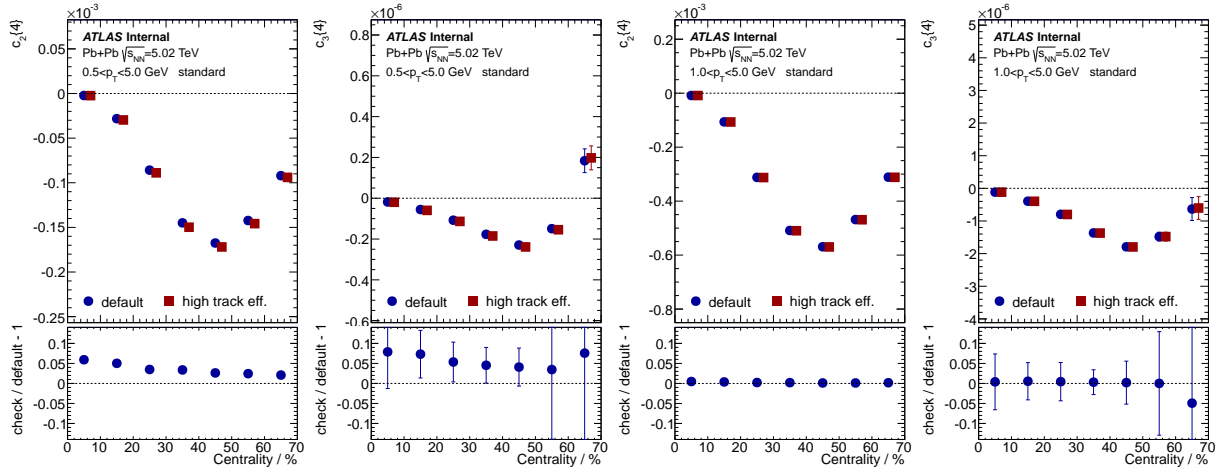


Figure 29: Systematics of $c_n\{4\}$ from tracking efficiency: default v.s. higher efficiency. Bottom panels are the relative uncertainties between the default and check.

1001 7.6 Pileup rejection

1002 During the 2015 Pb+Pb data taking, the mean value of μ is around 0.001, which means the fraction
1003 of pileup events is very low compared with pp or $p+Pb$ samples. Furthermore, in this analysis all the
1004 tracks used to calculate cumulants are from the primary vertex. In principle, in pile-up events, tracks from

1005 pile-up vertex should not contribute to the measurement. However, in the track and vertex reconstruction,
 1006 when a pile-up vertex is too close to the primary vertex, two vertices might be merged. Since the particles
 1007 from two different vertices are totally uncorrelated, including these events with merged vertex will reduce
 1008 the signal of flow signal.

1009 In order to check the impact from pileup events, a variation of pileup cleaning is performed:

- 1010 • Default: official HI pileup rejection tool, based on FCal E_T and ZDC;
 1011 • Check: alternative pileup rejection method, based on FCal E_T and tracks N_{ch} ;

1012 Fig. 30 illustrates the differences between the two pileup cleaning methods: official (left) and alterna-
 1013 tive (right). The left panel shows the correlation between FCal sum E_T and calibrated number of neutrons
 1014 in the ZDC. The main band (light blue circle) is dominated by the events with a single primary vertex
 1015 and the "grass" above the main band (light red circle) are mainly from pileup events. This is because
 1016 both the sum E_T and number of neutrons in a pileup event are larger than the corresponding single event.
 1017 In order to clean up the pileup events, a significance cut (indicated by the red curve) was applied to reject
 1018 the top 0.1% events at each FCal sum E_T slice. From this correlation map, it is obvious that the pileup
 1019 events and single events are disentangled at very high FCal sum E_T , meaning that almost all the pileup
 1020 events are rejected with the official pileup tool. As a comparison, the right panel shows the correlation
 1021 between FCal sum E_T and the number of tracking efficiency corrected reconstructed tracks N_{ch} . Simi-
 1022 lar as the left panel, the "grass" under the main band are from the pileup events. However, since FCal
 1023 sum E_T and N_{ch} are correlated, the overlap region between the pileup events and single events is much
 1024 larger than the previous case, where the $N_{neutron}$ and FCal sum E_T are anti-correlated. This means the
 1025 performance of this alternative pileup rejection method is much worse than the official, which provides
 1026 sufficient variations as a cross-check.

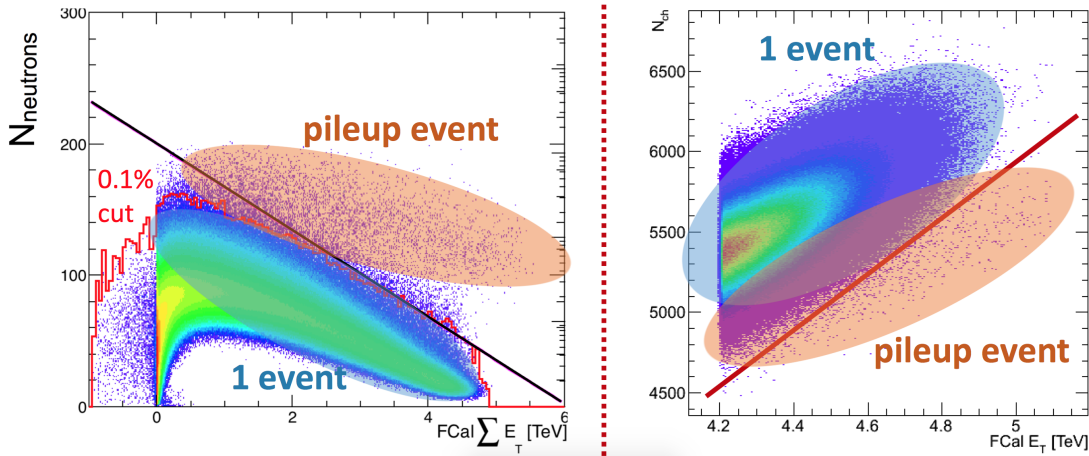


Figure 30: An illustration of two pileup rejection methods: official HI pileup tool (left) and private pileup rejection (right).

1027 The fraction of pileup events in peripheral is minimal and it increases fast with FCal E_T , so only
 1028 comparisons in UCC events are shown. But note that this systematic check is also performed for the
 1029 whole centrality range. It is worth mentioning that this check overestimates the pileup impact since the
 1030 fraction of residual pileup events are large using the alternative rejection. Another way to estimate the
 1031 impact from pileup would be by adjusting the significance cut of $N_{neutron}$, and check the trend of $c_n\{4\}$
 1032 as a function of various ZDC energy cut. To be conservative, we are quoting the difference between the
 1033 two methods as the upper bound of the systematics for pileup effects.

1034 The comparison of $c_n\{4\}$ calculated with and without pileup rejection is shown in Fig. 31, as a
 1035 function of FCal E_T in ultra-central collisions. For all the harmonics, the relative differences are within
 1036 10% and within statistical uncertainties. It is quoted as part of the systematics.

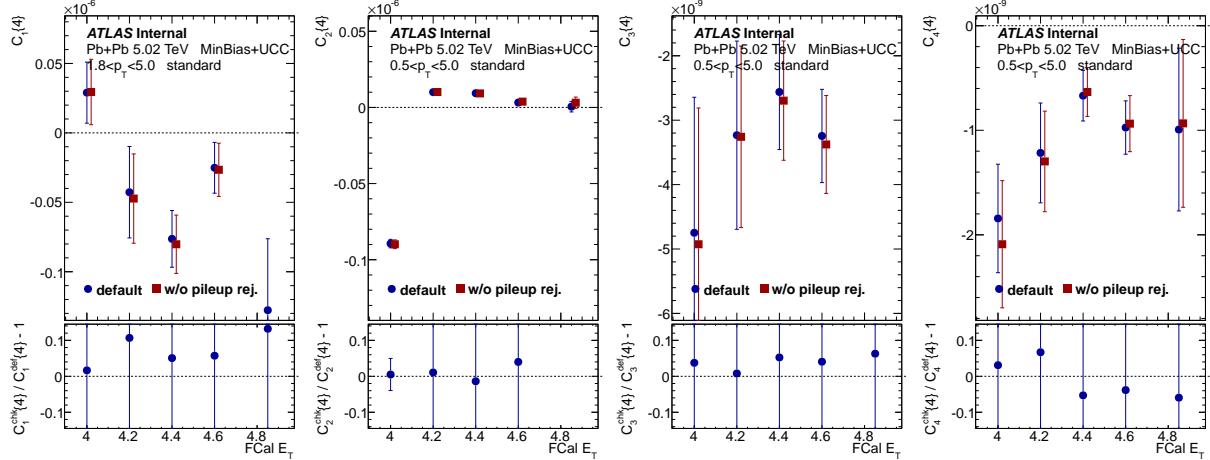


Figure 31: Systematics of $c_n\{4\}$ from pileup effects: with s.s. without pileup rejection. Bottom panels are the relative uncertainties between the default and check.

1037 7.7 Detector effects from flattening procedure

1038 Tracking efficiency weighting corrects the possible detector effects as a function of η and p_T , but the
 1039 residual detector effects could still remain in the ϕ direction. In heavy ion collision, since the event plane
 1040 angle is random from event to event, the ϕ distribution averaged over many events should be flat and the
 1041 discrepancy is due to the detector effects.

1042 To estimate the impact from detector effects, the flattening procedure was performed. The correction
 1043 factor, w_ϕ , is defined as:

$$w_\phi(\eta, \phi) \equiv \frac{\langle N(\delta\eta) \rangle}{N(\delta\eta, \delta\phi)} \quad (67)$$

1044 where $N(\delta\eta, \delta\phi)$ is the number of particles in the small (η, ϕ) phase-space window; and $\langle N(\delta\eta) \rangle$ is the
 1045 mean number of particles in the small η slice averaged over the whole ϕ range. w_ϕ is evaluated run-
 1046 by-run, as a function of p_T , vertex position z_{vtx} and charge, so that it can properly correct the detector
 1047 effects.

1048 To illustrate how the flattening works, Fig. 32 shows the $\eta - \phi$ distributions before (left) and after
 1049 (right) flattening. Several holes are observed in the raw $\eta - \phi$ distribution, while after flattening, the
 1050 average ϕ distribution is flat by construction in each η slice.

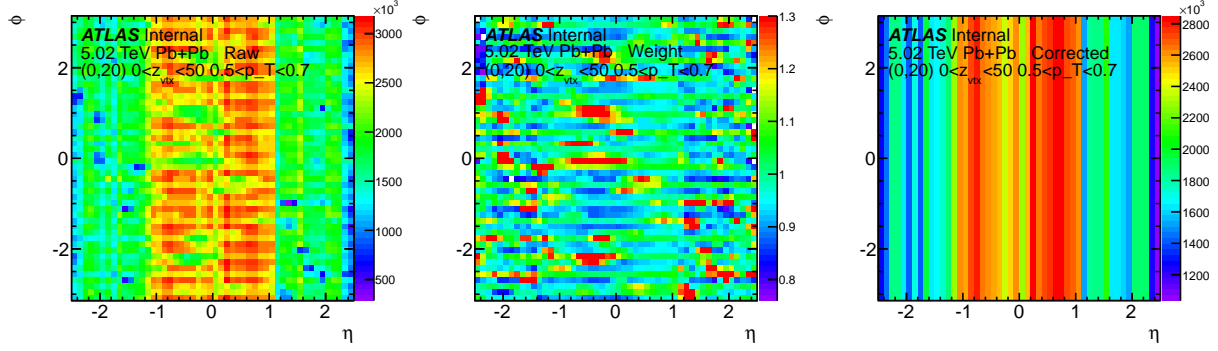


Figure 32: An example demonstrating how flattening works. Left plot is the raw $\eta - \phi$ distribution, while right plot is the $\eta - \phi$ distribution after flattening procedure. Middle panel shows the correction factor w_ϕ .

To check the impact from flattening correction, we have performed:

- Default: each particle weighted by w_ϕ ;
- Check: particles not weighted by w_ϕ ;

A comparison of $c_n\{4\}$ before and after flattening is shown in Fig. 33. For all the harmonics, the relative differences are within 10% and within statistical uncertainties. However, the relative difference seems to increase towards the central collision. Since the detector effect indeed depends on the occupancy of detector, it is worth checking the impact from flattening in UCC in details.

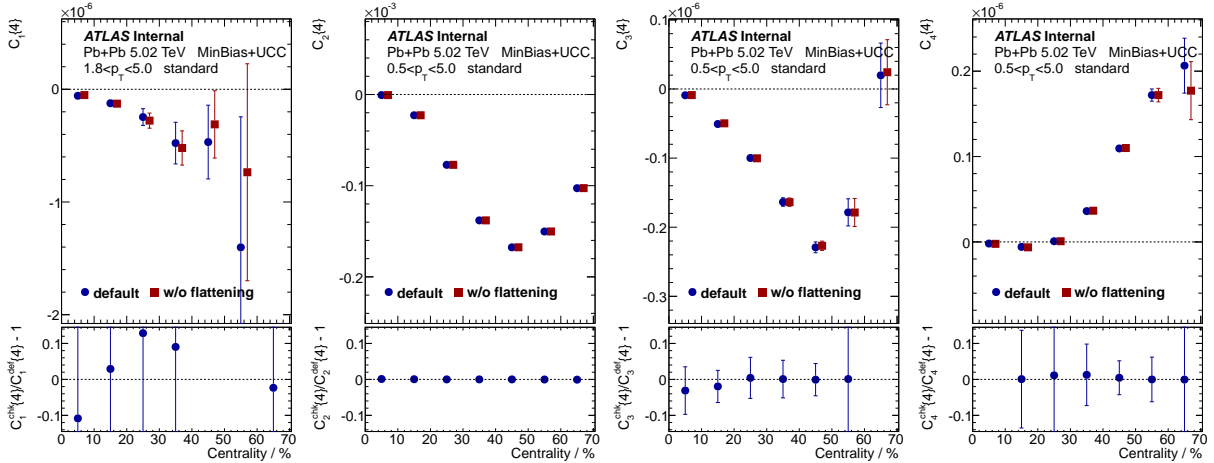


Figure 33: Systematics of $c_n\{4\}$ from flattening procedure: with and without flattening. Bottom panels are the relative uncertainties between the default and check.

A comparison of $c_n\{4\}$ in ultra-central collisions before and after flattening is shown in Fig. 34. For the odd harmonics $c_1\{4\}$ and $c_3\{4\}$, flattening does not change the results too much: the relative differences are within 10% and still within statistical errors. However, for the even harmonics, especially for $c_2\{4\}$, the positive magnitude without flattening is smaller than default. Since the flattening is an essential procedure to account for the detector effects. This check will be quoted as the systematics.

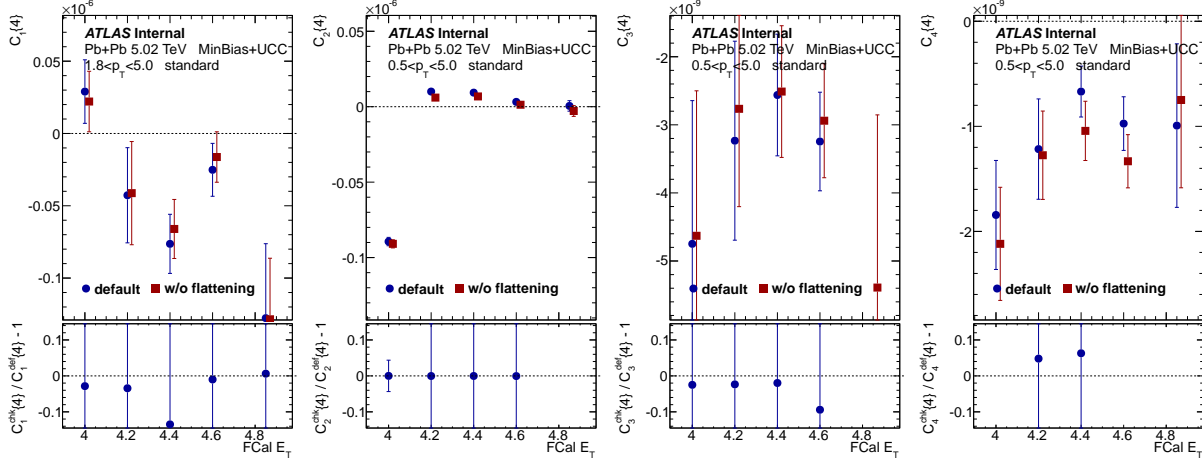


Figure 34: Systematics of $c_n\{4\}$ in ultra-central collisions from flattening procedure: with and without flattening. Bottom panels are the relative uncertainties between the default and check.

1063 A proper way to estimate the residual detector effects after flattening should be through mixed events
1064 technique, as has been discussed in Sec. 6.

1065 7.8 Centrality definition

1066 Uncertainty in how well the min-bias triggers sample the Pb+Pb cross-section (i.e. the min-bias trigger
1067 efficiency) results in an uncertainty in the definition of the centrality intervals. This causes the nominal
1068 (0 – 85)% centrality range to have a $\pm 1\%$ uncertainty. The effect of such uncertainties on observables
1069 are determined by re-evaluating the observables with the following criteria:

- 1070 • Default: (0 – 85)% centrality range;
- 1071 • Check 1: (0 – 84)% centrality range;
- 1072 • Check 2: (0 – 86)% centrality range;

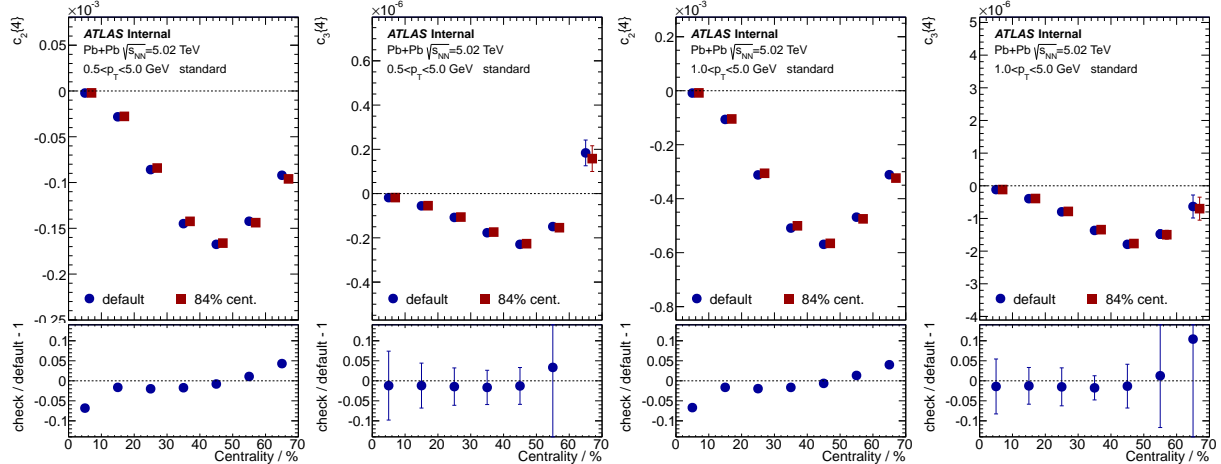


Figure 35: Systematics of $c_n\{4\}$ from centrality definition: (0 – 85)% v.s. (0 – 84)% . Bottom panels are the relative uncertainties between the default and check.

Fig. 35 compares the $c_n\{4\}$ for the different centrality ranges. This systematic uncertainty depends on the centrality dependence of the observable: if the observable has no centrality dependence, the uncertainty is zero. On the other hand, this uncertainty is large if the observable is strongly dependent of centrality. This explains why this uncertainty for $c_3\{4\}$ is larger than that of $c_2\{4\}$. Different p_T ranges make little difference since the relative centrality dependence of the observables do not change much.

7.9 Event class bin width

As has been discussed in Sec. 6, cumulant is sensitive to the definition of event class, which is associated with the multiplicity fluctuation. In order to suppress the multiplicity fluctuation, while calculating the multi-particle correlation, the events are always binned with 1% centrality bin width, which is sufficient for cumulant-like analysis [8]. However, unlike in small systems, since the non-flow contribution is much smaller in Pb+Pb collisions, different bin widths will not trigger non-flow fluctuations. However, different bin widths could still result in different flow fluctuations, especially when the bin width is too large. So it is worthwhile to check the impact of event class bin width:

- default: 1% centrality as the event class bin width;
- check: 5% centrality as the event class bin width;

Fig. 36 shows the comparison of $c_n\{4\}$ calculated with two event class bin widths. For the lower harmonics $c_1\{4\}$ and $c_2\{4\}$, the relative differences are within statistics errors. While for the higher order harmonics $c_3\{4\}$ and $c_4\{4\}$, since flow signal is smaller, the flow fluctuation becomes larger. This explains why the relative differences of $c_3\{4\}$ and $c_4\{4\}$ between two event class bin widths are larger. This cross-check illustrates the importance of narrow bin width in the cumulant calculation, but it will NOT be quoted as part of the systematics since we will always use the narrowest bin width.

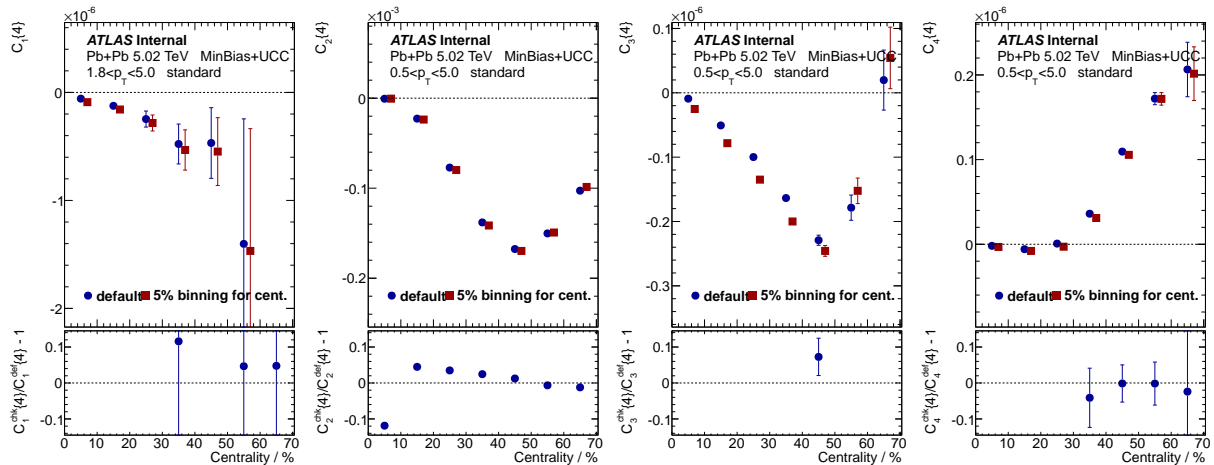


Figure 36: Systematics of $c_n\{4\}$ from different bin width: 1% v.s. 5% centrality bin widths. Bottom panels are the relative uncertainties between the default and check.

7.10 η gap for subevent

Compared with 2-subevent method, 3-subevent method is designed to remove the dijet-like correlation, where the chance that both jets contribute to all the 3 subevents are dramatically lowered. The only situation where dijet correlation still contributes is when two jets fall upon the two boundaries among

1098 3 subevents. To show whether the $c_n\{4\}$ is affected by the residual dijet contributions, we introduced η
1099 gaps between subevents.

1100 Fig. 37 is a cartoon showing how the η gap was applied to the subevent methods. For the standard
1101 cumulant method, in principle η gap can also be applied among all 4 particles. However, the formula of
1102 direct cumulant will no longer hold and one has to rely on the nested loop method. Meanwhile for the
1103 subevent methods, it is quite natural to apply the η gaps between subevents, while keeping the formula
1104 the same. In the following cross-checks, we will only test the η gap in subevent methods. After all, the
1105 subevent method is used to evaluate the residual non-flow in Pb+Pb, and if subevent cumulant with η gap
1106 gives consistent results, it means most of the dijet-like non-flow are already removed by the 3-subevent
1107 method.

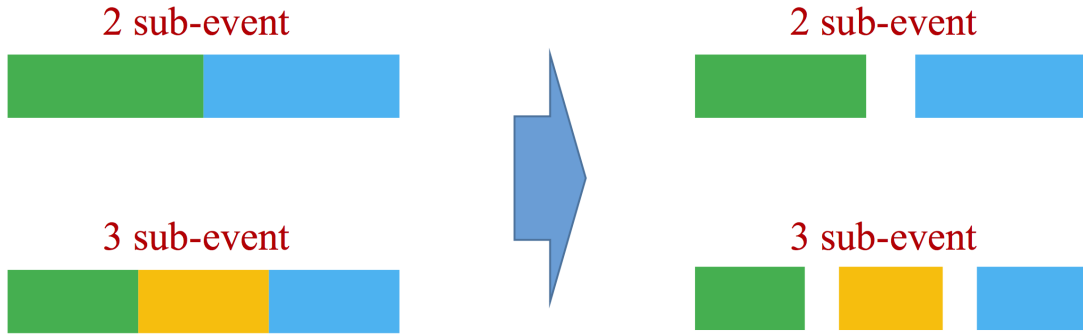


Figure 37: A cartoon showing how the η gap was applied to subevent to further suppress the long-range non-flow.

1108 Fig. 38 presents the comparisons of $c_n\{4\}$ with and without $\eta = 0.5$ gap, calculated using 3-subevent
1109 methods. For $c_2\{4\}$, since the elliptic flow is dominating over the non-flow, applying η gap has minimal
1110 impact on the results. While for $c_3\{4\}$ and $c_4\{4\}$, where the flow signals become smaller, subevent with
1111 η gap causes up to 10% difference compared with no gap. In the end, since $c_1\{4\}$ signal is even smaller,
1112 by applying the η gap, the number of particle combinations in $\langle 4 \rangle$ will drop, which results in larger
1113 statistical errors. Since the residual non-flow upon subevent cumulant is under control, this cross-check
1114 will NOT be quoted as systematics. To increase statistical significance, the default subevent method will
1115 NOT include the η gap.

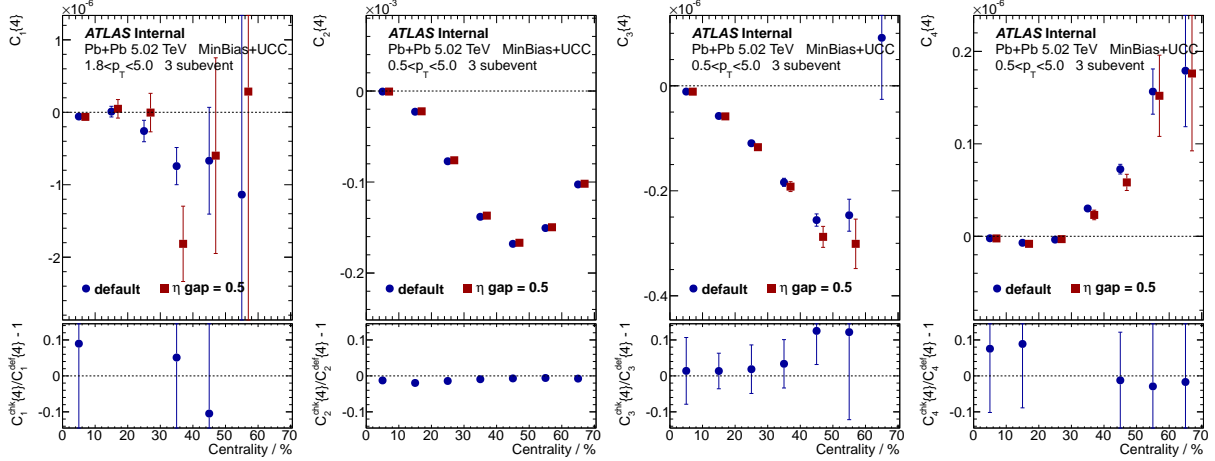


Figure 38: Systematics of $c_n\{4\}$ from η gap between subevents: with $\eta = 0.5$ gap and without gap. The $c_n\{4\}$ are calculated using 3-subevent method. Bottom panels are the relative uncertainties between the default and check.

1116 7.11 Summary of systematics

1117 This section summarizes the breakdown of systematics for every observable in this analysis. In order not
 1118 to flooding the plots, the results are shown in two p_T ranges:

- 1119 • $0.5 < p_T < 5.0 \text{ GeV}$;
- 1120 • $1.0 < p_T < 5.0 \text{ GeV}$;

1121 and except for the 2-particle cumulant, all other results are only shown using standard cumulant method.

1122 The corresponding systematics from 3-subevent method is listed in the Appendix.

1123 Overall, the summary of systematics has the following features:

- 1124 • In most cases, systematics are dominated by tracking efficiency variations. This is not surprising
 1125 since magnitude of flow, as well as its fluctuation, are highly dependent of p_T . Slightly change in
 1126 tracking efficiency as a function of p_T will cause noticeable differences to cumulants;
- 1127 • Monte-Carlo closure has significant impact on $c_n\{2k\}$: in the lower p_T region, about 5% for 2-
 1128 particle cumulant, 10% and 15% for 4- and 6-particle cumulants. In higher p_T , systematics from
 1129 MC closure become much smaller;
- 1130 • Normalized cumulant, symmetric cumulant and asymmetric cumulant have smaller systematic
 1131 errors than its correspondence without normalization, due to the reason that part of the systematics
 1132 are canceled out in the ratio;

1133 As a summary, in most cases, the total systematics are within 10%. In other cases where the system-
 1134 atics are larger, they are still smaller or comparable with statistical uncertainties.

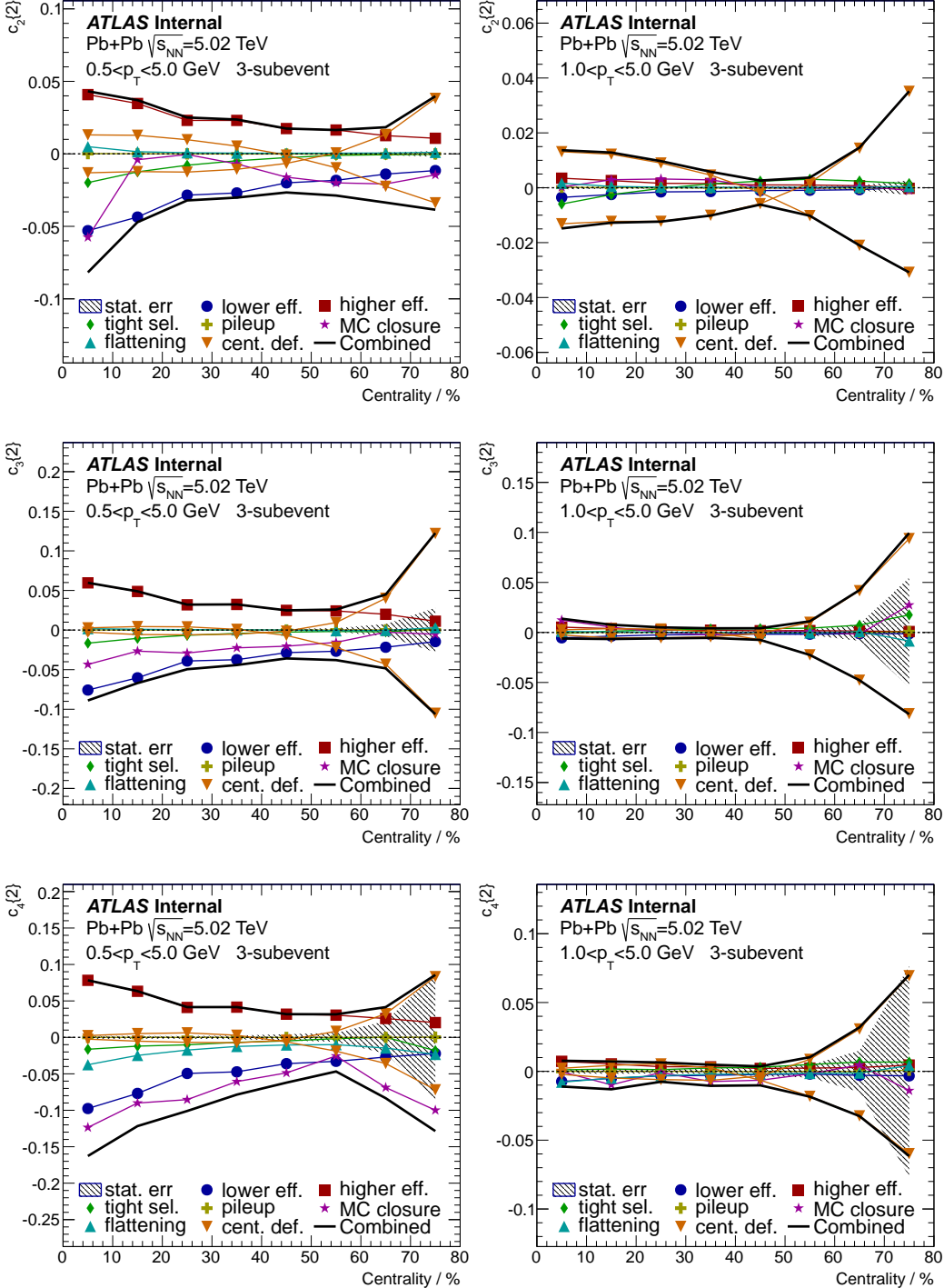
¹¹³⁵ 7.11.1 2-particle cumulant $c_n\{2\}$


Figure 39: Breakdown of all major systematic sources for 2-particle cumulant $c_n\{2\}$. Left column shows the lower p_T cut and right column shows the higher p_T cut. Different rows represent different harmonics. The cumulants are calculated using standard method. Shaded area indicate the statistical uncertainty.

¹¹³⁶ 7.11.2 4-particle cumulant $c_n\{4\}$ and $\hat{c}_n\{4\}$

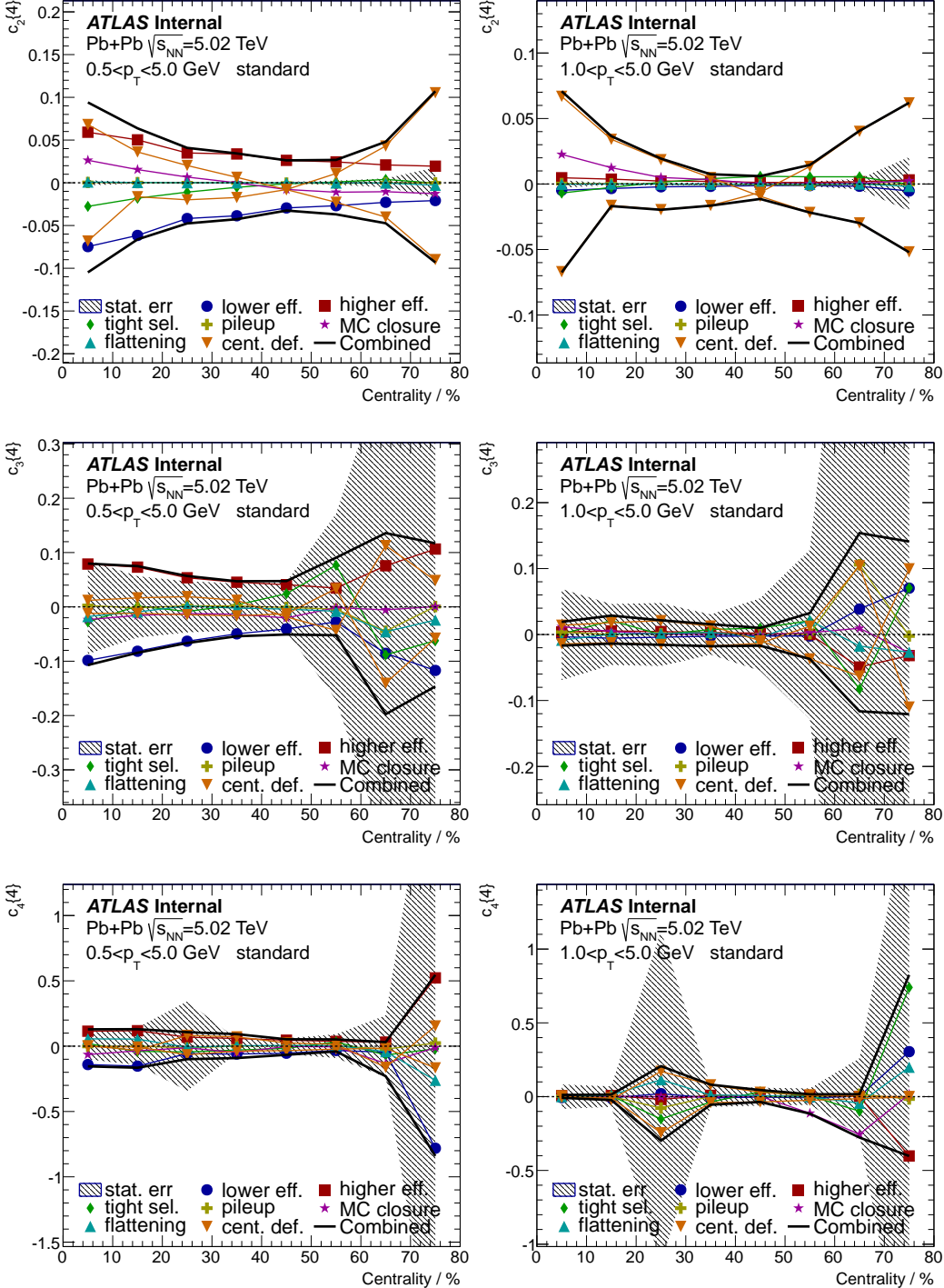


Figure 40: Breakdown of all major systematic sources for 4-particle cumulant $c_n\{4\}$. Left column shows the lower p_T cut and right column shows the higher p_T cut. Different rows represent different harmonics. The cumulants are calculated using standard method. Shaded area indicate the statistical uncertainty.

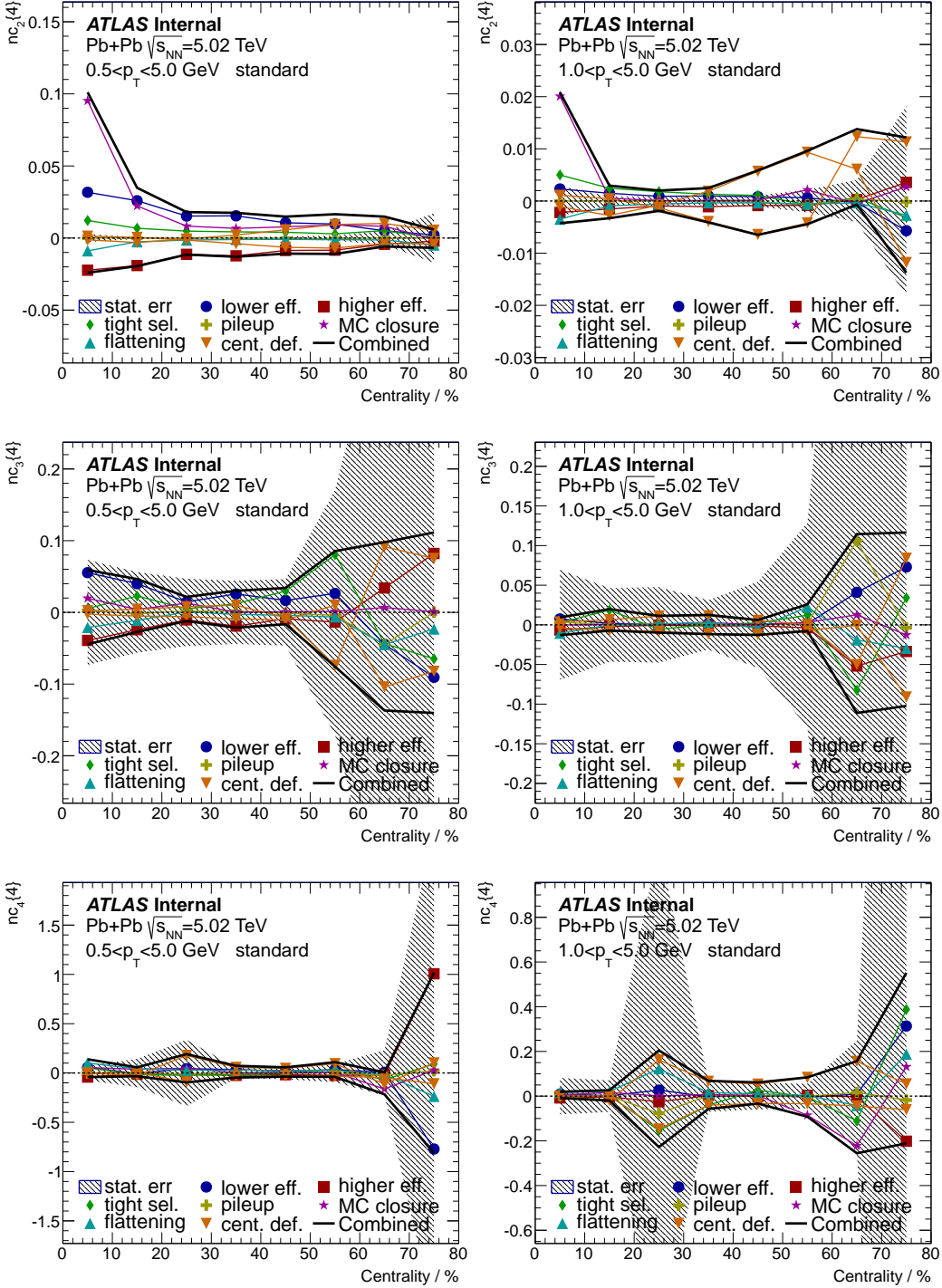


Figure 41: Breakdown of all major systematic sources for normalized 4-particle cumulant $\hat{c}_n\{4\}$. Left column shows the lower p_T cut and right column shows the higher p_T cut. Different rows represent different harmonics. The cumulants are calculated using standard method. Shaded area indicate the statistical uncertainty.

¹¹³⁷ 7.11.3 6-particle cumulant $c_n\{6\}$ and $\hat{c}_n\{6\}$

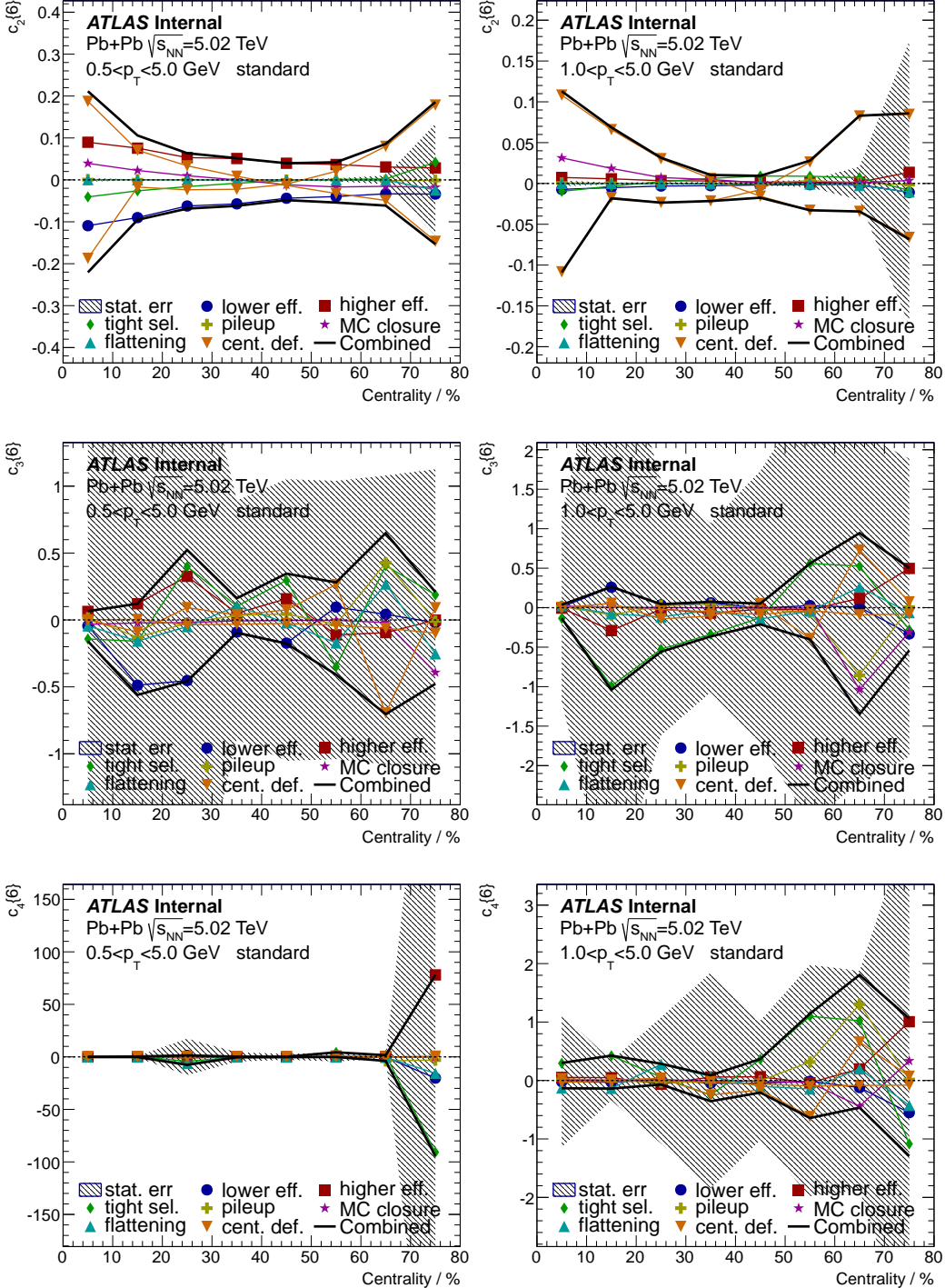


Figure 42: Breakdown of all major systematic sources for 6-particle cumulant $c_n\{6\}$. Left column shows the lower p_T cut and right column shows the higher p_T cut. Different rows represent different harmonics. The cumulants are calculated using standard method. Shaded area indicate the statistical uncertainty.

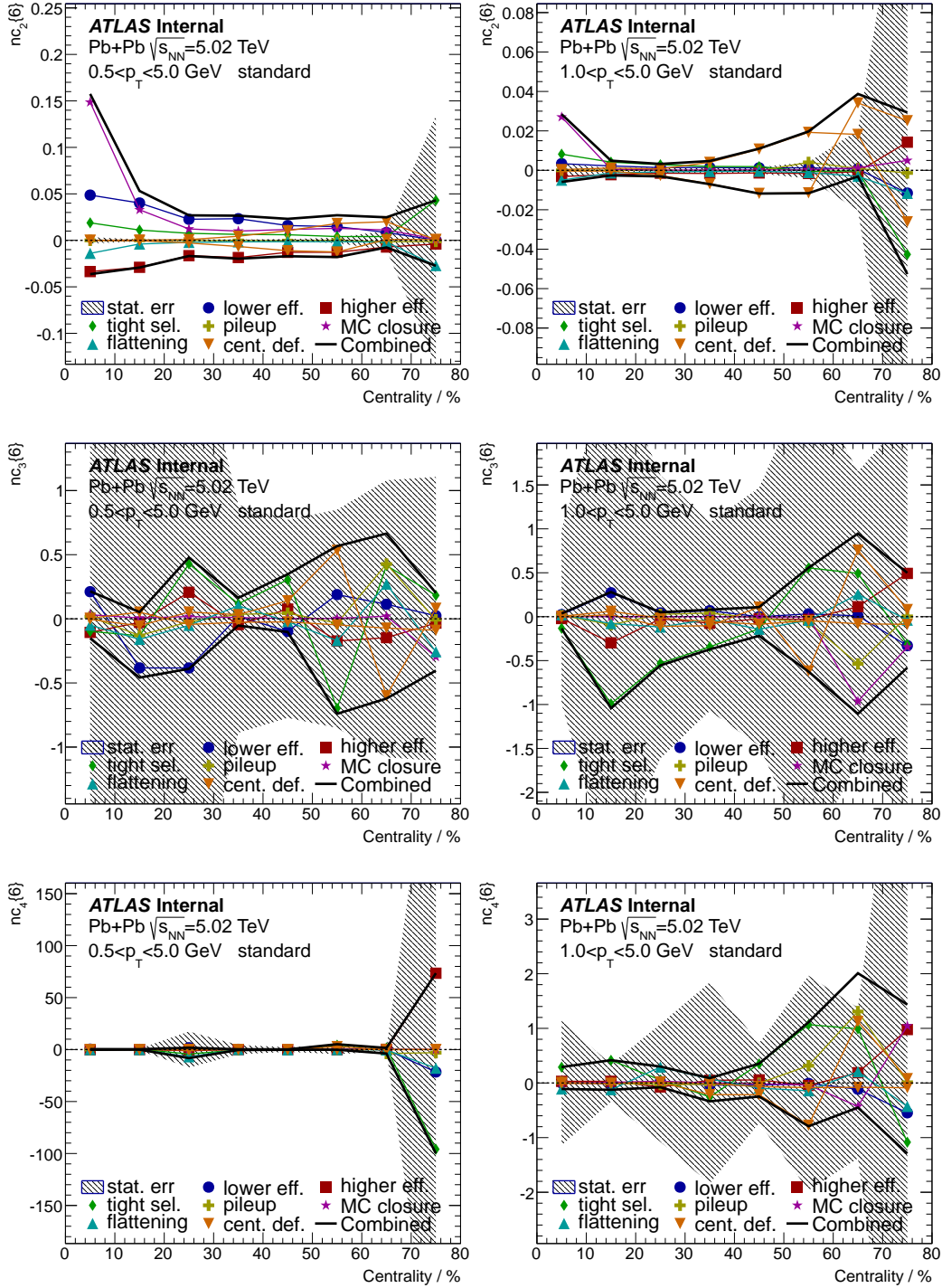


Figure 43: Breakdown of all major systematic sources for normalized 6-particle cumulant $\hat{c}_n\{6\}$. Left column shows the lower p_T cut and right column shows the higher p_T cut. Different rows represent different harmonics. The cumulants are calculated using standard method. Shaded area indicate the statistical uncertainty.

¹¹³⁸ 7.11.4 Universality check of flow fluctuation

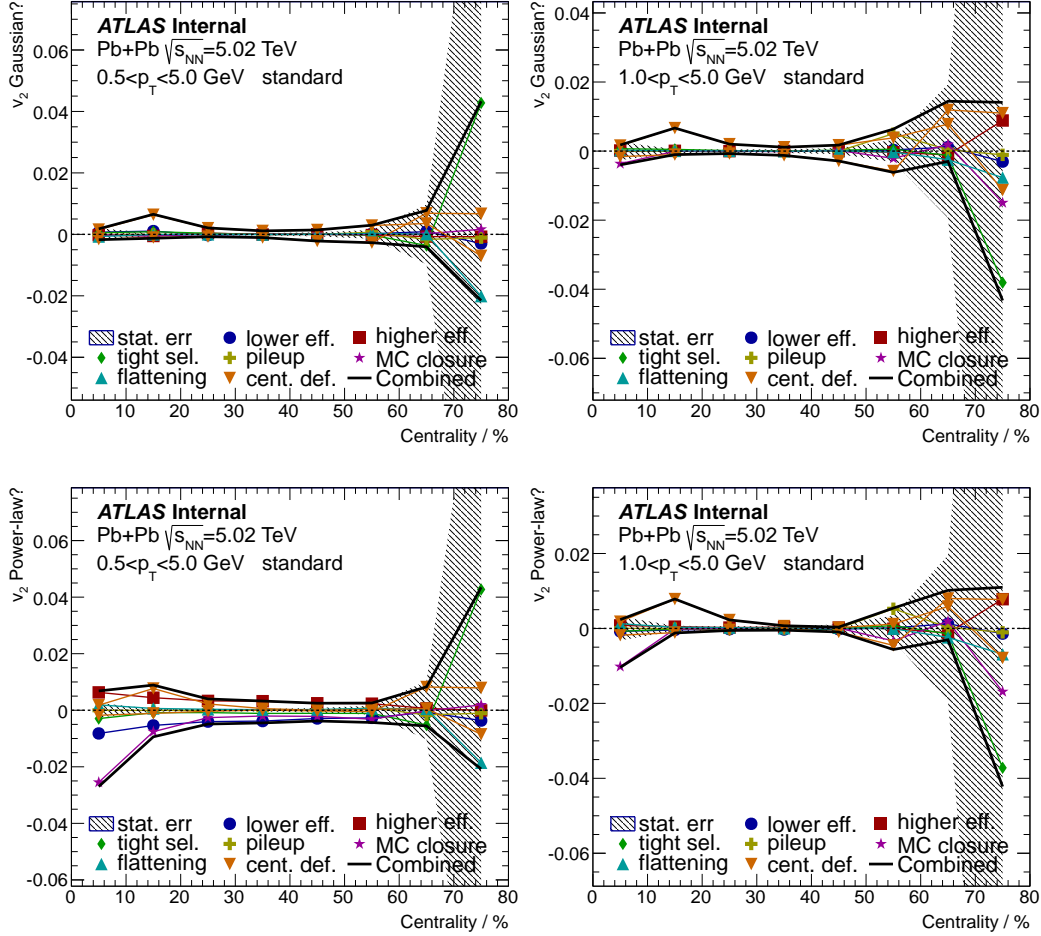


Figure 44: Breakdown of all major systematic sources for flow fluctuation check. Left column shows the lower p_T cut and right column shows the higher p_T cut. Different rows represent different fluctuation models. The cumulants are calculated using standard method. Shaded area indicate the statistical uncertainty.

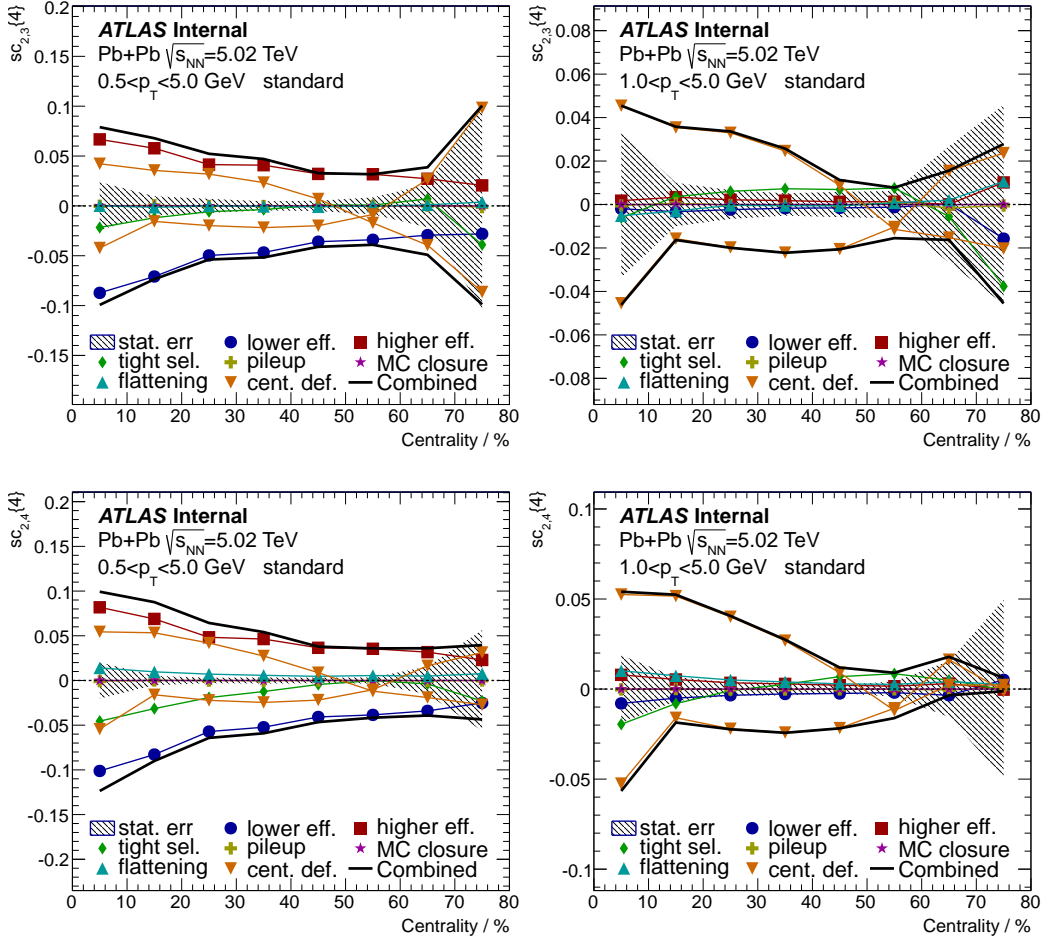
¹¹³⁹ **7.11.5 Symmetric and normalized symmetric cumulant $sc_{n,m}\{4\}$ and $nsc_{n,m}\{4\}$**


Figure 45: Breakdown of all major systematic sources for symmetric cumulant $sc_{n,m}\{4\}$. Left column shows the lower p_T cut and right column shows the higher p_T cut. Different rows represent different harmonic combinations. The cumulants are calculated using standard method. Shaded area indicate the statistical uncertainty.

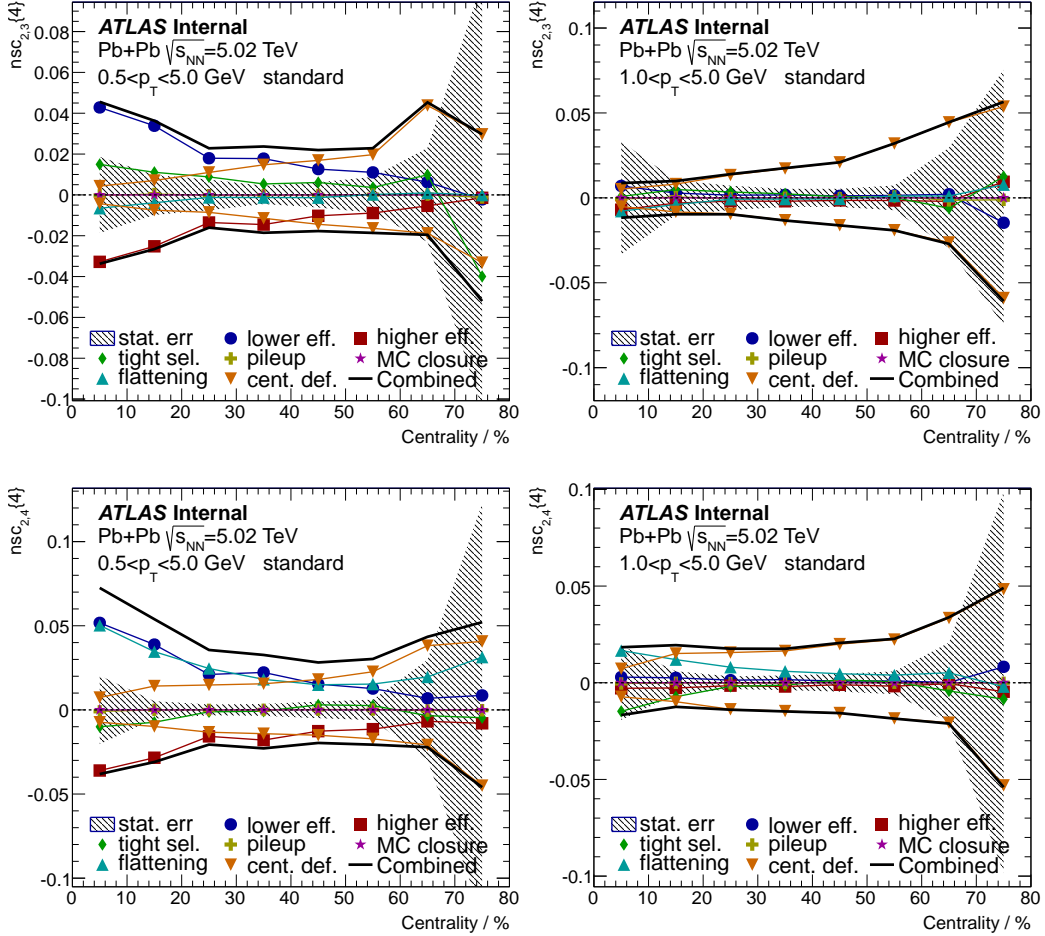


Figure 46: Breakdown of all major systematic sources for normalized symmetric cumulant $nsc_{n,m}\{4\}$. Left column shows the lower p_T cut and right column shows the higher p_T cut. Different rows represent different harmonic combinations. The cumulants are calculated using standard method. Shaded area indicate the statistical uncertainty.

¹¹⁴⁰ **7.11.6 Asymmetric and normalized asymmetric cumulant $ac_{n,n+m}\{3\}$ and $nac_{n,n+m}\{3\}$**

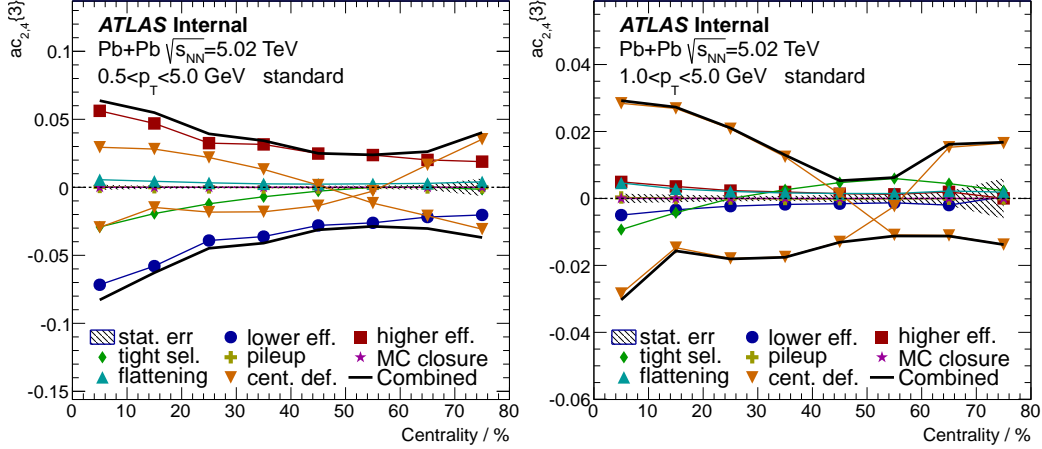


Figure 47: Breakdown of all major systematic sources for asymmetric cumulant $ac_{n,n+m}\{3\}$. Left column shows the lower p_T cut and right column shows the higher p_T cut. The cumulants are calculated using standard method. Shaded area indicate the statistical uncertainty.

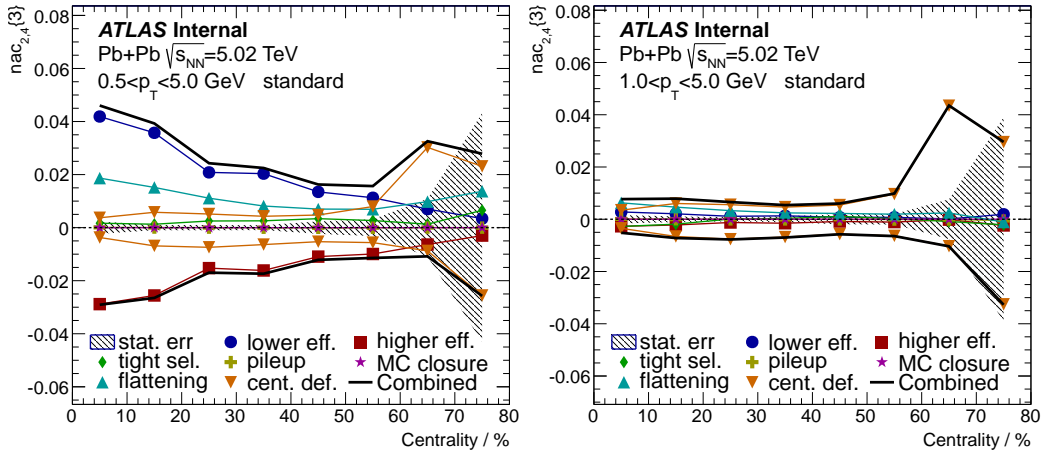


Figure 48: Breakdown of all major systematic sources for normalized asymmetric cumulant $nac_{n,n+m}\{3\}$. Left column shows the lower p_T cut and right column shows the higher p_T cut. The cumulants are calculated using standard method. Shaded area indicate the statistical uncertainty.

1141 8 Results

1142 8.1 Outline

1143 In this section, all the main results for 5.02 TeV Pb+Pb are presented as follows:

- 1144 • Comparison between standard and 3-subevent cumulant;
- 1145 • 2-particle cumulant $c_n\{2\}$;
- 1146 • 4-particle cumulant $c_n\{4\}$ and $nc_n\{4\}$;
- 1147 • 4-particle cumulant in ultra-central collisions;
- 1148 • 4-particle cumulant in 2.76 and 5.02 TeV;
- 1149 • 6-particle cumulant $c_n\{6\}$ and $nc_n\{6\}$;
- 1150 • Universality check of flow fluctuation models;
- 1151 • Symmetric cumulant $sc_{n,m}\{4\}$ and $nsc_{n,m}\{4\}$;
- 1152 • Asymmetric cumulant $ac_{n,n+m}\{3\}$ and $nac_{n,n+m}\{3\}$;

1153 Most of the results are calculated using standard cumulant method, and they are presented in the following 4 p_T ranges:

- 1155 • $0.5 < p_T < 5.0 \text{ GeV}$
- 1156 • $1.0 < p_T < 5.0 \text{ GeV}$
- 1157 • $1.5 < p_T < 5.0 \text{ GeV}$
- 1158 • $2.0 < p_T < 5.0 \text{ GeV}$

1159 In addition, three different event class definitions are applied to test impact of centrality on flow fluctuations:

- 1161 • Event class definition 1: centrality: defined by FCal E_T ;
- 1162 • Event class definition 2: FCal E_T : same as centrality but with better look in UCC;
- 1163 • Event class definition 3: N_{ch}^{rec} : different η range from FCal E_T ;

1164 8.2 Comparison between standard and 3-subevent cumulant

1165 3-subevent method was proposed to suppress the residual non-flow contribution. It measures particle 1166 correlation across different η ranges. The method has been extensively studied in small systems and 1167 proven its effectiveness. However, in large systems like Pb+Pb collision, where flow signal is dominat- 1168 ing over non-flow, the improvement from 3-subevent method is limited. In this section, we will make 1169 direct comparison between results using standard and 3-subevent methods. If the difference is not large, 1170 standard method will be the default method due to its smaller statistical uncertainties.

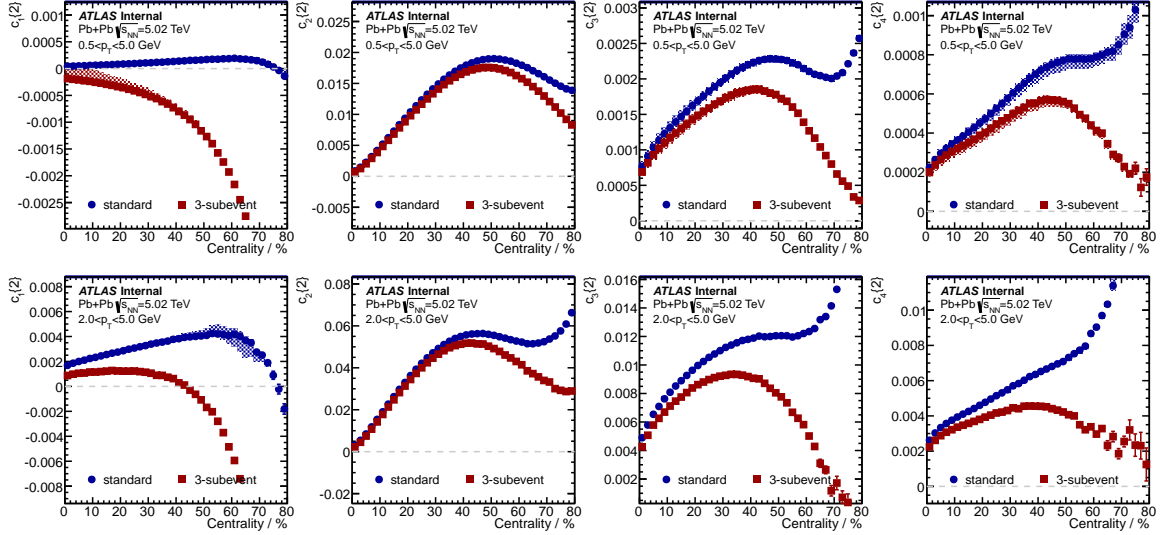


Figure 49: $c_n\{2\}$ compared between standard and 3-subevent methods, with low p_T (top) and high p_T (bottom). Different columns are for different harmonics.

Fig. 49 compares the 2-particle cumulant $c_n\{2\}$ using two methods. For second-harmonic v_2 , the differences between two methods are small in central and mid-central collisions. As the collision moves to peripheral, since number of particles deceases fast, the non-flow contributions case the growth of the differences between two methods. While for other flow harmonics, due to their smaller magnitudes, the suppression from 3-subevent method is observed even in central collision. The huge differences in v_1 is partially due to the large momentum conservation effects in standard method, which we will not discuss in details in this analysis ($c_1\{2\}$ is not included in the results). Since the statistical uncertainty for 2-particle correlation is not an issue, in order to suppress the non-flow, in this analysis, 3-subevent method is always preferred whenever 2-particle correlations are calculated (for example in the normalized cumulant).

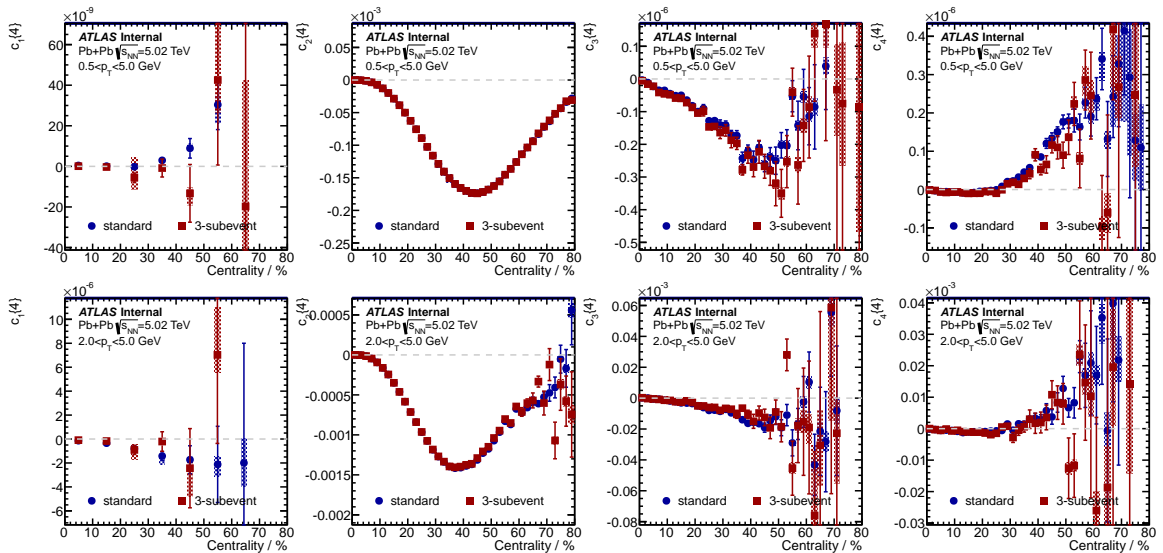


Figure 50: $c_n\{4\}$ compared between standard and 3-subevent methods, with low p_T (top) and high p_T (bottom). Different columns are for different harmonics.

Fig. 50 compares the 4-particle cumulant $c_n\{4\}$ using standard and 3-subevent methods. For v_2 , both methods give very consistent $c_2\{4\}$. This is as expected since by requiring 4 particles in the correlation calculation, the non-flow contributions are already significantly suppressed. For v_3 and v_4 , both methods are consistent within statistical uncertainties, and we do see the errors from 3-subevent are much larger. For v_1 in high p_T , 3-subevent method can also measure negative $c_1\{4\}$ in peripheral region, but with smaller statistical significance. This observation supports our claim that negative $c_1\{4\}$ is not due to non-flow contributions.

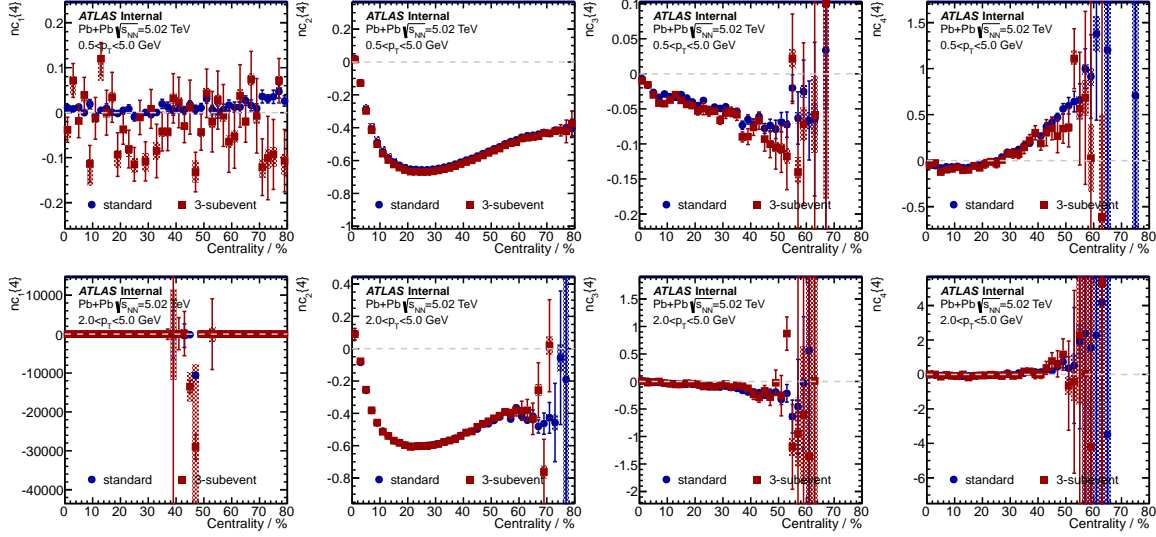


Figure 51: $nc_n\{4\}$ compared between standard and 3-subevent methods, with low p_T (top) and high p_T (bottom). Different columns are for different harmonics.

Fig. 51 shows the results for normalized 4-particle cumulant. Since both standard and 3-subevent cumulants are normalized by the 3-subevent 2-particle correlation, the behaviors of $nc_n\{4\}$ are the same as $c_n\{4\}$: both methods give consistent results. (Please ignore the leftmost column because $c_1\{2\}$ is not well defined.)

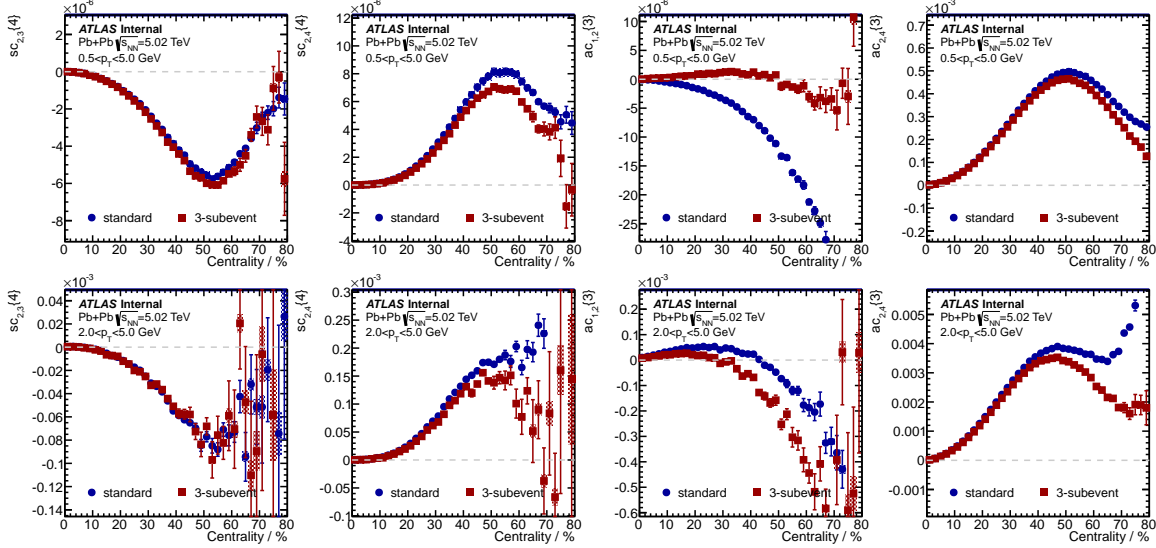


Figure 52: Symmetric and asymmetric cumulant compared between standard and 3-subevent methods, with low p_T (top) and high p_T (bottom). Different columns are for different observables.

In the end, Fig. 52 compares the 2 methods for symmetric and asymmetric cumulants. For the observables shown in the figure, both methods began to deviate towards peripheral collisions. The differences can be caused by two factors: non-flow contributions and flow decorrelation effects. Flow decorrelation effects are introduced into 3-subevent method simply because 3 events are separated in the η direction. Since in this analysis we do not tend to discuss such effects, the standard method is selected as the default one when presenting the symmetric and asymmetric cumulant results.

8.3 2-particle cumulant $c_n\{2\}$

In this section we will show the 2-particle cumulant $c_n\{2\}$ for flow harmonics v_2 , v_3 and v_4 . In each case, the $c_n\{2\}$ is calculated with 4 different p_T ranges and 3 different event class definitions. By varying the event class definitions, flow fluctuation is changing in each event class according so that we could study the potential impact of event class definition on cumulant-like analysis.

The main purpose of calculating 2-particle cumulant is to normalize 4-, 6-particle cumulant, symmetric and asymmetric cumulants. In order to suppress the large residual non-flow, we will always apply the 3-subevent method when calculate 2-particle correlation.

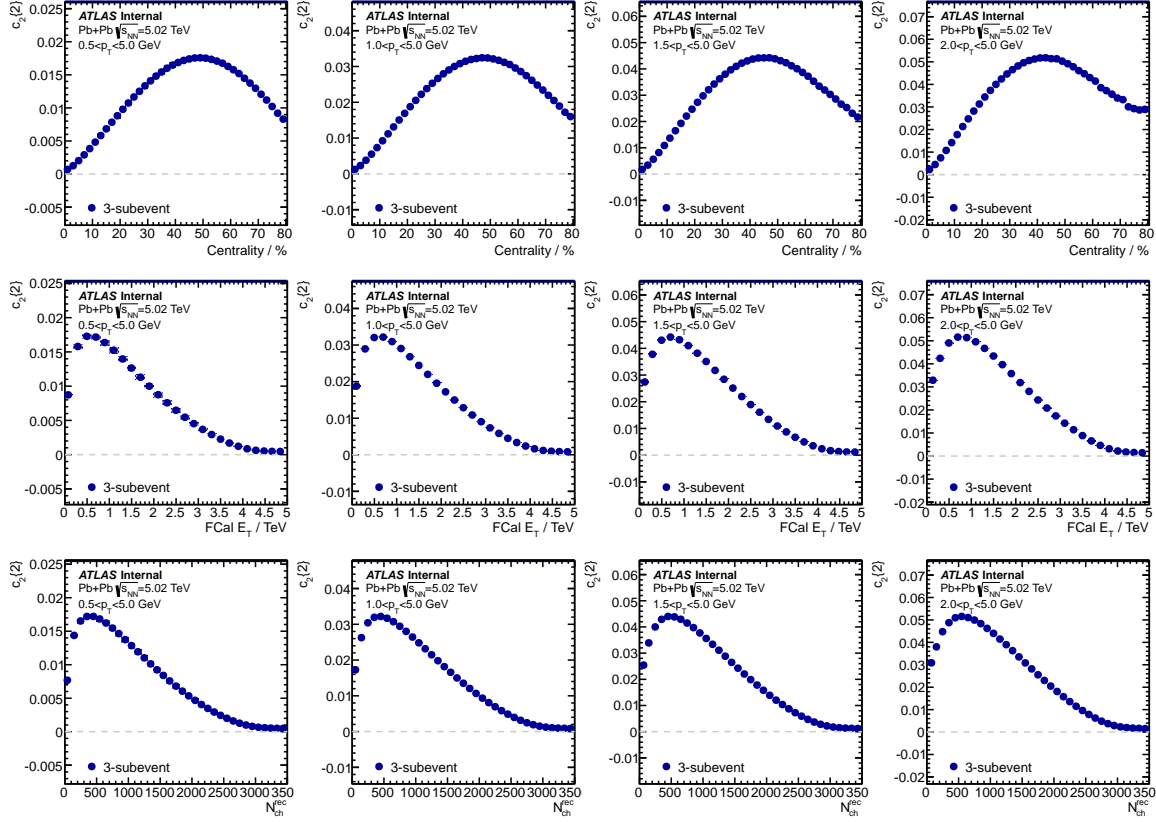


Figure 53: 2-particle cumulant $c_2\{2\}$ calculated with different p_T ranges (columns) and different event class definitions (rows).

Fig. 53 shows the 2-particle cumulant $c_2\{2\}$ calculated with different p_T ranges and different event class definitions. The centrality dependence of v_2 is same as other event-plane measurements: $c_2\{2\}$ is largest in mid-central and decreases towards central and peripheral. Previous measurements showed that v_2 as a function of p_T keeps increasing until p_T reaches 2 to 3 GeV, which is also reflected in this measurement of $c_2\{2\}$ with different p_T cuts: the magnitude of $c_2\{2\}$ keeps increasing as p_T grows. Similar behaviors are observed for other harmonics v_3 and v_4 , as shown in Fig. 54.

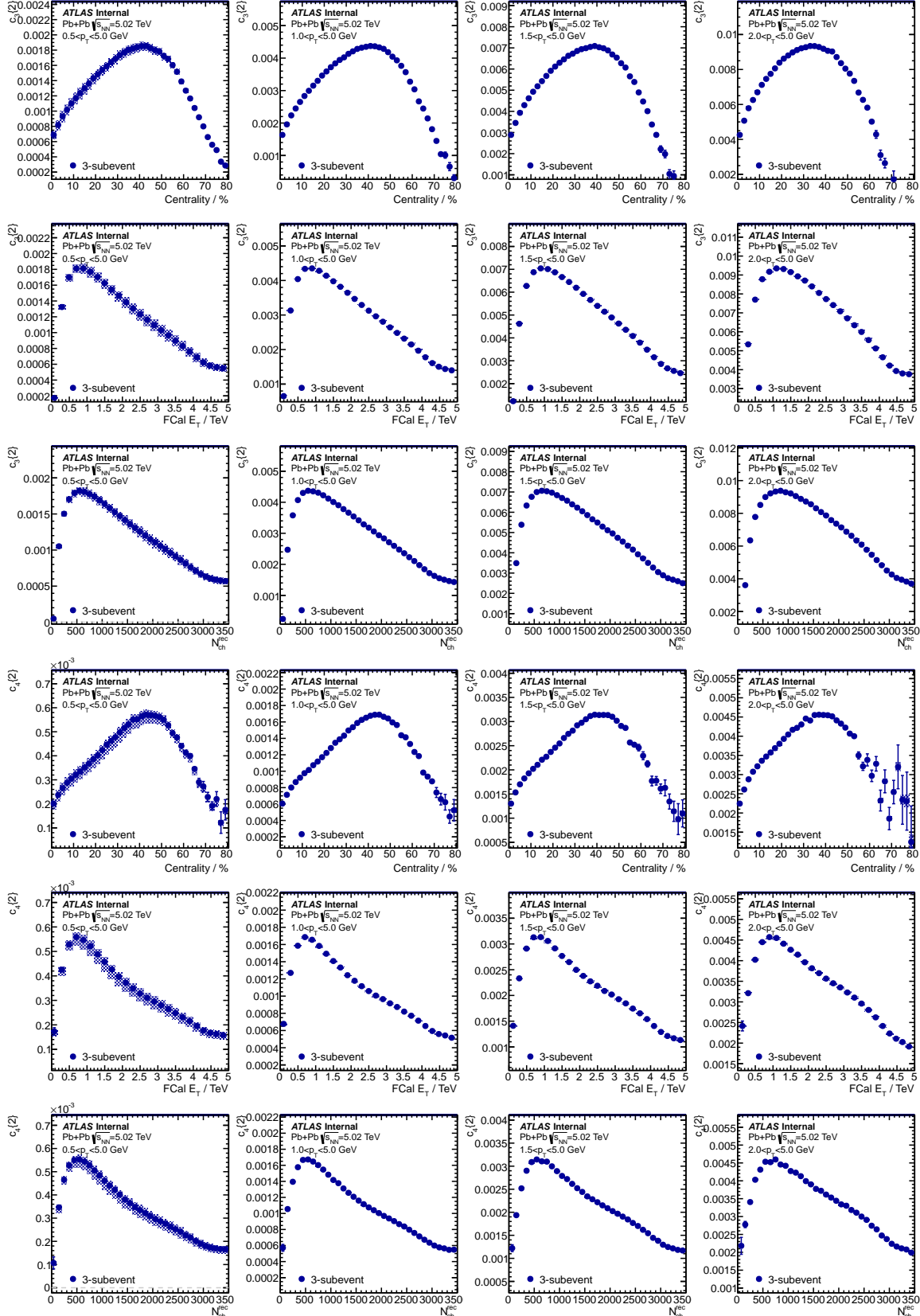


Figure 54: 2-particle cumulant $c_3\{2\}$ (top half) and $c_4\{2\}$ (bottom half) calculated with different p_T ranges (columns) and different event class definitions (rows).

1212 8.4 4-particle cumulant $c_n\{4\}$ and $nc_n\{4\}$

1213 In this section we present the 4-particle cumulant $c_n\{4\}$ for flow harmonics v_1 , v_2 , v_3 and v_4 . The
1214 normalized cumulants are also shown to better reflect the centrality dependence of flow fluctuations.

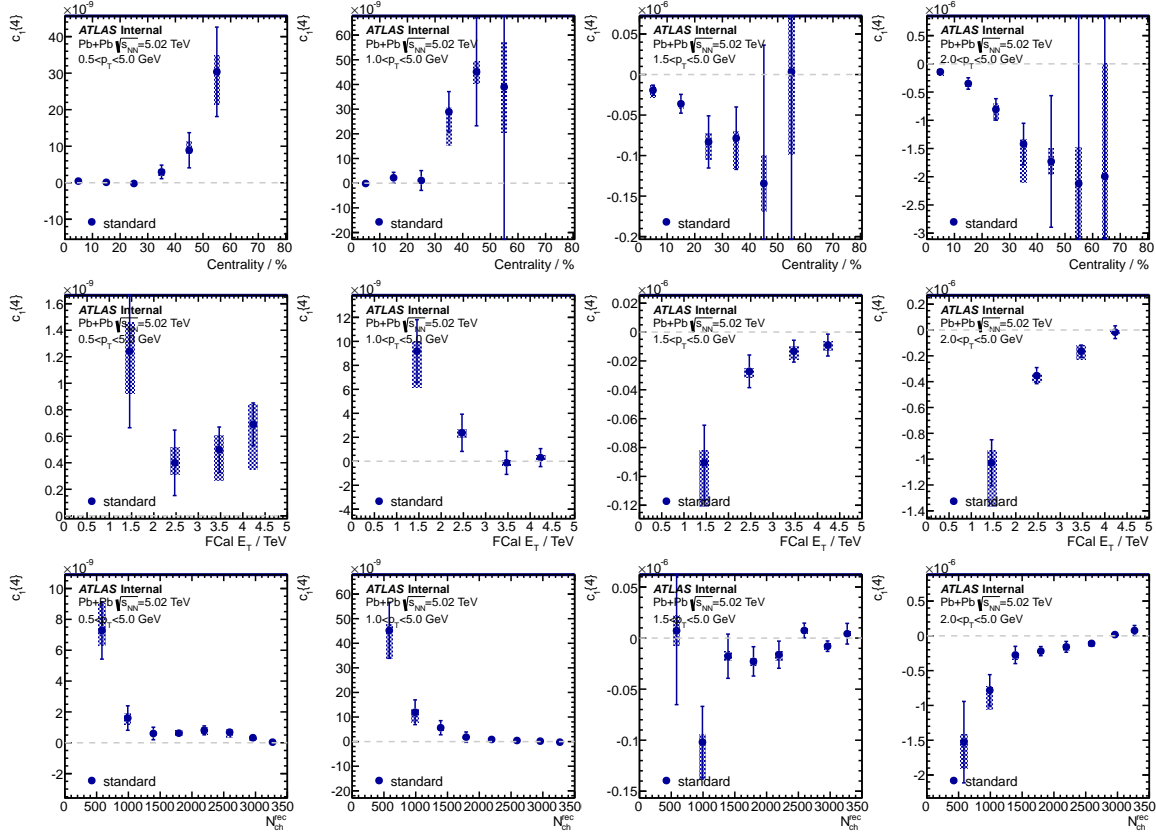


Figure 55: 4-particle cumulant $c_1\{4\}$ calculated with different p_T ranges (columns) and different event class definitions (rows).

1215 Fig. 55 shows the 4-particle cumulant $c_1\{4\}$ calculated with different p_T ranges and different event
1216 class definitions. When the minimum p_T cut is below 1.0 GeV, $c_1\{4\}$ is consistent with 0 within statistical
1217 uncertainties, except in the very peripheral region, where $c_1\{4\}$ becomes positive. The reason why
1218 $c_1\{4\}$ becomes positive is not clear at the moment. As the minimum p_T cut goes beyond 1.5 GeV,
1219 $c_1\{4\}$ is systematically below 0 in peripheral collisions. We know that $v_1\{2\}$ from 2-particle correlation
1220 (after global momentum conservation is removed) changes sign around $p_T = 1.0$ GeV, which explains
1221 why $c_1\{4\}$ is negative only with higher p_T cuts: when the p_T cut is lower, the negative and positive
1222 $v_1\{2\}$ compensates each other. Interestingly, 2-particle correlation measurement also shows that $v_1\{2\}$
1223 is weakly dependent of centrality, which is not a case for $c_1\{4\}$: its magnitude keeps decreasing towards
1224 peripheral collision. While the mean value of v_1 unchanged, this indicates that the fluctuation of v_1
1225 becomes highly non-Gaussian in peripheral collisions.

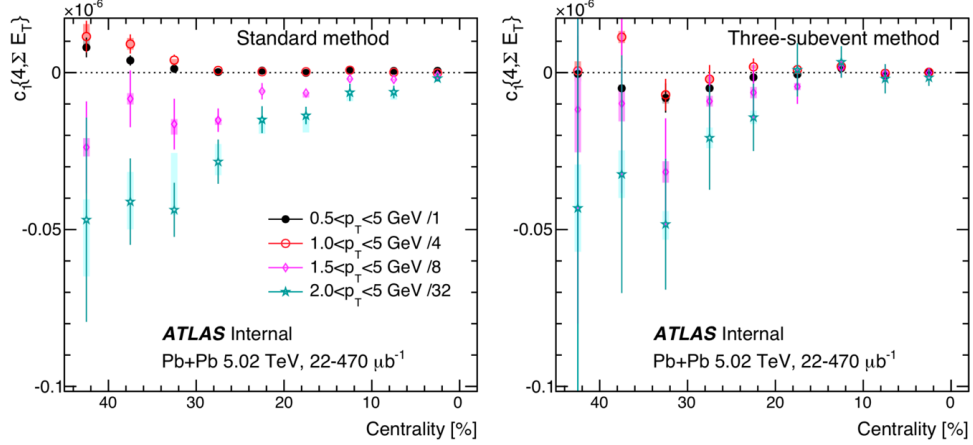


Figure 56: 4-particle cumulant $c_1\{4\}$ calculated using standard cumulant method (left) and 3-subevent method (right).

1226 To check whether negative $c_1\{4\}$ is caused by non-flow effects, measurement is repeated using 3-
 1227 subevent method, as previously shown in Fig. 56. In addition, $c_1\{4\}$ with high p_T cut is always negative
 1228 in peripheral, regardless of event class definitions (shown in the paper draft [24]). This further supports
 1229 our claim that this observation is due to genuine v_1 fluctuation, not other trivial effects.

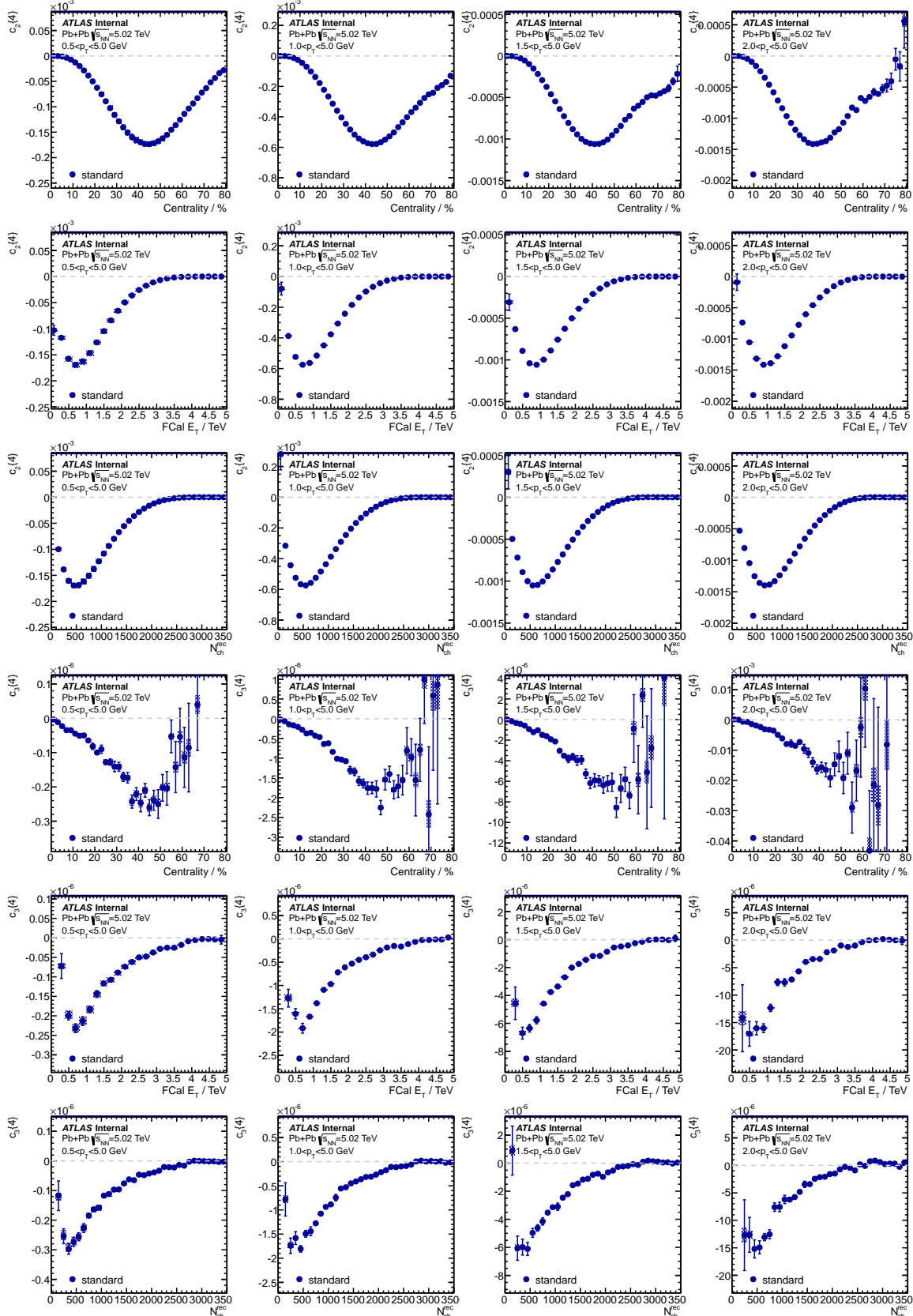


Figure 57: 4-particle cumulant $c_2\{4\}$ (top half) and $c_3\{4\}$ (bottom half) calculated with different p_T ranges (columns) and different event class definitions (rows).

Fig. 57 present 4-particle cumulant $c_2\{4\}$ and $c_3\{4\}$ calculated with different p_T ranges and different event class definitions. Both $c_2\{4\}$ and $c_3\{4\}$ follow similar centrality dependence: they start with small value, reach maximum around 40% centrality, then decrease towards peripheral. Unlike the 2-particle correlation measurements, where $c_2\{2\}$ does not reach 0 in most central collision. The reason why $c_2\{4\}$ and $c_3\{4\}$ are close to 0 is driven by the flow fluctuation. In central collision, due to a large number of sources, the flow fluctuations approach Gaussian, which results in a close-to-0 4-particle cumulant. We will come back to this feature when discussing the normalized cumulant results.

As minimum p_T cut increases from 0.5 to 2.0 GeV, the magnitudes of $c_2\{4\}$ and $c_3\{4\}$ increase rapidly. This p_T dependence is qualitatively consistent with observations from 2-particle correlation measurements, which indicates that the fluctuations of v_2 and v_3 are so close to Gaussian, that the 4-particle cumulants are driven by the mean value of flow. We will verify this point by universality check of flow fluctuations.

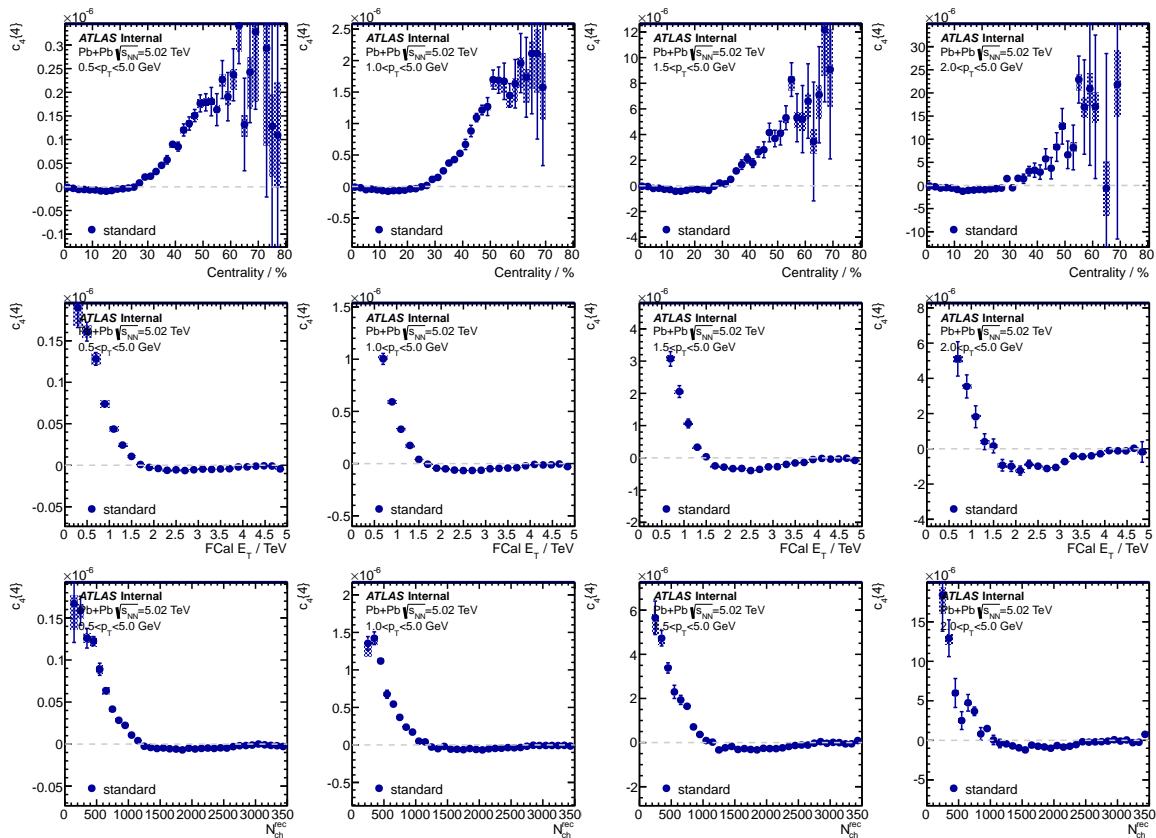


Figure 58: 4-particle cumulant $c_4\{4\}$ calculated with different p_T ranges (columns) and different event class definitions (rows).

$c_4\{4\}$ with different p_T ranges are summarized in Fig. 58. Like $c_2\{4\}$ and $c_3\{4\}$, $c_4\{4\}$ shows strong p_T dependence. It is also interesting to note that $c_4\{4\}$ is negative for centrality $< 25\%$, then it turns positive and keeps increasing towards peripheral. This behavior is consistent with the hydrodynamic prediction: negative $c_4\{4\}$ in central and mid-central is due to the linear component of v_4 , while in peripheral, the non-linear component from v_2^2 dominates over linear component:

$$v_4 = v_{4L} + k v_2^2 \quad (68)$$

and this non-linear component causes v_4 fluctuation to be non-Gaussian, which results in positive $c_4\{4\}$

₁₂₄₈ (note that 4-particle cumulant is ill-defined if it's positive). By checking different event class definitions,
₁₂₄₉ it's also clear that the balance between linear and non-linear is not due to centrality fluctuation.

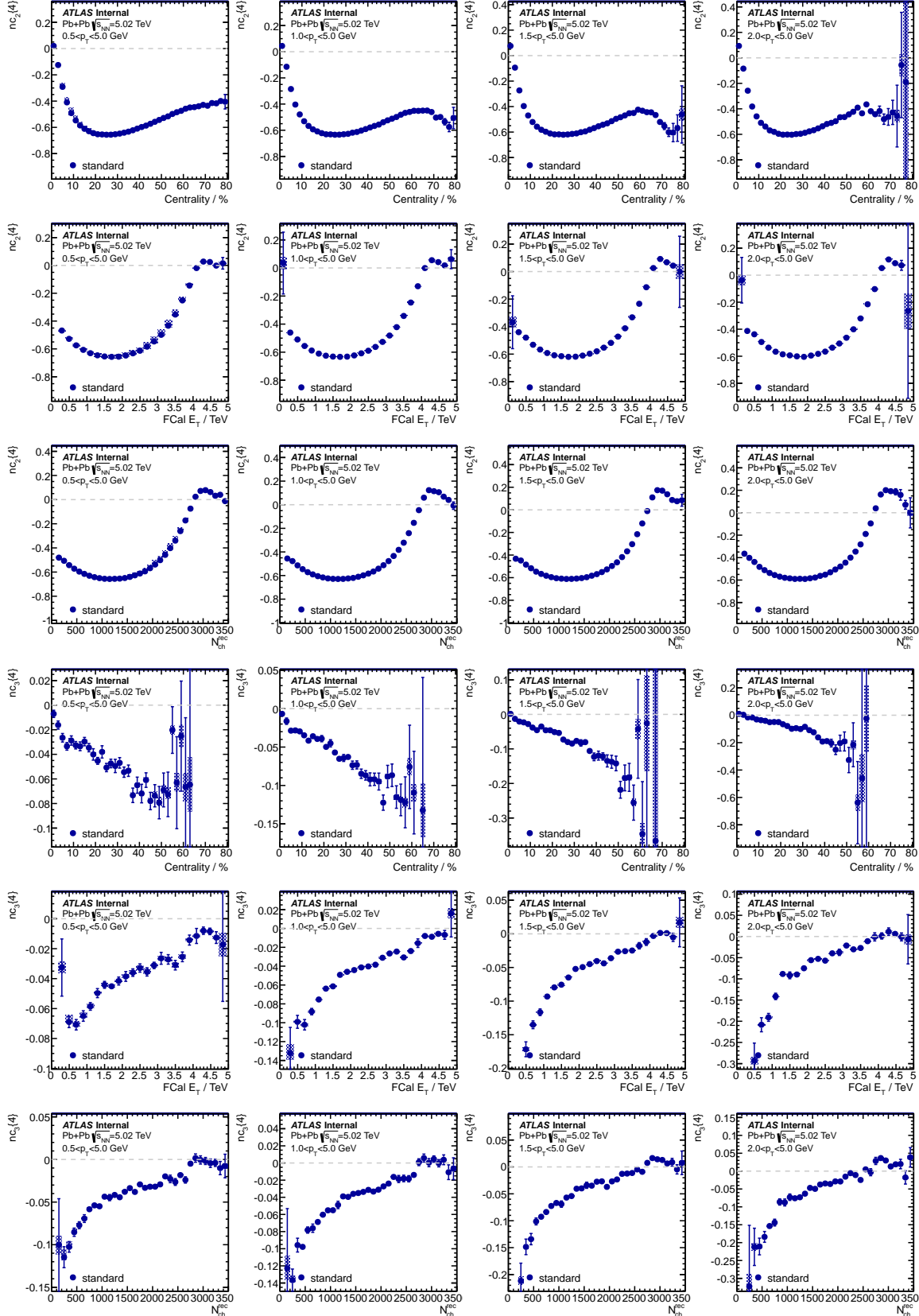


Figure 59: Normalized 4-particle cumulant $nc_2\{4\}$ and $nc_3\{4\}$ calculated with different p_T ranges (columns) and different event class definitions (rows).

In order to show the fluctuation nature of flow harmonics, Fig. 59 presents the similar results but with normalized cumulants $nc_2\{4\}$ and $nc_3\{4\}$. By dividing out 2-particle correlations from 4-particle cumulant, normalized cumulant focuses on the fluctuation itself. For v_2 , the fluctuation is largest in mid-centrality 20 – 30% and it decreases towards central and peripheral. In the ultra-central collision with centrality < 1%, $nc_2\{4\}$ exhibits rich sign change behavior: it first reaches 0 then becomes positive, in the most-central collisions, it drops back to 0. This behavior can be explained with centrality fluctuation, which we will dive into in details in the next section. For v_3 , since there is no average geometry from the initial stage, the fluctuation nature is very different from v_2 : magnitude of $\hat{3}\{4\}$ keeps increasing towards peripheral. This is expected because the number of sources drops quickly as collision moves to peripheral. Meanwhile, like v_2 , $nc_3\{4\}$ quickly approaches 0 in central collision, however, in most cases, it does not change sign as $nc_2\{4\}$, except for the N_{ch}^{rec} binned cases with very high p_T cuts. Finally, it is also noted that the p_T dependence for normalized cumulant is much weaker than cumulant, indicating that the flow fluctuation has a weak p_T dependence.

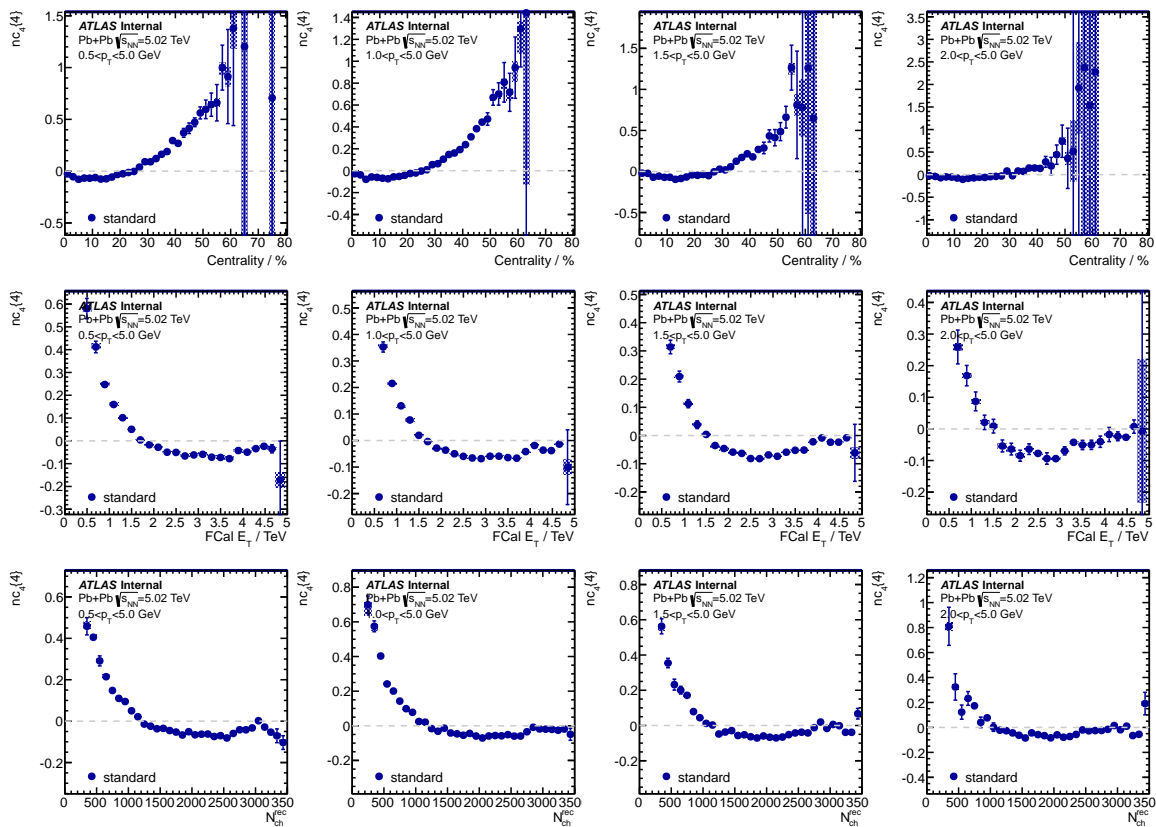


Figure 60: Normalized 4-particle cumulant $nc_4\{4\}$ calculated with different p_T ranges (columns) and different event class definitions (rows).

Fig. 60 shows the normalized 4-particle cumulant $nc_4\{4\}$, where the negative trend in central and mid-central is more obvious than without normalization. This is actually the advantage of normalizing cumulant: fluctuation behaviors can be easily spotted without zooming in.

1266 8.5 4-particle cumulant in ultra-central collisions

Follow the discussions in previous sections, magnitudes of $c_2\{4\}$ and $c_3\{4\}$ approach 0 towards central collisions, due to the increase of the number of sources. In Run 2 5.02 TeV Pb+Pb, ultra-central collision

triggers are applied to enhance the statistics for events with centrality < 1% (See Section. 3). With abundant statistics seeded by the UCC triggers, it provides a great opportunity to study the cumulant in ultra-central collisions. In this section, we are plotting $c_2\{4\}$, which has the largest signal, as function of FCal E_T instead of centrality. It worth mentioning that the event class is also defined with FCal E_T , with bin width = 20 GeV.

Fig. 63 presents the $c_2\{4\}$ in ultra-central Pb+Pb collisions, calculated with both cumulant methods. $c_2\{4\}$ from 3-subevent is systematically lower, even though within statistical uncertainties. This is because in large systems, the non-flow contributions are already largely suppressed with 4-particle cumulants. For lower p_T range $0.5 < p_T < 5.0$ GeV (left plot), $c_2\{4\}$ is negative for FCal $E_T < 4.1$ TeV, which picks up the tail of $c_2\{4\}$ as a function of centrality (Fig. 57). As FCal E_T increases, $c_2\{4\}$ changes the sign at $E_T = 4.2$ TeV and stays positive for $E_T < 4.6$ TeV. For $E_T > 4.6$ TeV, $c_2\{4\}$ is back to 0 again. The positive sign of $c_2\{4\}$ is very interesting, since with increasing number of sources, the v_2 fluctuation should approach Gaussian, which results in $c_2\{4\} = 0$. However, as shown in this figure, this is actually not the case: $c_2\{4\}$ can be positive in ultra-central collision, with more than 3-sigma statistical significance. For the higher p_T range $1.8 < p_T < 5.0$ GeV, trends are similar as lower p_T range, but the magnitude of positive $c_2\{4\}$ becomes larger with p_T .

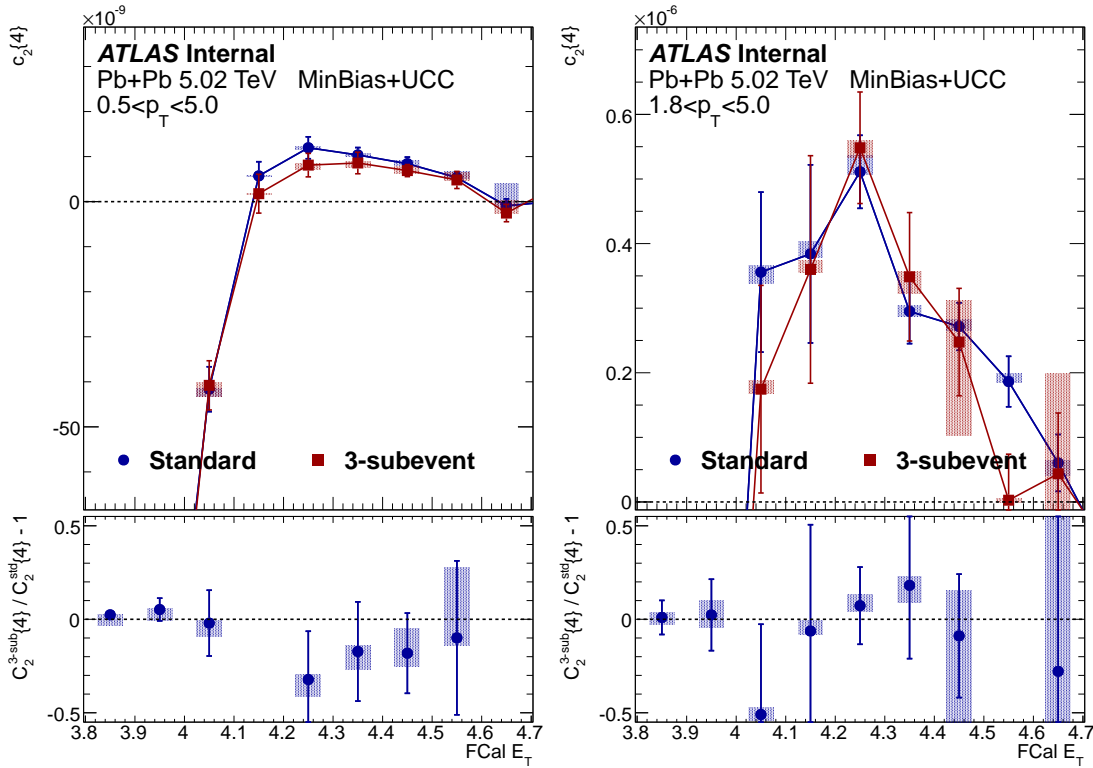


Figure 61: $c_2\{4\}$ in 5.02 TeV ultra-central Pb+Pb, calculated with different cumulant methods. Event class is defined by FCal E_T . Left panel is for the lower p_T range and right panel is for the higher p_T range.

To directly show the p_T dependence of $c_2\{4\}$ in ultra-central collisions, Fig. 62 presents the $c_2\{4\}$ calculated in different p_T ranges, with standard cumulant method. It is noticed that $c_2\{4\}$ from all the p_T ranges follow similar trend: $c_2\{4\}$ starts with negative, turns positive around $E_T = 4.1$ TeV, and drops back to 0 in most central collisions. The maximum magnitude of $c_2\{4\}$ increases quickly as minimum p_T cut increases.

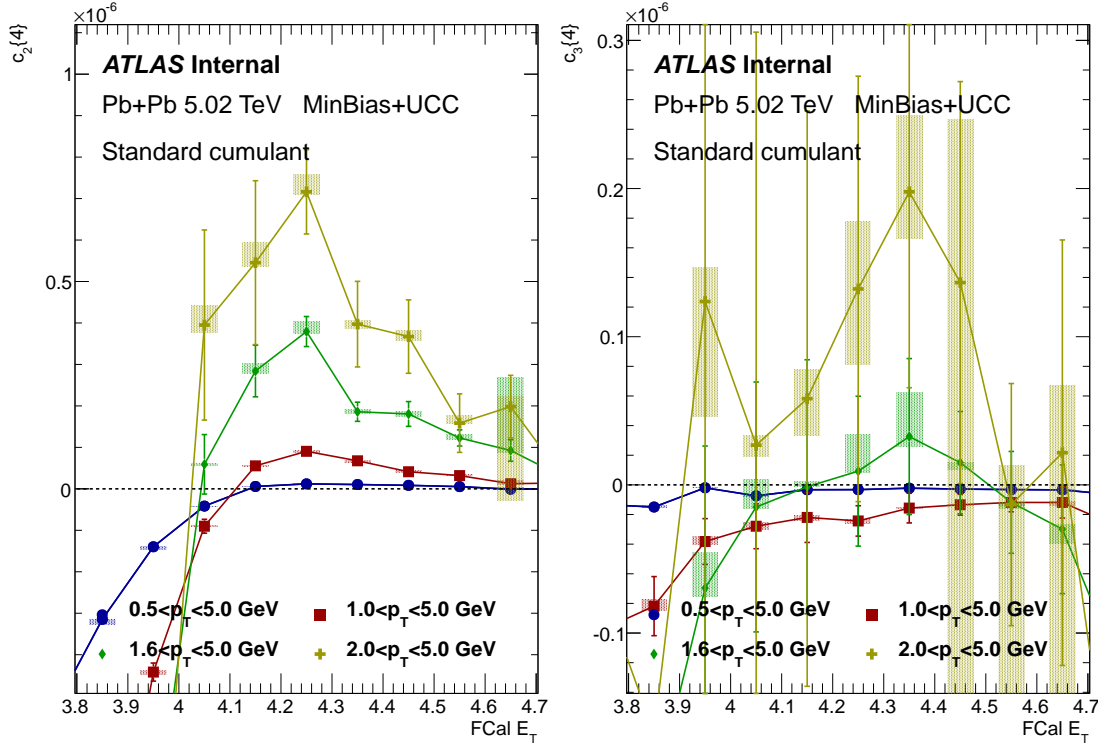


Figure 62: $c_2\{4\}$ and $c_3\{4\}$ in 5.02 TeV Pb+Pb, with event class binned with FCal E_T . Results are calculated in different p_T ranges, with standard cumulant method.

1290 The definition of event class is important in cumulant measurement. Since cumulant measures the
 1291 underlying v_n probability distribution within a bunch of similar events, by changing the event class def-
 1292 inition, the magnitude, even the sign of cumulant could also change. In order to check whether the
 1293 positive $c_2\{4\}$ observed in ultra-central collision is due to such binning effects, in this section, a different
 1294 event class definition is applied: events are grouped according to their N_{ch}^{rec} , with $0.5 < p_T < 5.0$ GeV. To
 1295 properly compare with FCal E_T binning, the final results are mapped to the mean value of FCal E_T for
 1296 each N_{ch}^{rec} bin.

1297 The result is shown in Fig. 63, with particles from lower and higher p_T ranges separately. $c_2\{4\}$ from
 1298 3-subevent is systematically lower, even though still within statistical uncertainties. Compared with FCal
 1299 E_T binning, similar trend is observed: $c_2\{4\}$ starts with negative value, becomes positive, and drops back
 1300 to 0 in the most central collisions. However, there are two major differences between the two event class
 1301 definitions:

- 1302 • the maximum magnitude depends on event class definition;
 1303 • the point where $c_2\{4\}$ changes sign depends on event class definition;

1304 which is not surprising since the $c_2\{4\}$ signal in ultra-central collision is small, and slight changes in
 1305 event class definition will modify the v_2 fluctuation, which leads to the observations mentioned above.
 1306 However, it is interesting that even though the magnitude of maximum $c_2\{4\}$ changes a lot, the trends of
 1307 $c_2\{4\}$ from two event class definitions are still similar.

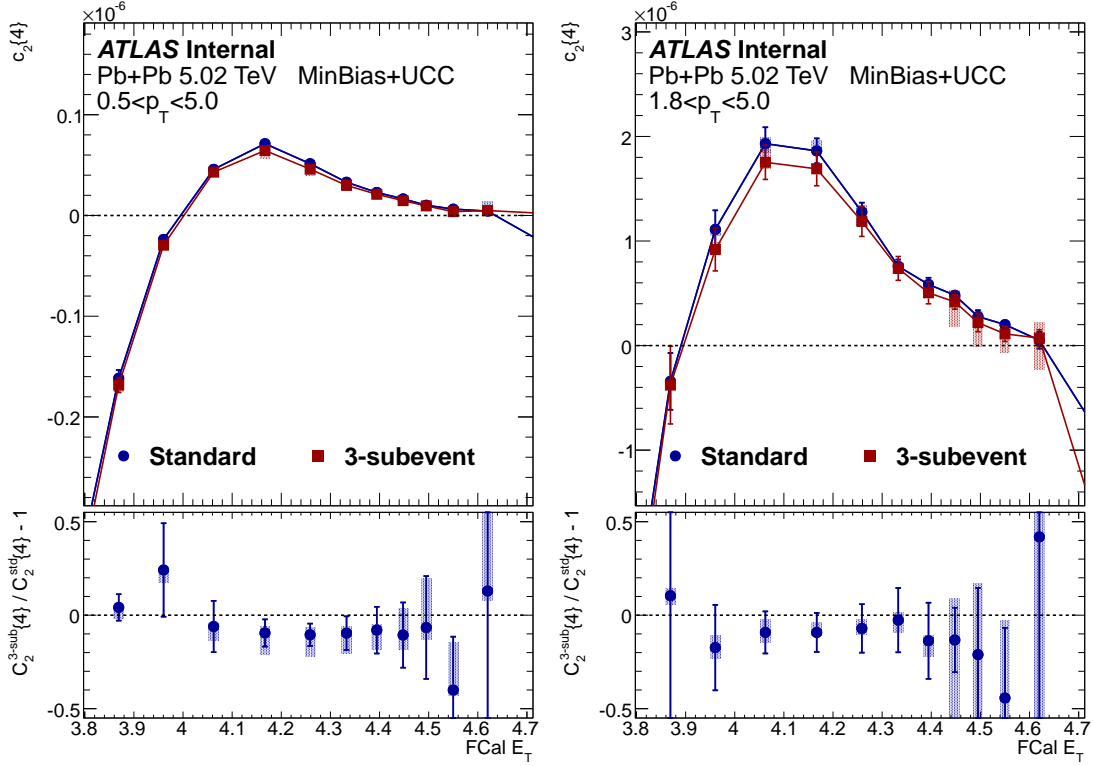


Figure 63: $c_2\{4\}$ in 5.02 TeV ultra-central Pb+Pb, calculated with different cumulant methods. Event class is defined by N_{ch} . Left panel is for the lower p_T range and right panel is for the higher p_T range.

1308 To directly show the p_T dependence of $c_2\{4\}$ in ultra-central collisions, Fig. 64 presents the $c_2\{4\}$
 1309 calculated in different p_T ranges, with standard cumulant method. It is observed that $c_2\{4\}$ from all the
 1310 p_T ranges follow similar trend: $c_2\{4\}$ starts with negative, turns positive, and drops back to 0 in most-
 1311 central collisions. The maximum magnitude of $c_2\{4\}$ increases quickly as minimum p_T cut increases.

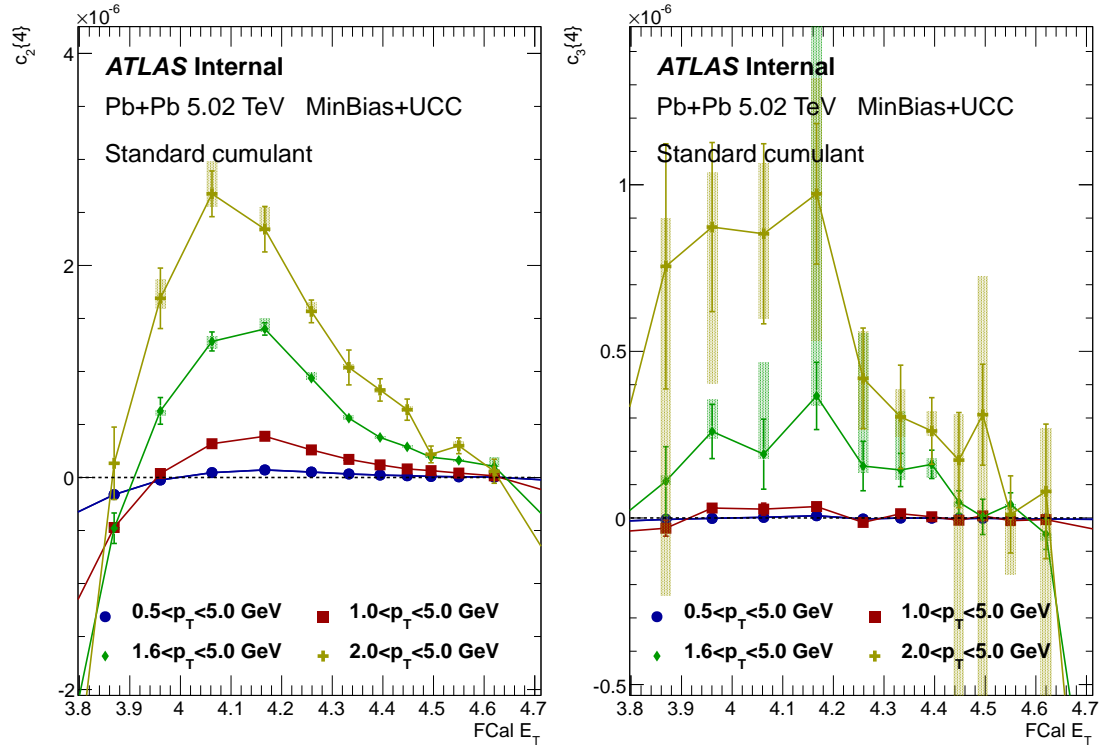


Figure 64: $c_2\{4\}$ and $c_3\{4\}$ in 5.02 TeV Pb+Pb, with event class binned with N_{ch} . Results are calculated in different p_T ranges, with standard cumulant method.

1312 8.6 4-particle cumulant in 2.76 and 5.02 TeV

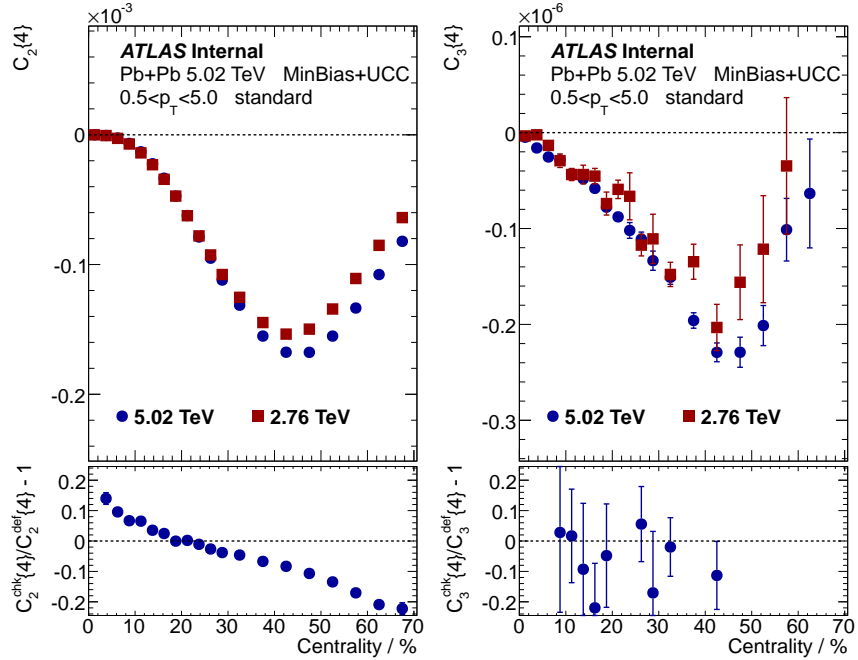


Figure 65: $c_2\{4\}$ and $c_3\{4\}$ at 2.76 and 5.02 TeV Pb+Pb collision, calculated with standard cumulant. The bottom panels show the relative difference between 2.76 and 5.02 TeV Pb+Pb.

1313 Judging from previous measurements of 2-particle correlation that discussed in Sec. 2, we expect the
 1314 4-particle cumulant $c_n\{4\}$ is also weakly energy dependent. Fig. 65 shows the comparison of $c_2\{4\}$
 1315 and $c_3\{4\}$ between 2.76 and 5.02 TeV Pb+Pb collision, as a function of centrality. The cumulants are
 1316 calculated using standard cumulant method with $0.5 < p_T < 5.0$ GeV. For $c_2\{4\}$, between 0% and 20%
 1317 centrality, the magnitude of $c_2\{4\}$ in 2.76 TeV Pb+Pb is larger than 5.02 TeV. As collision goes to
 1318 peripheral, the magnitude of $c_2\{4\}$ in 2.76 TeV Pb+Pb becomes smaller than 5.02 TeV. The maximum
 1319 relative difference reaches about 20% at most peripheral, which is around 5% level if converted to $v_2\{4\}$.
 1320 While for $c_3\{4\}$, the trend is simpler between two energies: magnitude of $c_3\{4\}$ at 2.76 TeV is always
 1321 smaller than 5.02 TeV. The maximum relative difference is still around 5% on the $v_3\{4\}$ level. In
 1322 summary, the energy dependence of $c_3\{4\}$ and $c_4\{4\}$ is weak between 2.76 and 5.02 TeV as expected.
 1323 Note that it is possible that such weak energy dependence is due to the small mean p_T difference, as well
 1324 as the different η distributions, between the two energies.

1325 8.7 6-particle cumulant $c_n\{6\}$ and $nc_n\{6\}$

1326 Enhancement of statistics in Run 2 makes it feasible to calculate up to 6-particle cumulant with high
 1327 precision. In this section, we will show the 6-particle cumulant results for v_2 and v_3 .

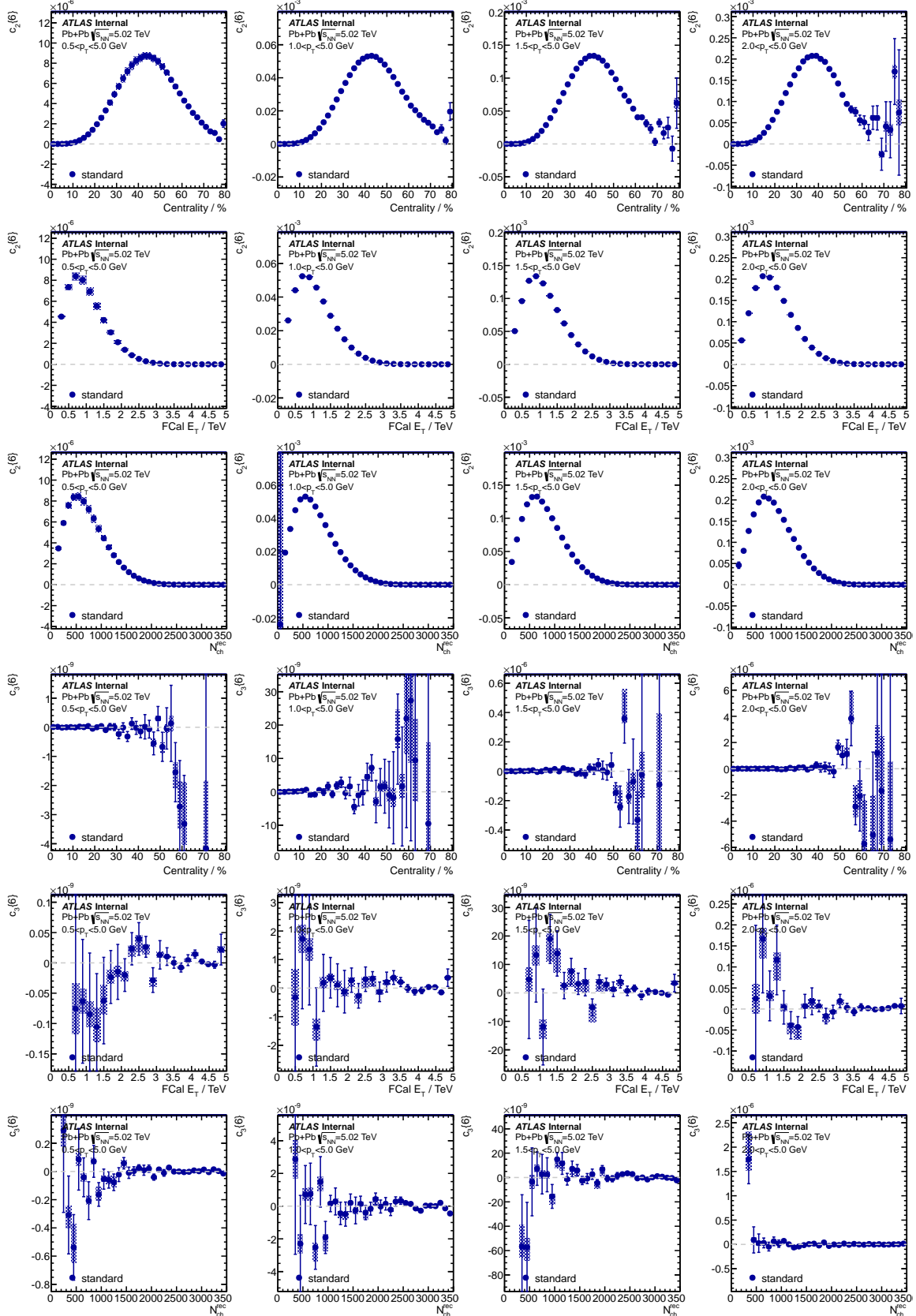


Figure 66: 6-particle cumulant $c_2\{6\}$ (top half) and $c_3\{6\}$ (bottom half) calculated with different p_T ranges (columns) and different event class definitions (rows).

Fig. 66 shows $c_2\{6\}$ and $c_3\{6\}$ calculated with different p_T ranges and different event class definitions. Unlike 4-particle cumulant, to have a well-defined $v_n\{6\}$, 6-particle cumulant needs to be larger than 0. For v_2 , the centrality dependence of $c_2\{6\}$ follows the similar trend as $c_2\{4\}$: its magnitude reaches maximum in mid-centrality and drops to 0 in central collisions. Unlike the Gaussian fluctuation scenario, since $2k$ -particle cumulant is proportional to the $2k$ th power of v_n , this explains why the $c_2\{6\}$ with higher p_T cuts yields larger magnitude. The results for the third harmonic $c_3\{6\}$ is also shown. Its magnitude is much smaller compared with $c_2\{6\}$. Unfortunately, since the magnitude of v_3 is significantly smaller than v_2 , with current statistics, we could not measure significant non-zero $c_3\{6\}$: the results are consistent with within statistical uncertainties.

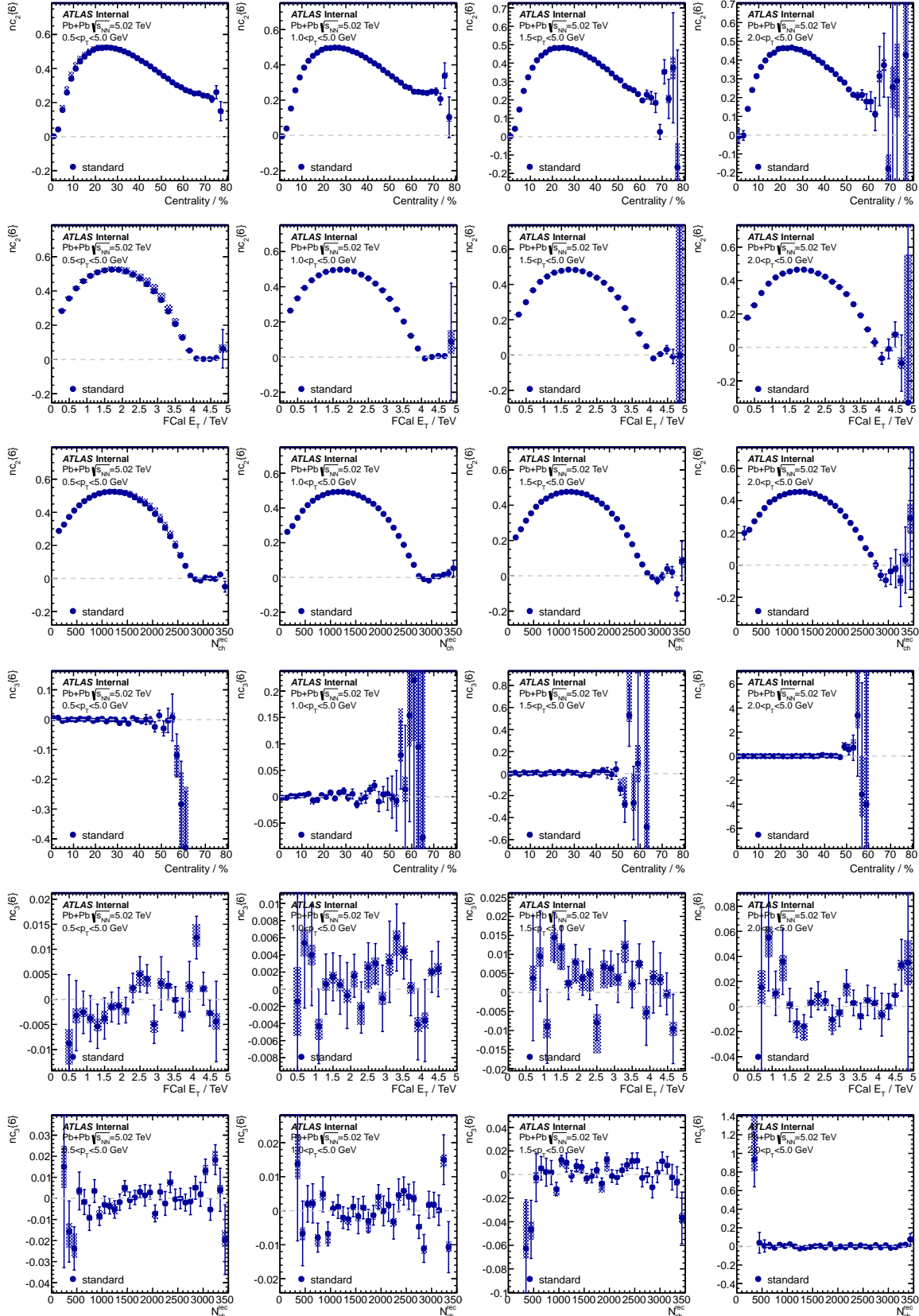


Figure 67: Normalized 6-particle cumulant $nc_2\{6\}$ (top half) and $nc_3\{6\}$ (bottom half) calculated with different p_T ranges (columns) and different event class definitions (rows).

1337 The centrality and p_T dependence of 6-particle cumulant mostly originates from the centrality and
1338 p_T dependence of \bar{v}_n . To disentangle the flow fluctuation from the mean value of flow, we have defined
1339 the normalized cumulant $nc_n\{6\}$, by dividing the 6-particle cumulant by 2-particle cumulant. The results
1340 are shown in Fig. 67. For the $nc_2\{6\}$ with $1.5 < p_T < 5.0$ GeV, we observed a hint of double sign change
1341 in the ultra-central collisions, which is related to the single sign change of $nc_2\{4\}$. For $nc_3\{6\}$, results
1342 from all p_T ranges are consistent with 0: similar conclusion as $c_3\{6\}$.

1343 8.8 Universality check of flow fluctuation models

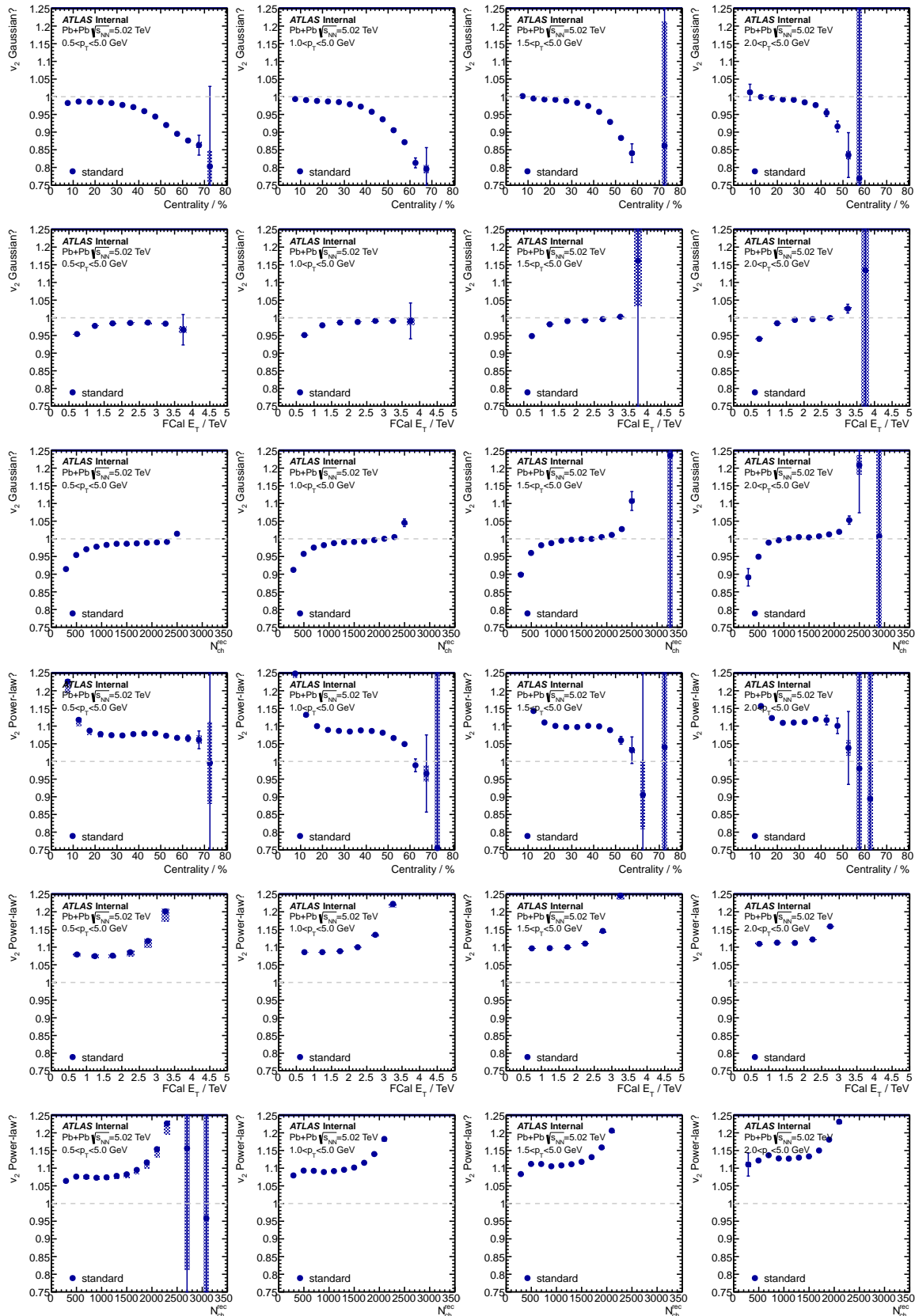


Figure 68: Check of flow fluctuation models, Gaussian (top half) or power-law (bottom half) calculated with different p_T ranges (columns) and different event class definitions (rows).

¹³⁴⁴ To quantify the flow fluctuation in Pb+Pb, in Fig. 68, we show the Gaussian universality test of v_2
¹³⁴⁵ fluctuation. As discussed in the methodology section, if the underlying flow fluctuation is Gaussian, the
¹³⁴⁶ value should be 1. In other words, any deviation from 1 will indicate a non-Gaussian fluctuation. In
¹³⁴⁷ Pb+Pb, the Gaussian check is consistent with 1 in central, very close to 1 in mid-central, and begins
¹³⁴⁸ to deviate from 1 towards peripheral collisions. This trend is qualitatively consistent with the previous
¹³⁴⁹ ATLAS $p(v_n)$ measurement, which used unfolding technique to directly measure the event-by-event v_n
¹³⁵⁰ distribution. The universality check for v_3 are consistent with 0, due to very large statistical uncertainties.
¹³⁵¹ In addition to Gaussian flow fluctuation, another competing fluctuation model follows the power-law
¹³⁵² distribution, which is shown in the same figure. Compared with the Gaussian check, the power-law
¹³⁵³ check is further away from 1, meaning that the underlying flow fluctuation is closer to Gaussian than
¹³⁵⁴ power-law. For v_3 , there are not enough statistics to quantify whether the fluctuation follows power-law.

1355 8.9 Symmetric cumulant $sc_{n,m}\{4\}$ and $nsc_{n,m}\{4\}$

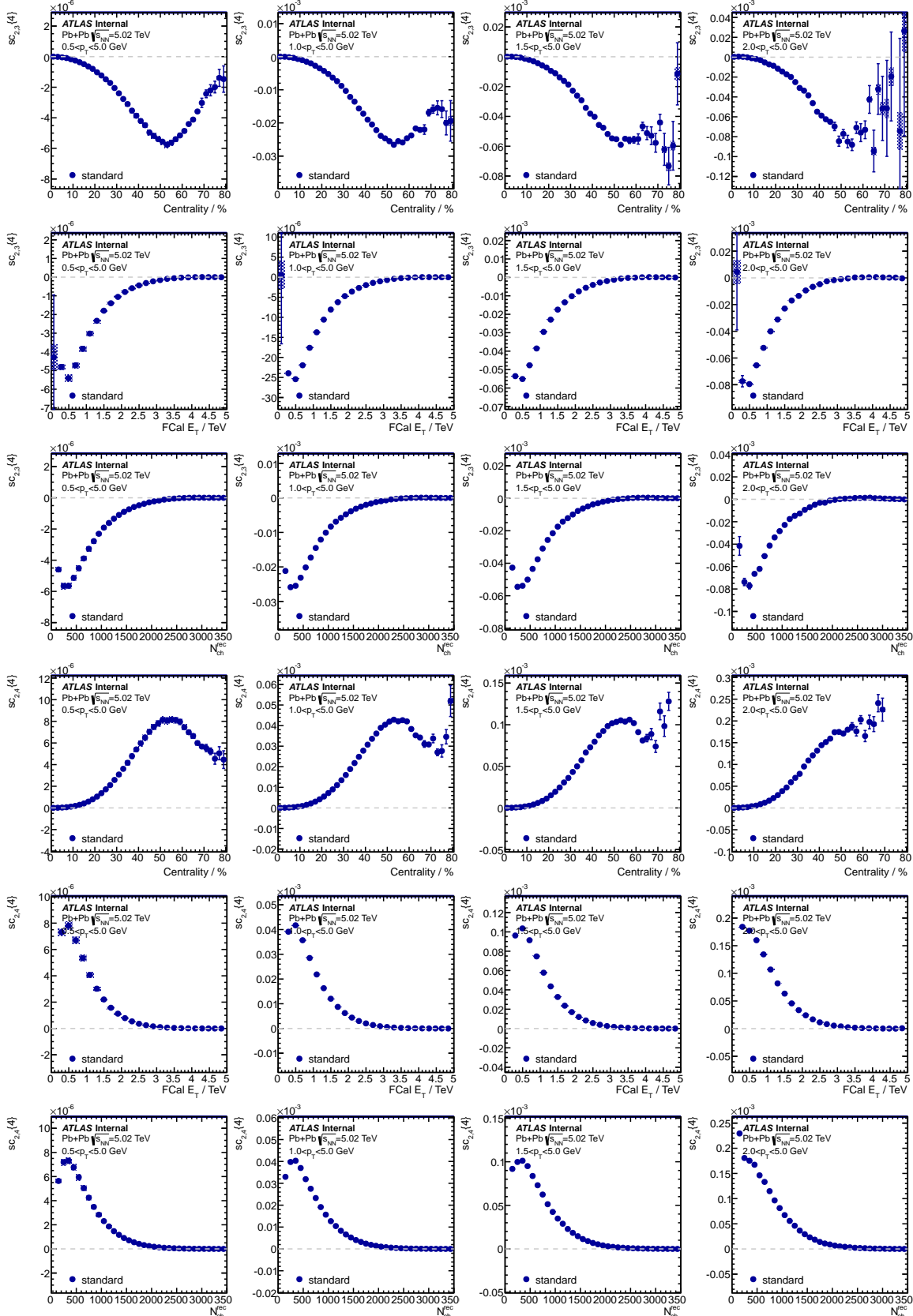


Figure 69: Symmetric cumulant $sc_{2,3}\{4\}$ (top half) and $sc_{2,4}\{4\}$ (bottom half) calculated with different p_T ranges (columns) and different event class definitions (rows).

1356 To unveil the correlation and fluctuation between flow harmonics v_n and v_m , Fig. 69 shows the symmetric
 1357 cumulant $sc_{2,3}\{4\}$ and $sc_{2,4}\{4\}$ calculated with different p_T ranges and different event class definitions.
 1358 $sc_{2,3}\{4\}$ measures the correlation between v_2 and v_3 , a negative value indicates that the correlation be-
 1359 tween v_2 and v_3 are anti-correlated. This is not hard to understand since an enhancement of elliptic flow
 1360 will suppress the leading odd harmonic v_3 . The centrality dependence of $sc_{2,3}\{4\}$ basically follows the
 1361 centrality dependence of v_2 and v_3 , and $sc_{2,3}\{4\}$ has a strong p_T dependence, all of which will be weak-
 1362 ened once we calculate the normalized symmetric cumulant. For $sc_{2,4}\{4\}$, the value is larger than 0,
 1363 meaning that the correlation between v_2 and v_4 are positively correlated. Part of the cause is due to the
 1364 similar geometric features of elliptic and quadratic flow, more importantly, the other cause is due to the
 1365 non-linear component of v_2^2 in v_4 , which is covered in the discussion of sign change of $c_4\{4\}$.

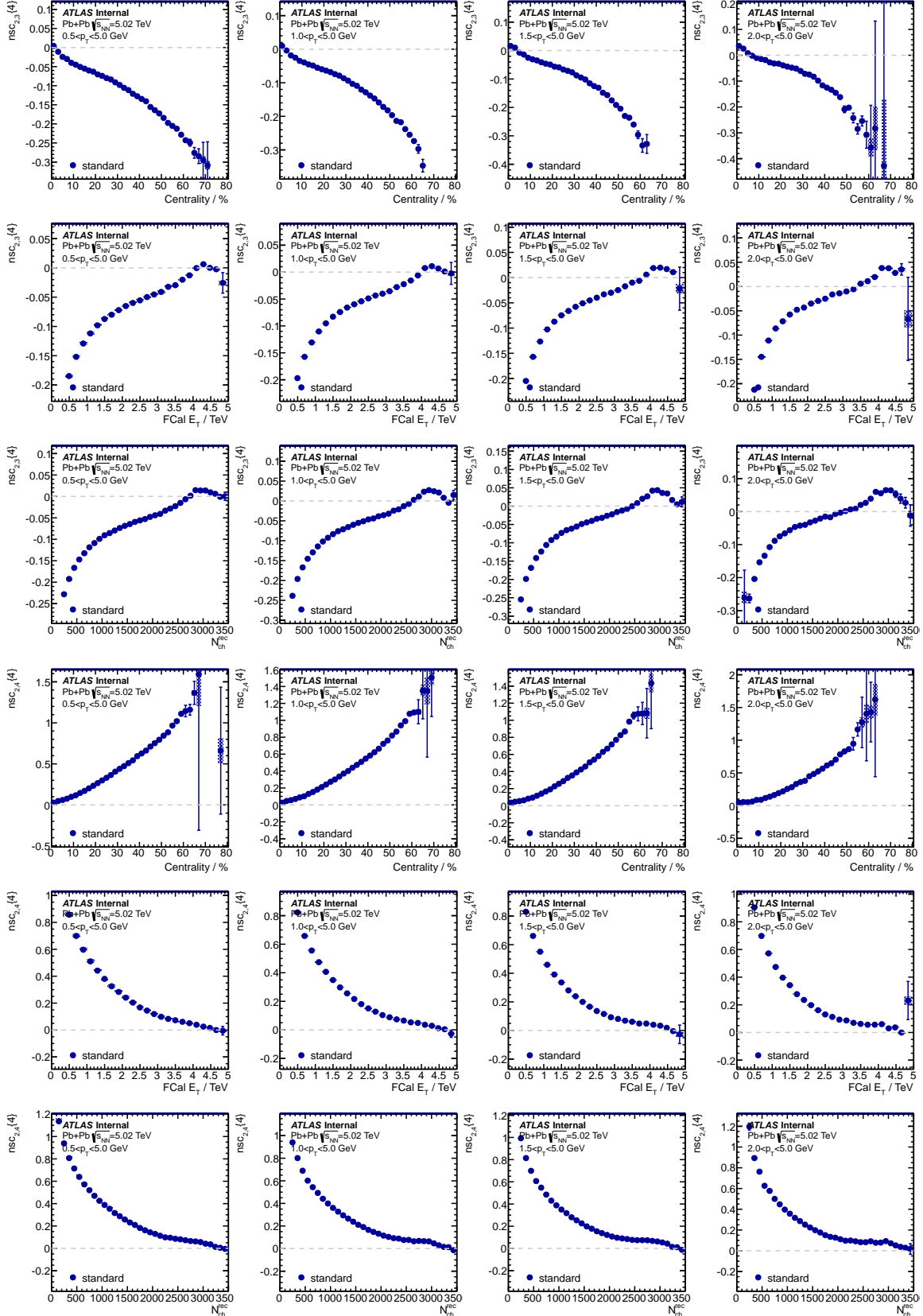


Figure 70: Normalized symmetric cumulant $nsc_{2,3}\{4\}$ (top half) and $nsc_{2,4}\{4\}$ (bottom half) calculated with different p_T ranges (columns) and different event class definitions (rows).

1366 To take out the centrality and p_T dependence of symmetric cumulant, normalized symmetric cumu-
 1367 lants $nsc_{n,m}\{4\}$ are calculated, and the results are summarized in Fig. 70. For $nsc_{2,3}\{4\}$, the centrality
 1368 and p_T dependence are very different from $sc_{2,3}\{4\}$: the magnitude keeps increasing as collision moves
 1369 towards peripheral, and the p_T dependence is much weaker in the normalized case. Interestingly, similar
 1370 sign change behaviour is also observed in central collision: $nsc_{2,3}\{4\}$ becomes positive for centrality
 1371 $< 1\%$, especially when the events are binned according to N_{ch}^{rec} . This sign change behavior can be ex-
 1372 plained in the similar way as the sign change of $c_2\{4\}$: centrality fluctuation changes the flow fluctuation,
 1373 and results in positive correlation between v_2 and v_3 . For $nsc_{2,4}\{4\}$, the centrality and p_T dependence are
 1374 also very different from $nsc_{2,3}\{4\}$, but no hint of sign change is observed. This could be due to the fact
 1375 that $v_2\{2\}$ never drops to 0, even in central collisions, which makes $nsc_{2,4}\{4\}$ positive. However, a hint
 1376 of kink is observed in ultra-central collision, indicating that the centrality fluctuation still plays a role.

1377 8.10 Asymmetric cumulant $ac_{n,n+m}\{3\}$ and $nac_{n,n+m}\{3\}$

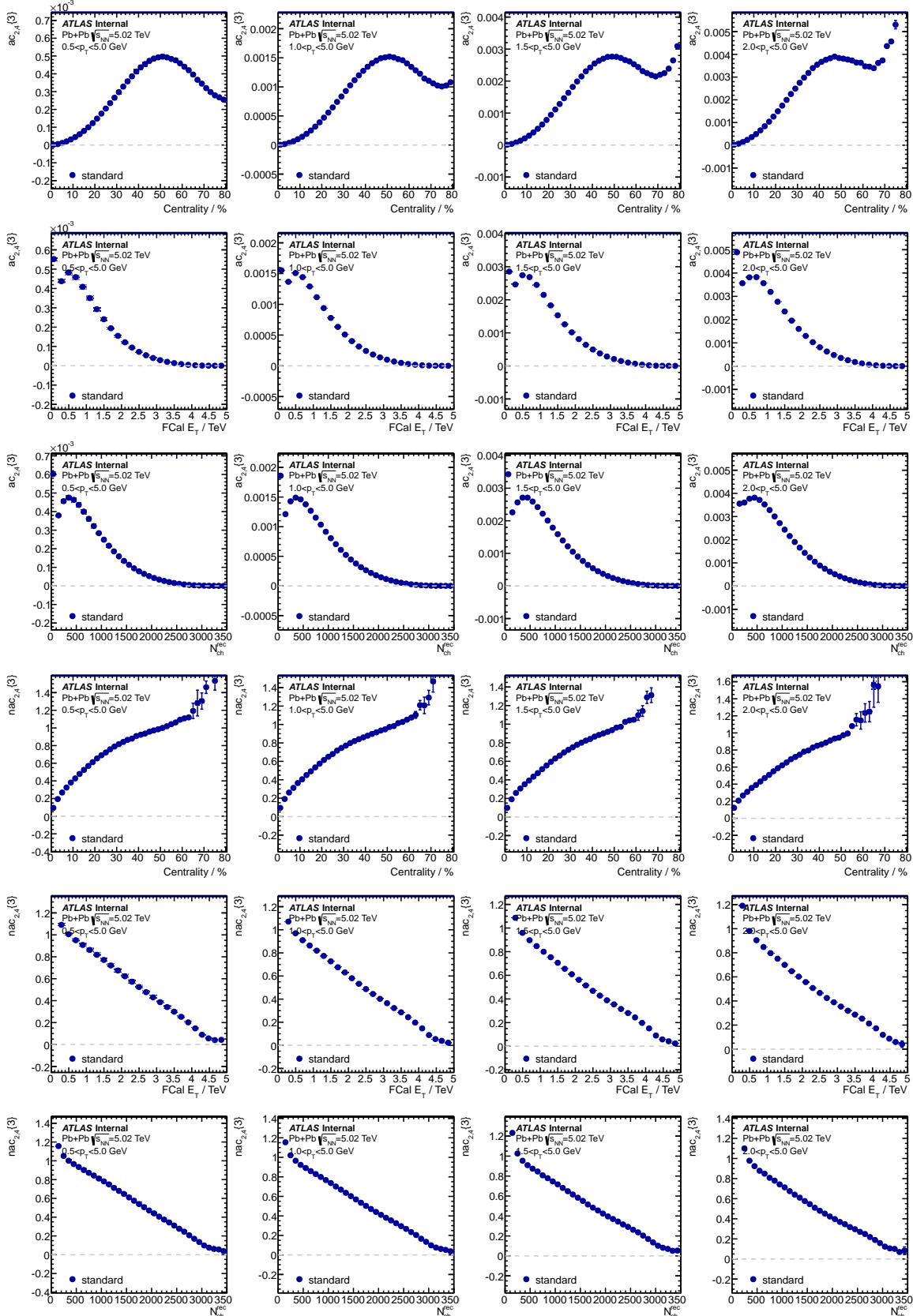


Figure 71: Asymmetric cumulant $ac_{2,4}\{3\}$ (top half) and normalized asymmetric cumulant $nac_{2,4}\{3\}$ (bottom half) calculated with different p_T ranges (columns) and different event class definitions (rows).

1378 In the last part of this section we show the asymmetric cumulant $ac_{2,4}\{3\}$ results in Fig. 71. $ac_{2,4}\{3\}$
1379 measures the correlation among v_2 , v_2 and v_4 , which is similar to the event plane correlation that has
1380 been measured before. Like $sc_{2,4}\{4\}$, $ac_{2,4}\{3\}$ follows the similar centrality and p_T dependence, most
1381 of which is due to the centrality and p_T dependence of v_2 and v_4 . Note that the increase of magnitude in
1382 peripheral with high p_T is probably cause by the non-flow, as shown in the method comparison section.
1383 After the asymmetric cumulant is normalized, the centrality dependence becomes monotonic and the p_T
1384 dependence is much weaker.

1385 9 Selected plots for the paper

1386 This section listed the plots that will be included in the paper. All the discussions are already covered in
 1387 the results section. For the purpose of story telling, different panels are re-organized to be shown in the
 1388 same plot.

1389 9.1 2-particle cumulant $v_n\{2\}$ with $n = 2, 3, 4$

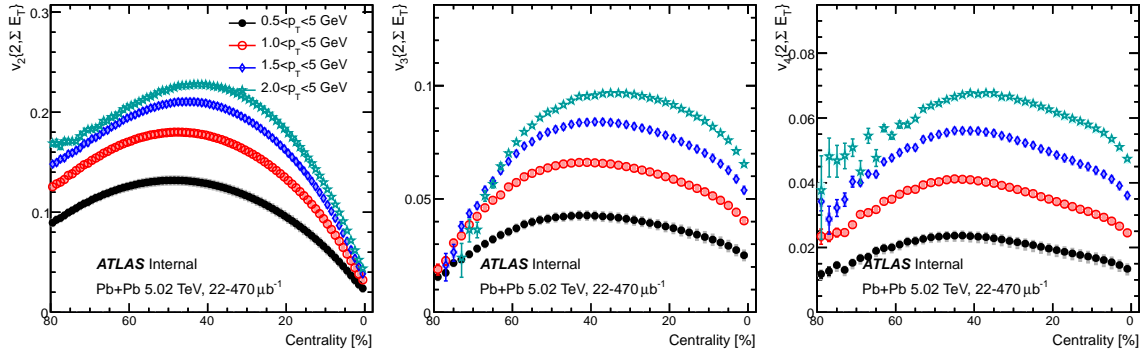


Figure 72: 2-particle flow cumulant as a function of centrality, calculated using standard method, with multiple p_T ranges.

1390 9.2 4-particle cumulant $nc_n\{4\}$ with $n = 2, 3, 4$

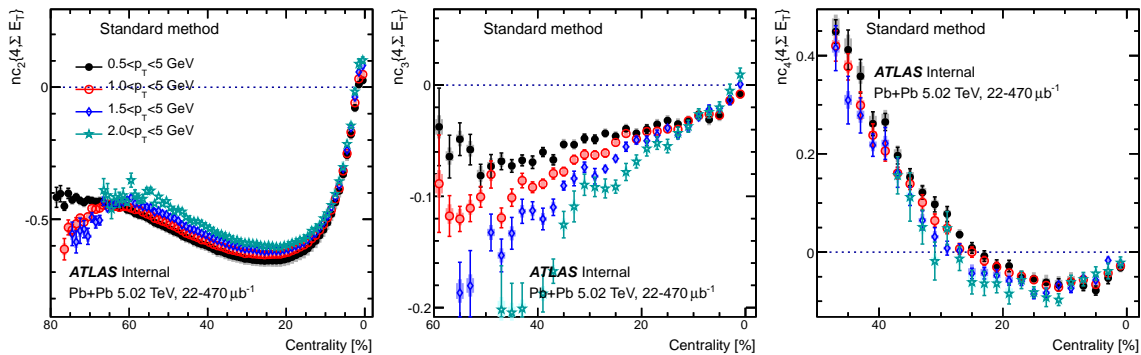


Figure 73: 4-particle normalized cumulant as a function of centrality, calculated using standard method, with multiple p_T ranges.

¹³⁹¹ **9.3 6-particle cumulant $nc_n\{6\}$ with $n = 2, 3, 4$**

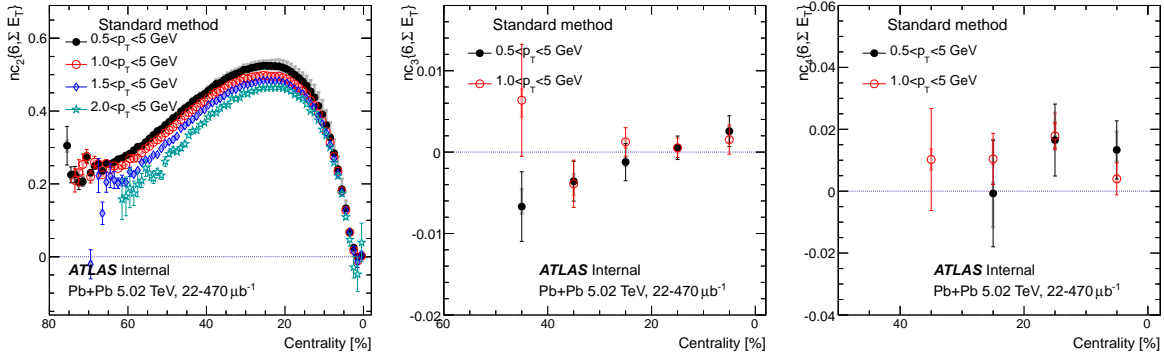


Figure 74: 6-particle normalized cumulant as a function of centrality, calculated using standard method, with multiple p_T ranges.

¹³⁹² **9.4 Cumulant ratio $v_n\{4\}/v_n\{2\}$ with $n = 2, 3, 4$**

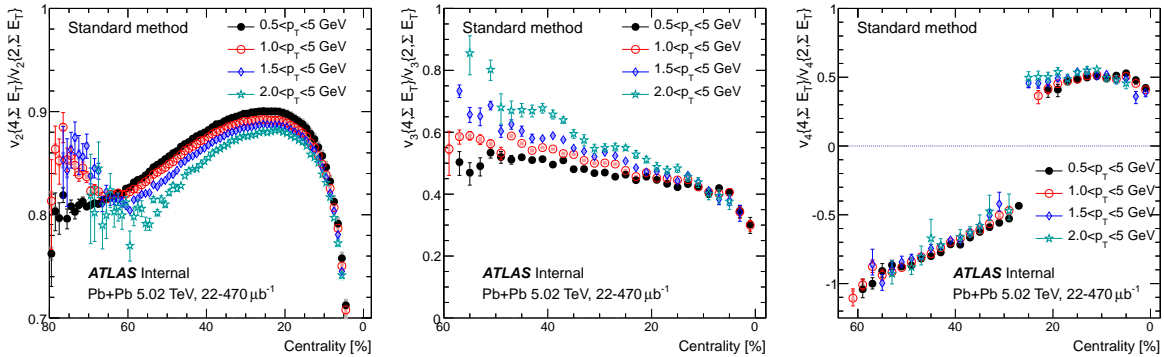


Figure 75: Cumulant ratio $v_n\{4\}/v_n\{2\}$ as a function of centrality, calculated using standard method, with multiple p_T ranges.

¹³⁹³ **9.5 Cumulant ratio $v_n\{6\}/v_n\{4\}$ with $n = 2$ and comparison with CMS**

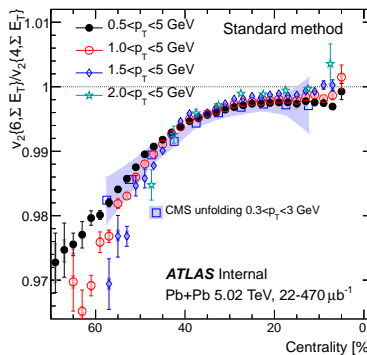


Figure 76: Cumulant ratio $v_n\{6\}/v_n\{4\}$ as a function of centrality, calculated using standard method, with multiple p_T ranges.

1394 9.6 Symmetric and asymmetric cumulant

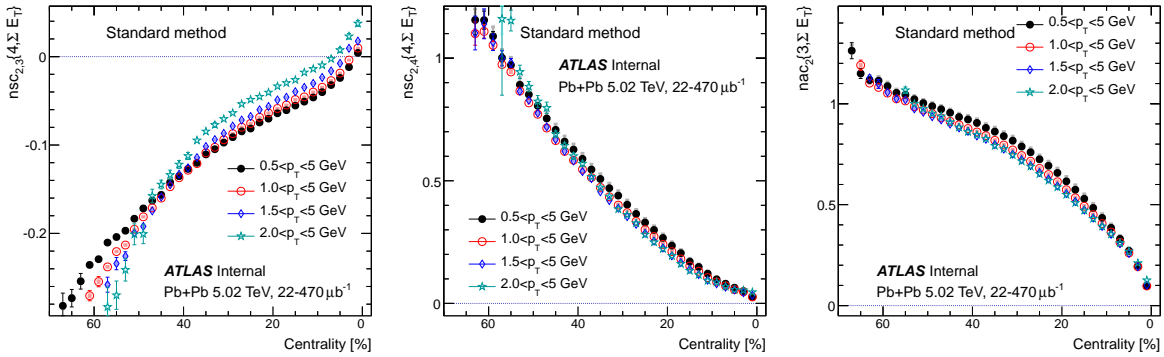


Figure 77: Normalized symmetric and asymmetric cumulants as a function of centrality, calculated using standard method, with multiple p_T ranges.

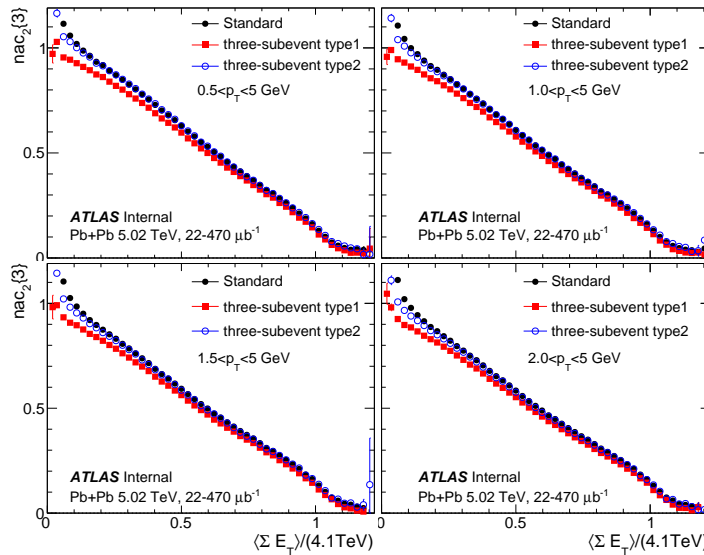


Figure 78: The $nac_2\{3\}$ from the standard method (solid circles), three-subevent method with V_4 defined in subevent a or c (solid squares) and three-subevent method with V_4 defined in subevent b (open circles). Different panels correspond to different p_T ranges. Only statistical uncertainties are shown.

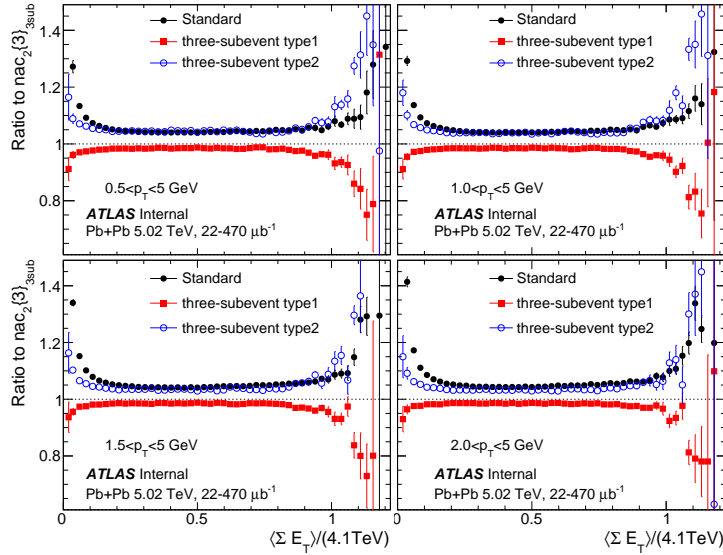


Figure 79: The ratio of $nac_2\{3\}$ from the standard method (solid circles), three-subevent method with V_4 defined in subevent a or c (solid squares) and three-subevent method with V_4 defined in subevent b (open circles) to $nac_2\{3\}$ from the three-subevent method combined. Different panels correspond to different p_T ranges. Only statistical uncertainties are shown.

1395 9.7 Volume fluctuation

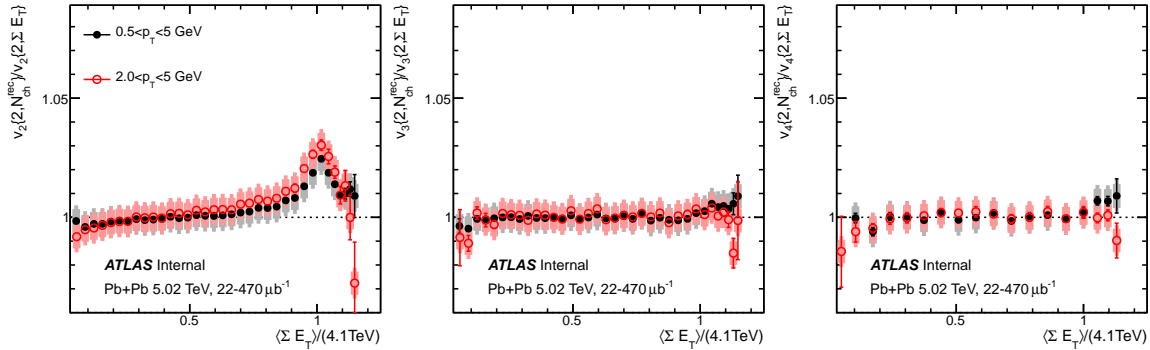


Figure 80: Check of volume fluctuation for 2-particle flow cumulant.

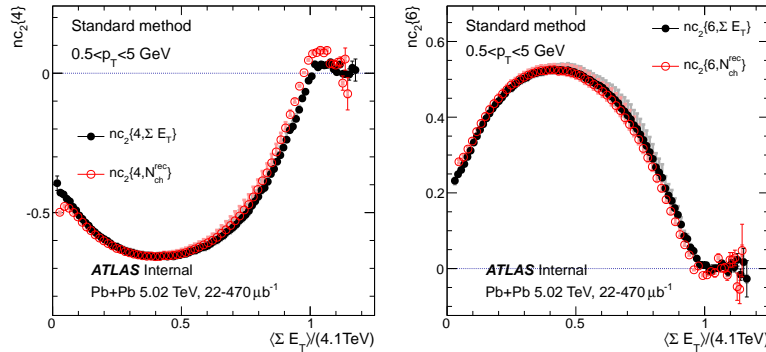


Figure 81: Check of volume fluctuation for 4- and 6-particle flow cumulant.

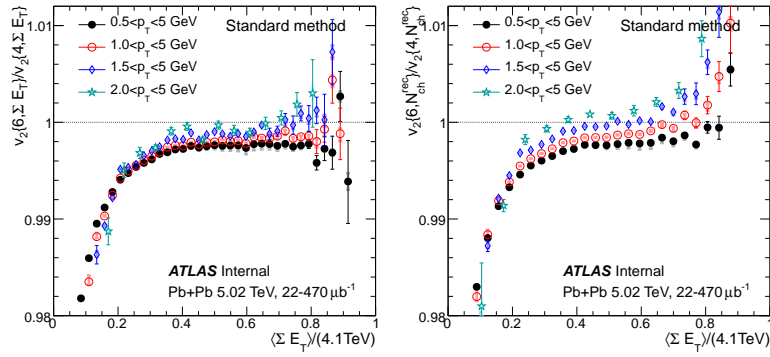


Figure 82: Check of volume fluctuation for cumulant ratios.

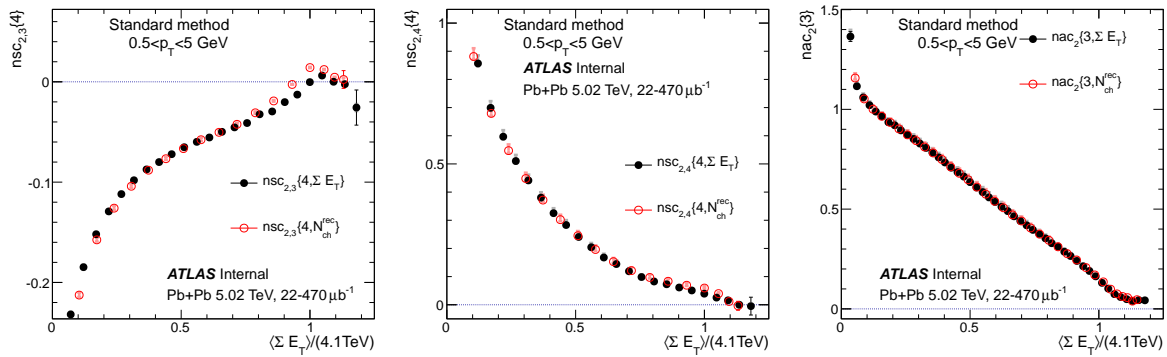


Figure 83: Check of volume fluctuation for symmetric and asymmetric cumulants.

1396 10 Summary

1397 This internal note presents details of measurements of the multi-particle azimuthal anisotropy in lead-lead
 1398 collisions at 5.02 TeV at the LHC in 2015. The measurements are performed for charged particles with
 1399 various transverse momenta, from $0.5 < p_T < 5.0$ GeV to $2.0 < p_T < 5.0$ GeV, and in the pseudorapidity
 1400 range $|\eta| < 2.5$. The anisotropy is characterized by the cumulant form of Fourier coefficients, $c_n\{4\}$,
 1401 of the charged-particle azimuthal angle distribution. The Fourier coefficients are evaluated using multi-
 1402 particle cumulant calculated with the direct cumulant (Q-cumulant) method.

1403 The features of this analysis is listed as follows:

- 1404 • Cumulants are measured in different p_T ranges, where we require all particles coming from the
 1405 same high p_T range. In previous measurements only one particle is from high p_T , which requires
 1406 the assumption that cumulant is factorizable in p_T ;
- 1407 • For the first time, cumulant of the dipolar flow $c_1\{4\}$ is found to be non-zero with particles from
 1408 high p_T range and the magnitude of $c_1\{4\}$ increases towards peripheral collisions;
- 1409 • We performed a precise measurement of higher-order harmonic c_4 , as a function of centrality.
 1410 $c_4\{4\}$ is found to be negative only in the central and mid-central collisions, which indicates an
 1411 interplay between linear and non-linear contribution in the hydrodynamic picture;
- 1412 • With ample statistics from ultra-central collision triggers, detailed studies of cumulant in most-
 1413 central collisions show interesting sign change behavior of $c_2\{4\}$ and $c_2\{6\}$, which could be ex-
 1414 plained by the volume fluctuation and centrality resolution;
- 1415 • We have tested two fluctuation models: Gaussian and power-law, and v_2 fluctuation is found to
 1416 be closer to Gaussian than power-law, while the v_3 fluctuation is consistent with purely randomly
 1417 fluctuation;
- 1418 • To study the correlation between different flow harmonics, symmetric and asymmetric cumulants
 1419 are measured with high precision;
- 1420 • For all the observables above, the measurements are repeated with three different event class def-
 1421 initions. The purpose is to evaluate the potential centrality fluctuation effects on cumulant mea-
 1422 surements, and we do observe differences in most of the observables;

1423 11 Appendix

1424 11.1 Systematics from 3-subevent method

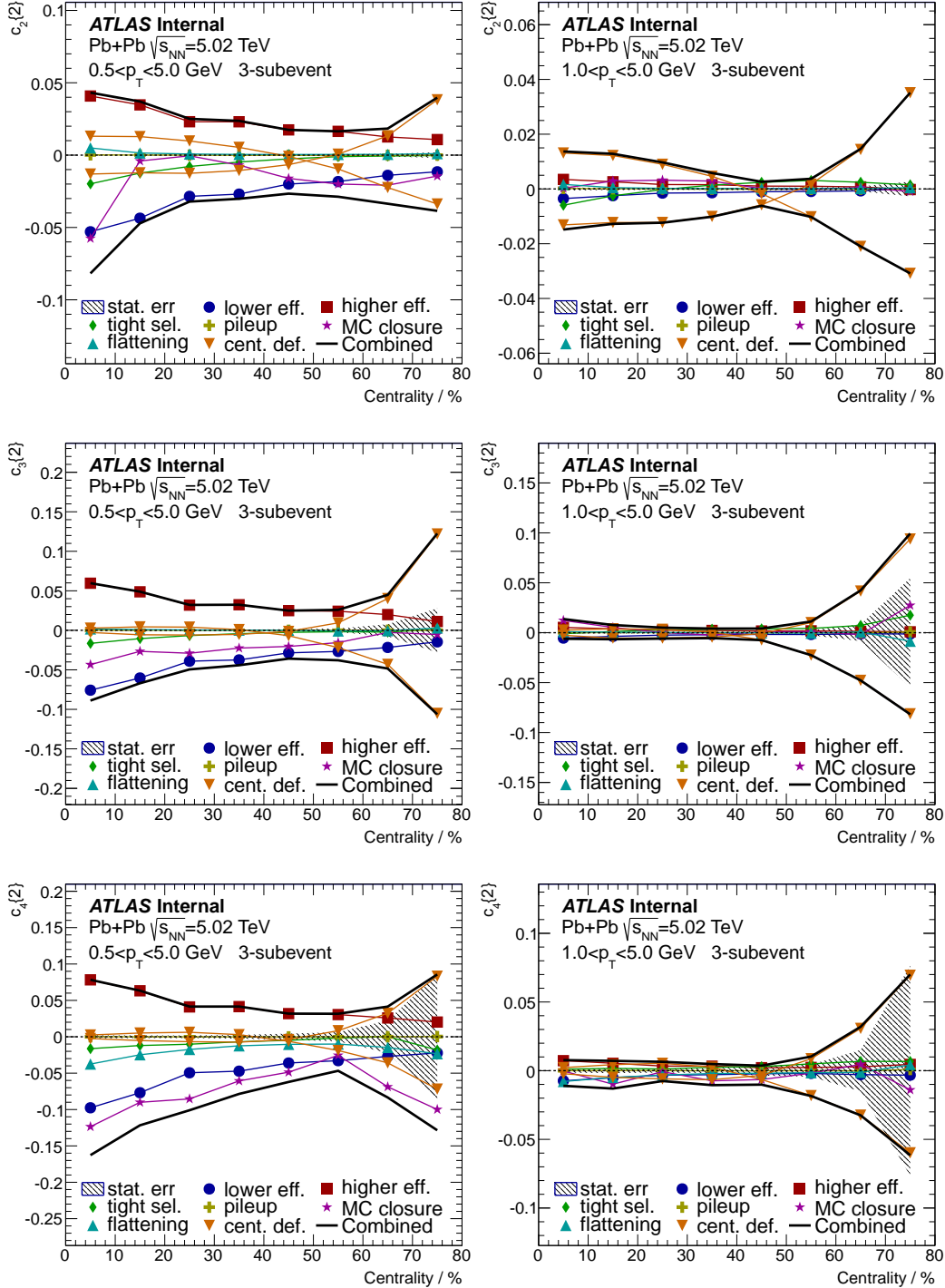


Figure 84: Breakdown of systematics for 2-particle cumulant $c_n\{2\}$ using 3-subevent method, with low (left) and high (right) p_T ranges. Different rows are for different harmonics.

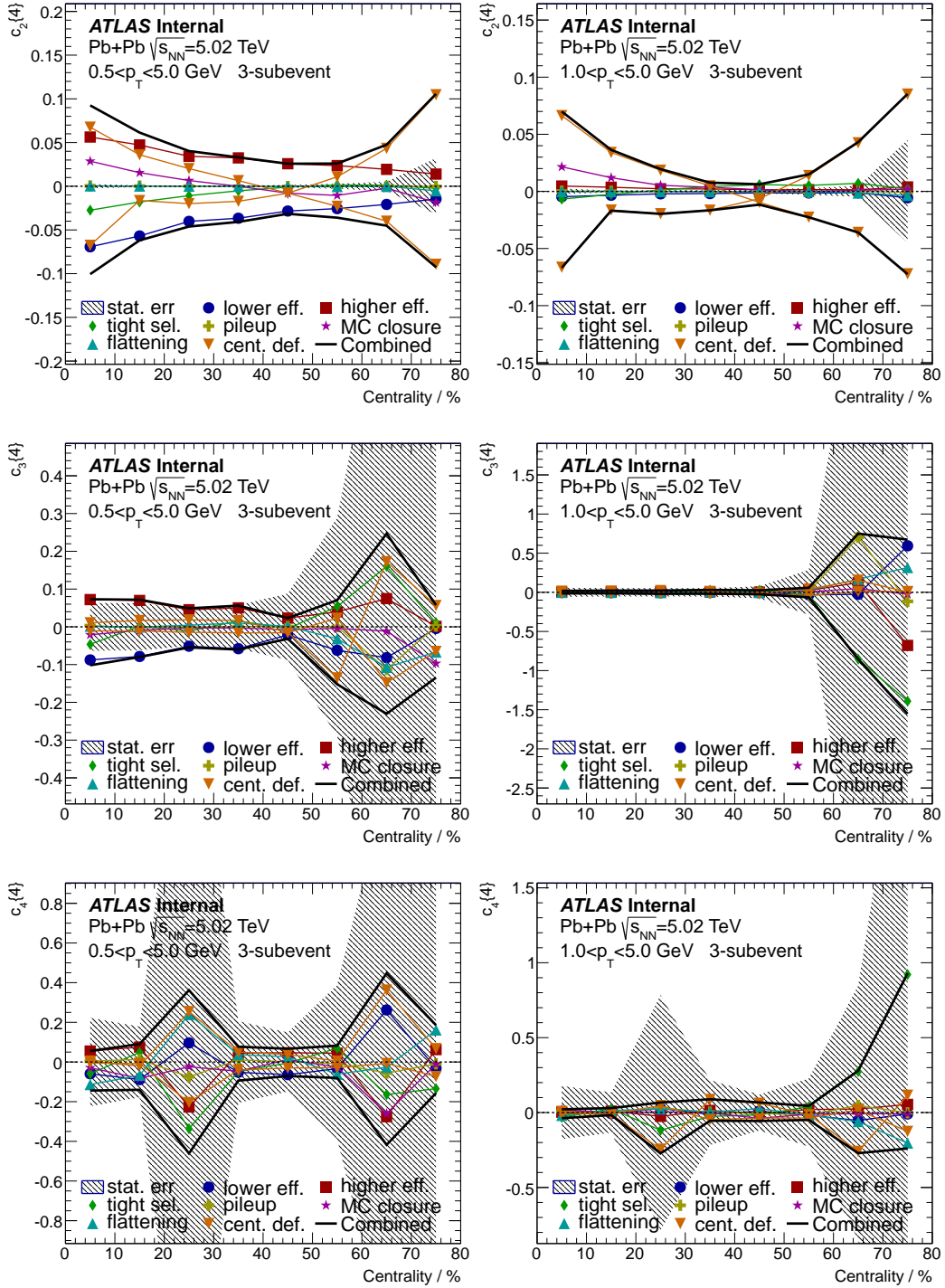


Figure 85: Breakdown of systematics for 4-particle cumulant $c_n\{4\}$ using 3-subevent method, with low (left) and high (right) p_T ranges. Different rows are for different harmonics.

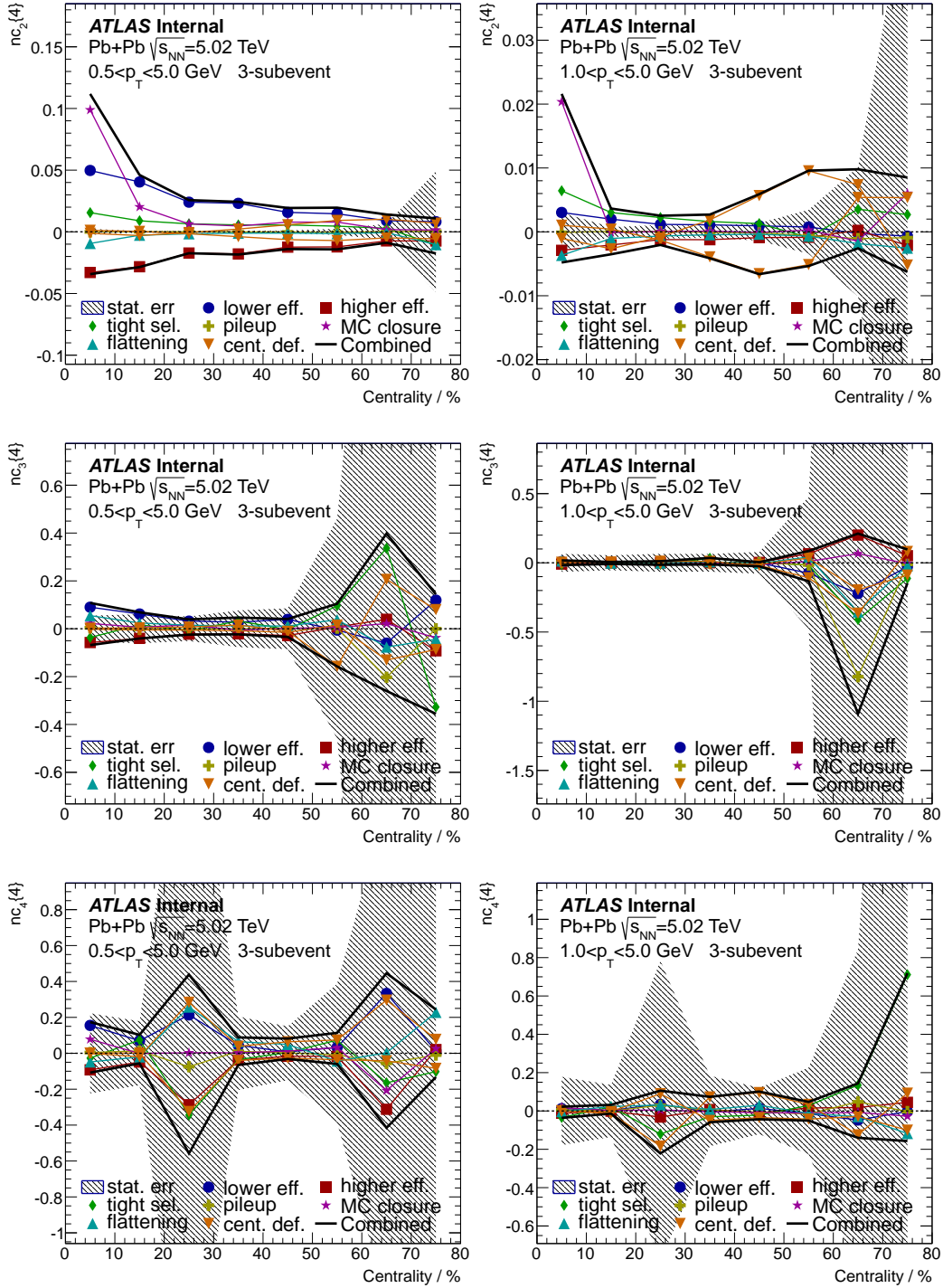


Figure 86: Breakdown of systematics for 4-particle normalized cumulant $\hat{c}_n\{4\}$ using 3-subevent method, with low (left) and high (right) p_T ranges. Different rows are for different harmonics.

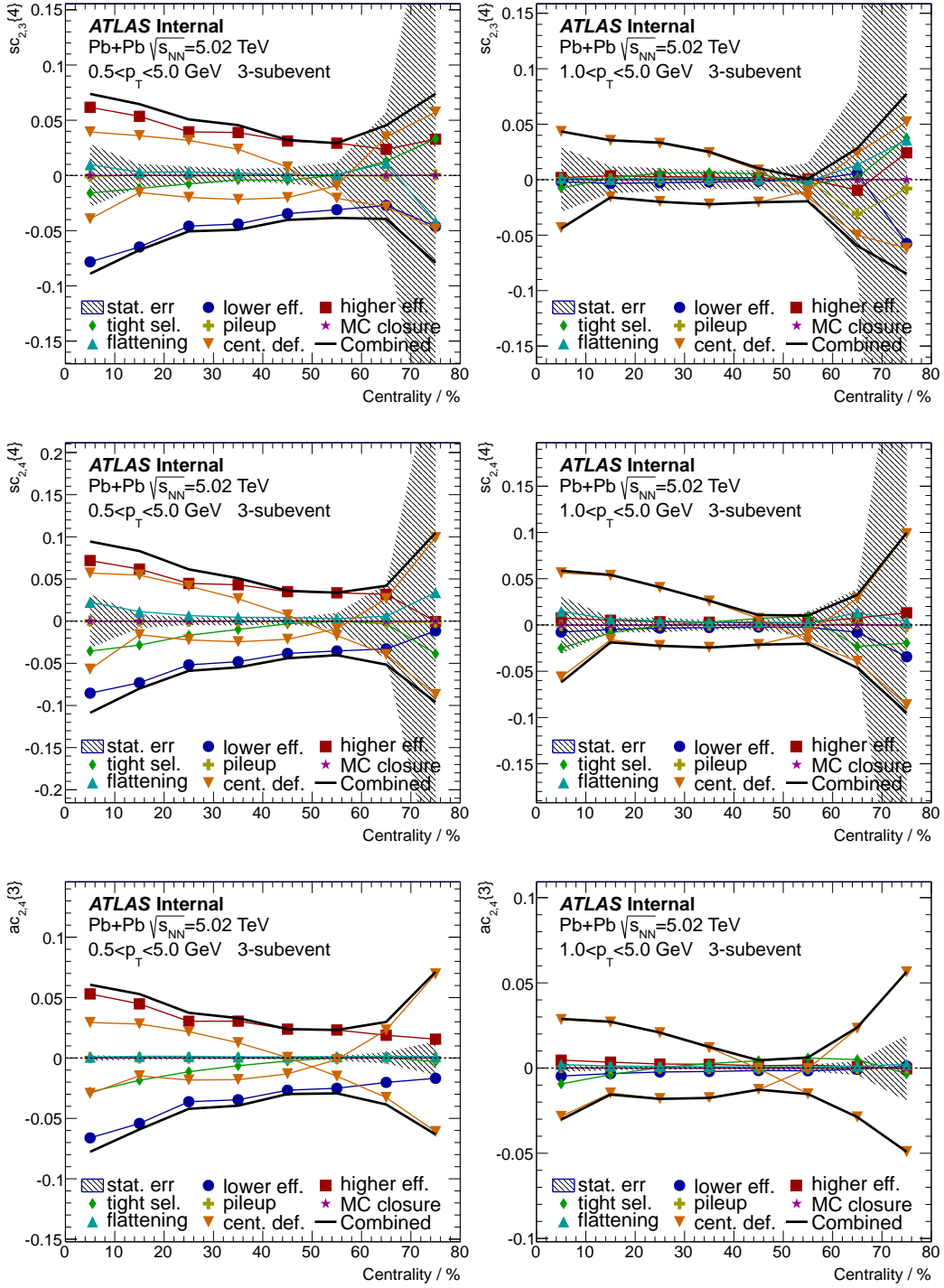


Figure 87: Breakdown of systematics for symmetric and asymmetric cumulants, using 3-subevent method, with low (left) and high (right) p_T ranges. Different rows are for different harmonics.

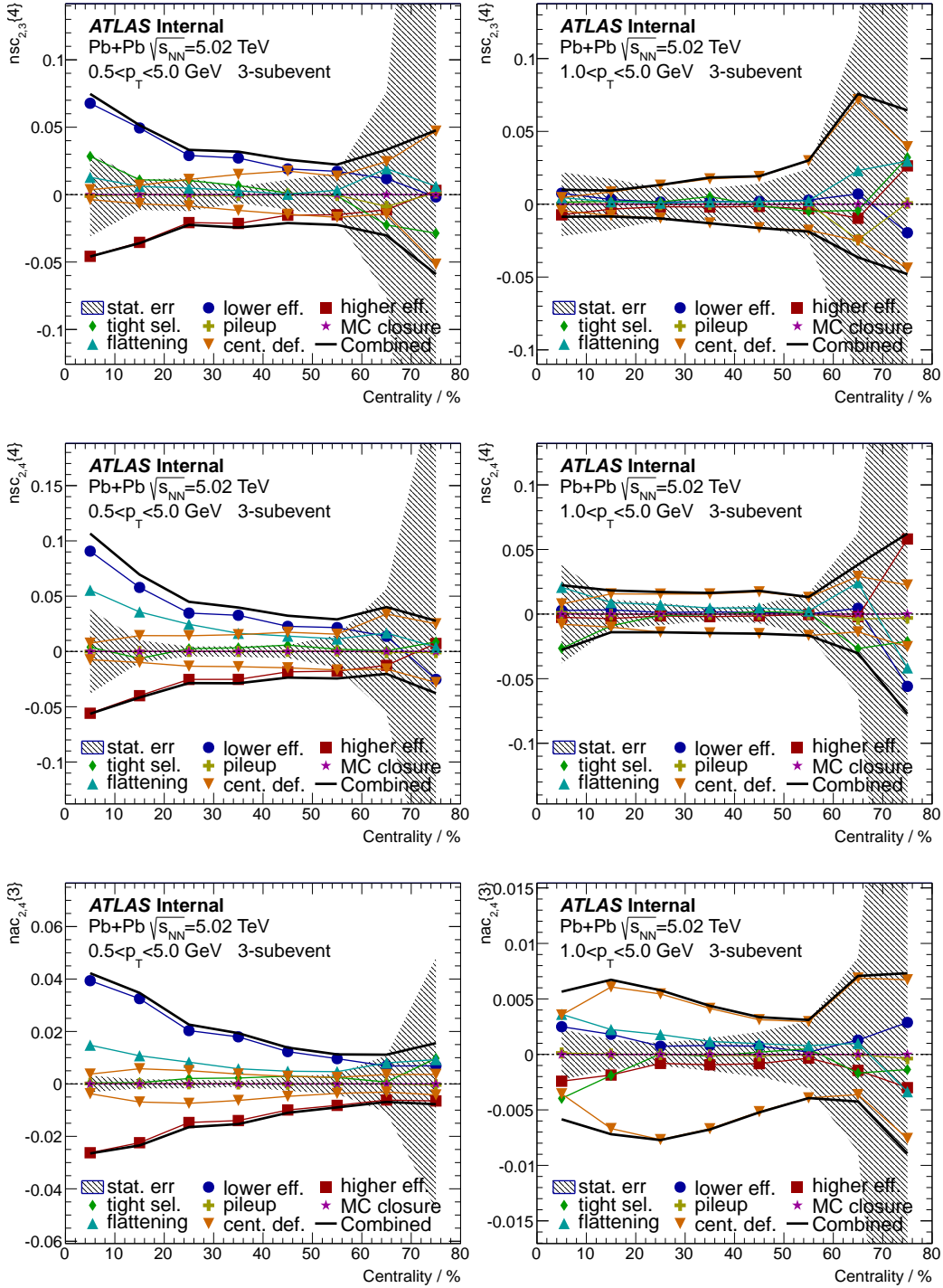


Figure 88: Breakdown of systematics for normalized symmetric and asymmetric cumulants, using 3-subevent method, with low (left) and high (right) p_T ranges. Different rows are for different harmonics.

1425 11.2 Results for 2.76 TeV Pb+Pb

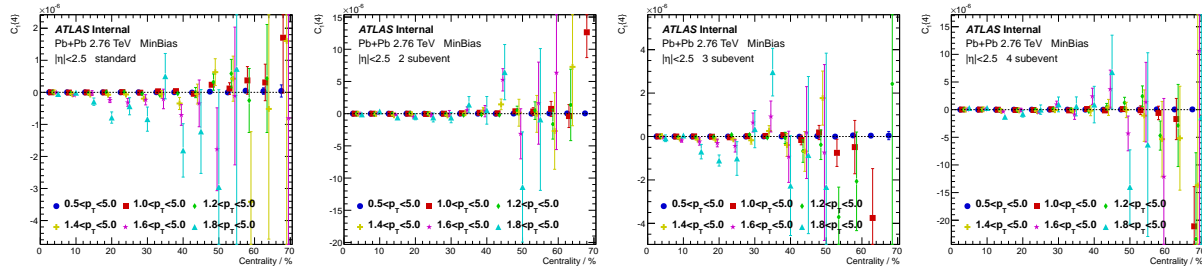


Figure 89: $c_1\{4\}$ in 2.76 TeV Pb+Pb, calculated in different p_T ranges. Each panel is for each cumulant method.

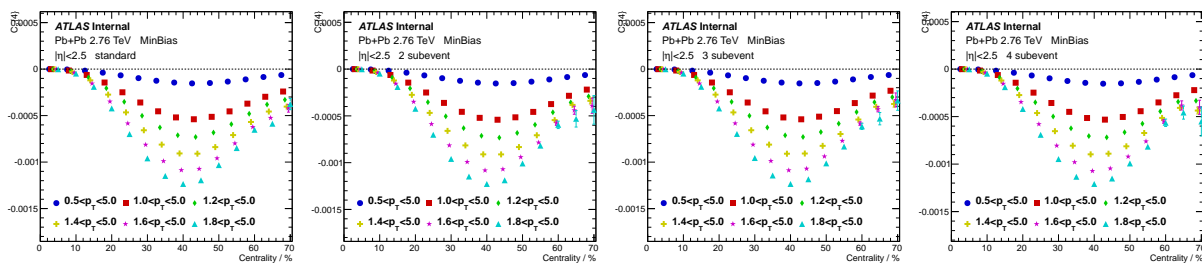


Figure 90: $c_2\{4\}$ in 2.76 TeV Pb+Pb, calculated in different p_T ranges. Each panel is for each cumulant method.

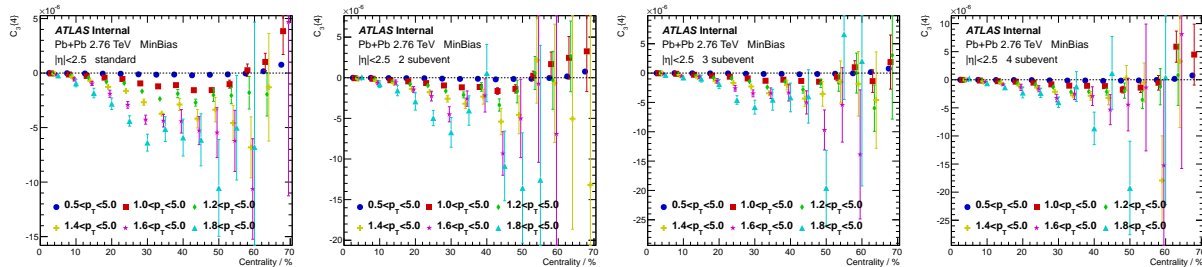


Figure 91: $c_3\{4\}$ in 2.76 TeV Pb+Pb, calculated in different p_T ranges. Each panel is for each cumulant method.

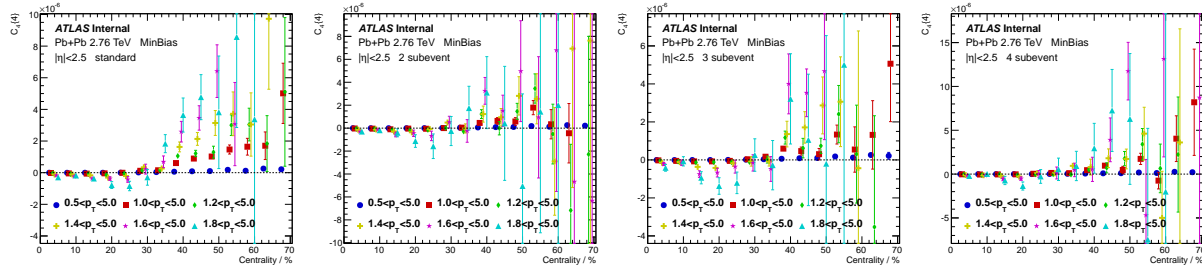


Figure 92: $c_4\{4\}$ in 2.76 TeV Pb+Pb, calculated in different p_T ranges. Each panel is for each cumulant method.

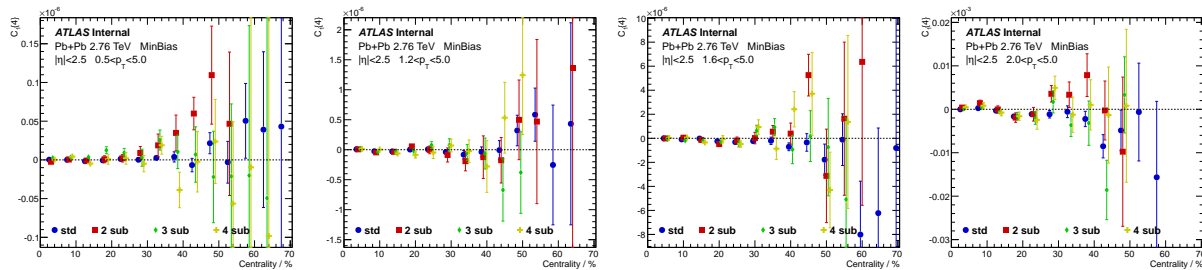


Figure 93: $c_1\{4\}$ in 2.76 TeV Pb+Pb, calculated with different cumulant methods. Each panel is for each p_T range.

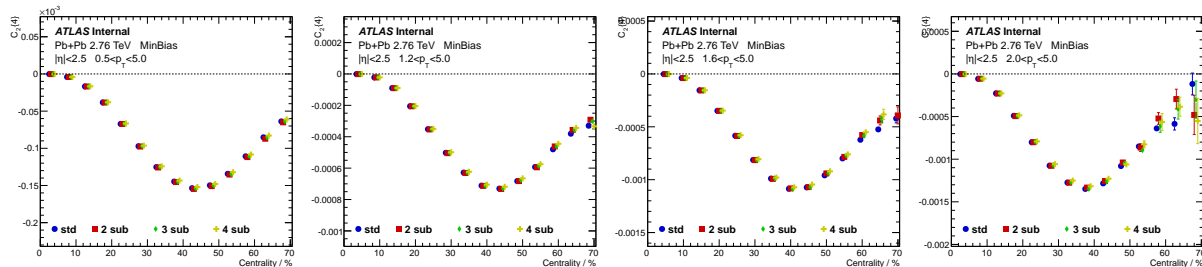


Figure 94: $c_2\{4\}$ in 2.76 TeV Pb+Pb, calculated with different cumulant methods. Each panel is for each p_T range.

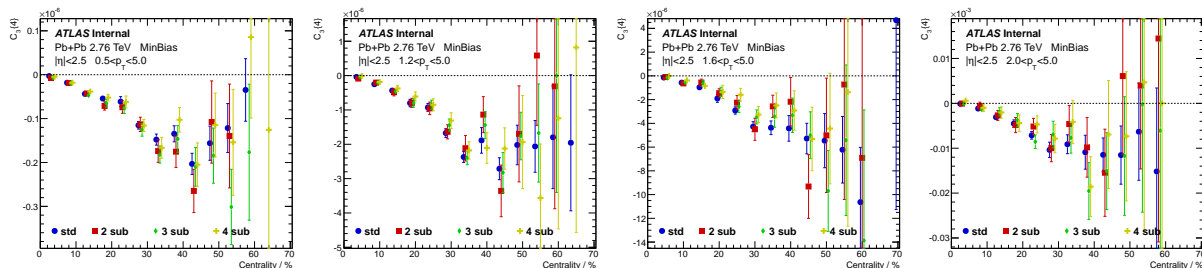


Figure 95: $c_3\{4\}$ in 2.76 TeV Pb+Pb, calculated with different cumulant methods. Each panel is for each p_T range.

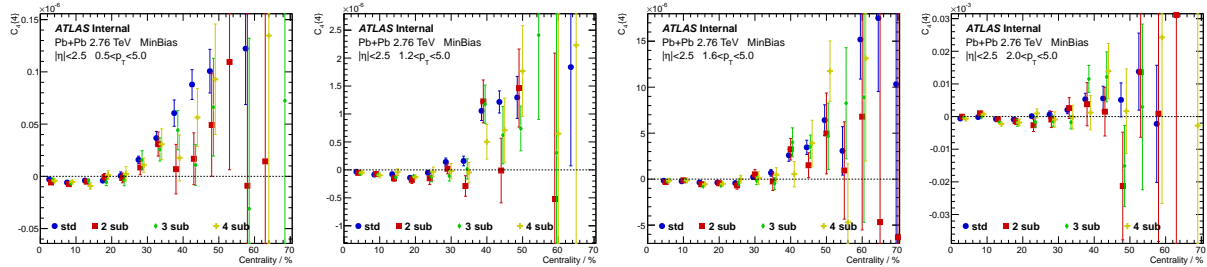


Figure 96: $c_4\{4\}$ in 2.76 TeV Pb+Pb, calculated with different cumulant methods. Each panel is for each p_T range.

1426 11.3 Results for 2.76 TeV Pb+Pb HIJING

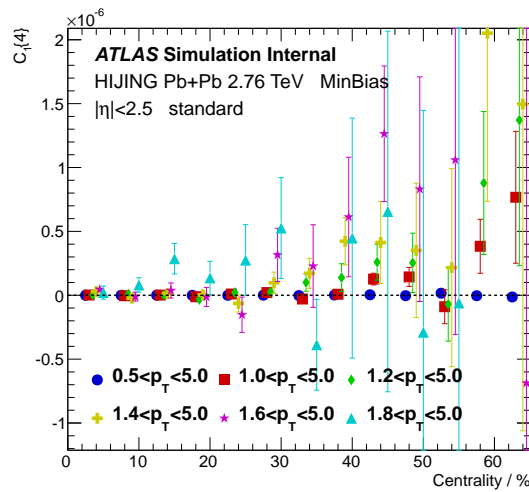


Figure 97: $c_1\{4\}$ in 2.76 TeV HIJING Pb+Pb, calculated in different p_T ranges.

1427 References

- 1428 [1] C. Gale, S. Jeon, and B. Schenke, “Hydrodynamic Modeling of Heavy-Ion Collisions,” *Int. J. Mod.*
1429 *Phys.*, vol. A28, p. 1340011, 2013.
- 1430 [2] U. Heinz and R. Snellings, “Collective flow and viscosity in relativistic heavy-ion collisions,” *Ann.*
1431 *Rev. Nucl. Part. Sci.*, vol. 63, pp. 123–151, 2013.
- 1432 [3] F. G. Gardim, F. Grassi, M. Luzum, and J.-Y. Ollitrault, “Mapping the hydrodynamic response to
1433 the initial geometry in heavy-ion collisions,” *Phys. Rev.*, vol. C85, p. 024908, 2012.
- 1434 [4] C. Gale, S. Jeon, B. Schenke, P. Tribedy, and R. Venugopalan, “Event-by-event anisotropic flow
1435 in heavy-ion collisions from combined Yang-Mills and viscous fluid dynamics,” *Phys. Rev. Lett.*,
1436 vol. 110, no. 1, p. 012302, 2013.
- 1437 [5] N. Borghini, P. M. Dinh, and J.-Y. Ollitrault, “A New method for measuring azimuthal distributions
1438 in nucleus-nucleus collisions,” *Phys. Rev.*, vol. C63, p. 054906, 2001.
- 1439 [6] A. Bilandzic, R. Snellings, and S. Voloshin, “Flow analysis with cumulants: Direct calculations,”
1440 *Phys. Rev.*, vol. C83, p. 044913, 2011.
- 1441 [7] A. Bilandzic, C. H. Christensen, K. Gulbrandsen, A. Hansen, and Y. Zhou, “Generic framework
1442 for anisotropic flow analyses with multiparticle azimuthal correlations,” *Phys. Rev.*, vol. C89, no. 6,
1443 p. 064904, 2014.
- 1444 [8] J. Jia, M. Zhou, and A. Trzupek, “Revealing long-range multiparticle collectivity in small collision
1445 systems via subevent cumulants,” *Phys. Rev.*, vol. C96, no. 3, p. 034906, 2017.
- 1446 [9] J. Adam *et al.*, “Correlated event-by-event fluctuations of flow harmonics in Pb-Pb collisions at
1447 $\sqrt{s_{NN}} = 2.76 \text{ TeV}$,” *Phys. Rev. Lett.*, vol. 117, p. 182301, 2016.
- 1448 [10] M. Zhou and J. Jia, “Centrality or volume fluctuations in heavy-ion collisions,” 2018.
- 1449 [11] V. Skokov, B. Friman, and K. Redlich, “Volume Fluctuations and Higher Order Cumulants of the
1450 Net Baryon Number,” *Phys. Rev.*, vol. C88, p. 034911, 2013.
- 1451 [12] “Measurement of four-particle azimuthal cumulants in Pb+Pb collisions at $\sqrt{s_{NN}} = 5.02 \text{ TeV}$ with
1452 the ATLAS detector,” Tech. Rep. ATLAS-CONF-2017-066, CERN, Geneva, Sep 2017.
- 1453 [13] M. Aaboud *et al.*, “Measurement of long-range multiparticle azimuthal correlations with the
1454 subevent cumulant method in pp and $p + Pb$ collisions with the ATLAS detector at the CERN
1455 Large Hadron Collider,” *Phys. Rev.*, vol. C97, no. 2, p. 024904, 2018.
- 1456 [14] J. Adam *et al.*, “Anisotropic flow of charged particles in Pb-Pb collisions at $\sqrt{s_{NN}} = 5.02 \text{ TeV}$,”
1457 *Phys. Rev. Lett.*, vol. 116, no. 13, p. 132302, 2016.
- 1458 [15] G. Aad *et al.*, “Measurement of flow harmonics with multi-particle cumulants in Pb+Pb collisions
1459 at $\sqrt{s_{NN}} = 2.76 \text{ TeV}$ with the ATLAS detector,” *Eur. Phys. J.*, vol. C74, no. 11, p. 3157, 2014.
- 1460 [16] V. Khachatryan *et al.*, “Evidence for transverse momentum and pseudorapidity dependent event
1461 plane fluctuations in PbPb and pPb collisions,” *Phys. Rev.*, vol. C92, no. 3, p. 034911, 2015.
- 1462 [17] M. Aaboud *et al.*, “Measurement of longitudinal flow decorrelations in Pb+Pb collisions at $\sqrt{s_{NN}} =$
1463 2.76 and 5.02 TeV with the ATLAS detector,” *Eur. Phys. J.*, vol. C78, no. 2, p. 142, 2018.

- 1464 [18] G. Aad *et al.*, “Measurement of the azimuthal anisotropy for charged particle production in $\sqrt{s_{NN}} =$
1465 2.76 TeV lead-lead collisions with the ATLAS detector,” *Phys. Rev.*, vol. C86, p. 014907, 2012.
- 1466 [19] A. M. Sirunyan *et al.*, “Non-Gaussian elliptic-flow fluctuations in PbPb collisions at $\sqrt{s_{NN}} = 5.02$
1467 TeV,” 2017.
- 1468 [20] A. M. Poskanzer and S. A. Voloshin, “Methods for analyzing anisotropic flow in relativistic nuclear
1469 collisions,” *Phys. Rev.*, vol. C58, pp. 1671–1678, 1998.
- 1470 [21] K. Burka, A. Trzupek, and T. Bold, “Measurement of centrality, pseudorapidity and pT dependence
1471 of higher flow harmonics in lead-lead collisions at $\sqrt{s_{NN}} = 5.02$ TeV with the ATLAS detector,”
1472 Tech. Rep. ATL-COM-PHYS-2016-490, CERN, Geneva, May 2016.
- 1473 [22] L. Yan and J.-Y. Ollitrault, “Universal fluctuation-driven eccentricities in proton-proton, proton-
1474 nucleus and nucleus-nucleus collisions,” *Phys. Rev. Lett.*, vol. 112, p. 082301, 2014.
- 1475 [23] A. K. Morley, T. Kuhl, G. Conti, E. Nurse, K. Wozniak, S. Martin-Haugh, O. Arnaez, D. Schaefer,
1476 J. Kvita, P. E. Sidebo, J. T. Kuechler, D. Boerner, O. Kepka, F. Nechansky, M. Vozak, M. R. Devesa,
1477 R. Iuppa, R. Lysak, W. Lukas, C. Eckardt, V. Cairo, M. Danninger, T. Cuhadar Donszelmann,
1478 A. Chisholm, Y. Kulchitsky, E. Plotnikova, H. Oide, A. Lister, S. Pagan Griso, H. Gray, D. Kar,
1479 A. Salzburger, T. Martin, and P. Tsiareshka, “Supporting note for the Minimum Bias publication:
1480 Charge particle multiplicity in pp interactions at 13 TeV measured with the ATLAS detector,” Tech.
1481 Rep. ATL-COM-PHYS-2015-313, CERN, Geneva, Apr 2015.
- 1482 [24] J. Jia and M. Zhou, “Flow fluctuations in Pb+Pb collisions at $\sqrt{s_{NN}} = 5.02$ TeV with the ATLAS
1483 detector,” Tech. Rep. ATL-COM-PHYS-2018-346, CERN, Geneva, Apr 2018. First paper draft,
1484 will aim for confnote conversion for the Quark Matter 2018 conference in May 13th.